DOT/FAA/AR-07/58

Air Traffic Organization
Operations Planning
Office of Aviation Research
and Development
Washington, DC 20591

Aircraft Cargo Compartment Multisensor Smoke Detection Algorithm Development

February 2008

Final Report

U.S. Department of Transportation
Federal Aviation Administration

NOTICE

Technical Report Documentation Page

1. Report No.	2. Government Accession No.	3. Recipient's Catalog No.
DOT/FAA/AR-07/58		

4. Title and Subtitle	5. Report Date
AIRCRAFT CARGO COMPARTMENT MULTISENSOR SMOKE DETECTION ALGORITHM DEVELOPMENT	February 2008
	6. Performing Organization Code
7. Author(s)	8. Performing Organization Report No.
Adityanand Girdhari	
9. Performing Organization Name and Address	10. Work Unit No. (TRAIS)
Rutgers, The State University of New Jersey New Brunswick, NJ 08901	
	11. Contract or Grant No.
12. Sponsoring Agency Name and Address	13. Type of Report and Period Covered
U.S. Department of Transportation Federal Aviation Administration Air Traffic Organization Operations Planning Office of Aviation Research and Development Washington, DC 20591	Final Report
	14. Sponsoring Agency Code ANM-110

15. Supplementary Notes

The Federal Aviation Administration Airport and Aircraft Safety R&D Division COTR was David Blake.

16. Abstract

There is a need to effectively develop and test an advanced fire detection system for aircraft cargo compartments that significantly reduces false alarms and improves alarm time response. Title 14 Code of Federal Regulations Part 25.858 requires that aircraft detection systems alarm within 1 minute of the start of a fire. Gas concentrations, temperature fluctuations, and particulate levels are three main parameters representative of a complete fire signature. Current aircraft detection systems depend solely on one parameter, particulate levels, for the detection of this wide fire signature. Improved fire detection capabilities can be achieved by combining multiple fire signatures or parameters in specific algorithms.

An advanced fire detection system combining an ionization smoke detector, thermocouple, smokemeter, and a carbon monoxide (CO)/carbon dioxide (CO_2) gas probe was installed in a Boeing 707 forward cargo compartment. A broad spectrum of fire and nuisance sources were tested to produce a matrix of extreme detector levels from all four sensors. This matrix provided alarm threshold criteria that aided in the development of a multisensor algorithm based on fire signatures such as CO and CO_2 gas concentrations, temperature, ionization chamber voltage, and percent light transmission per foot. Multiple algorithms were created to determine the most effective multisensor algorithm that responded the fastest to fires while providing nuisance immunity. A spatial distribution analysis was conducted by using a Computational Fluid Dynamic (CFD) model to specify the physical range of the multisensor detector subjected to the optimized algorithm.

A multisensor algorithm combining CO_2 gas concentrations, percent light transmission per foot, and ionization chamber voltage parameters produced a 100% success rate for detection of fires within 1 minute while providing nuisance immunity to those signatures tested. Comparison of computational and experimental alarm time, smokemeter, and ionization chamber results demonstrated the effectiveness of the CFD and provided strong evidence that the CFD can be used as a virtual detector to simulate fires with an average alarm time uncertainty of 2.57 seconds. Spatial distribution analysis from the CFD determined the physical range of the single multisensor detector to be at least 910 cubic feet, the volume of the Boeing 707 forward cargo compartment.

17. Key Words	18. Distribution Statement
Multicriteria fire detector, False alarm, Cargo compartments	This document is available to the U.S. public through the National Technical Information Service (NTIS) Springfield, Virginia 22161.

19. Security Classif. (of this report)	20. Security Classif. (of this page)	21. No. of Pages	22. Price
Unclassified	Unclassified	98	

ACKNOWLEDGEMENTS

The author would like to thank Professor Constantine Polymeropolous and Professor Tobias Rossmann for their professional and personal guidance. The numerous enlightening discussions on the topics of aircraft fire safety, heat transfer, computational modeling, and experimental methods and procedures were instrumental in this research. The leadership exhibited by both professors has been uncompromising and most valuable.

The author would also like to thank Mr. Richard G. Hill, Mr. Gus Sarkos, and Mr. David Blake at the Fire Safety Branch of the Federal Aviation Administration (FAA) William J. Hughes Technical Center for providing the support and facilities. These three professional individuals offered extensive knowledge, wisdom, and insight about the field of aircraft fire safety that is represented in this thesis. Their guidance and encouragement during the research at the William J. Hughes Technical Center was extremely valuable and truly appreciated.

The author would like to thank Mr. Rick Whedbee, Mr. Frank Gibbons, and Mr. Mark Materio for their professional help in the development of the experimental apparatus and assistance in conducting numerous fire tests. Much thanks and appreciation goes out to the entire staff of the Fire Safety Branch of the FAA William J. Hughes Technical Center for aiding in the completion of this thesis.

The Department of Mechanical and Aerospace Engineering at Rutgers University provided many opportunities. The author wants to thank the entire department, faculty, and staff for their support, kindness, and generosity.

TABLE OF CONTENTS

Page

EXECUTIVE SUMMARY xv

1. INTRODUCTION 1

1.1 Background 1
1.2 Objectives 2

2. REVIEW OF LITERATURE 2

2.1 Historical Overview 2
2.2 Cargo Compartments 3
2.3 Transport of Cargo 4
2.4 Current Technologies 4

2.4.1 Multisensor Detectors and Algorithms 5
2.4.2 Video-Based Detection 7
2.4.3 Semiconducting Gas Detector 7
2.4.4 Rugged LED-Based Detector 7

3. EXPERIMENTAL APPARATUS 8

3.1 General Design 8
3.2 Measuring Ionization Chamber 10
3.3 Smokemeter 13
3.4 Computational Fluid Dynamic Model 16

3.4.1 Light Transmission Data Conversion 17
3.4.2 Gas Data Conversion 17
3.4.3 Measuring Ionization Chamber Correlation 18

4. EXPERIMENTAL PROCEDURE 18

4.1 Experimental Testing 18

4.1.1 Fire Tests 21
4.1.2 Nuisance Source Tests 22

4.2 Computational Testing 24

5. RESULTS AND DISCUSSION 27

5.1 Data Analyzing Method 27
5.2 Experimental Fire Testing 28

5.2.1 Denatured Alcohol 28
5.2.2 Polyurethane Foam 30
5.2.3 Alcohol-Soaked Rags 34
5.2.4 Shredded Newspaper 36
5.2.5 Suitcase 38

5.3 Perimeter Experimental Fire Testing 41

5.3.1 Smokemeter 41
5.3.2 Measuring Ionization Chamber 43
5.3.3 The CO_2 Gas Probe 44
5.3.4 The CO Gas Probe 45
5.3.5 Thermocouple 46

5.4 Experimental Nuisance Testing 48

5.4.1 Vaporizer 48
5.4.2 Arizona Test Dust 49
5.4.3 Heat Gun 51
5.4.4 Exhaust Fumes 53
5.4.5 Occupied Compartment 54

5.5 Perimeter Experimental Nuisance Testing 54
5.6 Algorithm Development 57
5.7 Detector Performance 62

5.7.1 Detector Alarm Time Comparison 65
5.7.2 Detector Nuisance Immunity Comparison 65

5.8 Computational Analysis 66

5.8.1 X Location 66
5.8.2 Perimeter Locations 69

5.9 Computational and Experimental Time Comparison 76
5.10 Spatial Distribution Results 79
5.11 Error Analysis 79

5.11.1 Repeatability 79
5.11.2 Thermocouple 79
5.11.3 Smokemeter 80
5.11.4 Gas Probe 80
5.11.5 Measuring Ionization Chamber 80
5.11.6 Ground and In-Flight Comparison 81

6. CONCLUSIONS 81

7. REFERENCES 82

LIST OF FIGURES

Figure		Page
1	Three-Dimensional Side View of B-707 Forward Cargo Compartment With Instrumentation	8
2	Two-Dimensional Top View of B-707 Forward Cargo Compartment	9
3	Recessed Pan Including All Sensor Instrumentation	10
4	Ionization Chamber in Clean Air	11
5	Ionization Chamber Subjected to Smoke Particles	11
6	Alarm Threshold Detection Method Setup for MIC	12
7	Photoelectric Detector in Clean Air	13
8	Photoelectric Detector Subjected to Smoke Particles	14
9	Two-Dimensional Schematic of Experimental Smokemeter Setup in Recessed Pan	14
10	Three-Dimensional Schematic of Experimental Smokemeter Setup in Recessed Pan	15
11	Comparison of Theoretical and Experimental Optical Density Tests for Calibration	16
12	Cargo Compartment Coordinate System and Fire Locations	19
13	Resin Block, FAA Repeatable Fire Source	19
14	Box Setup Used for Controlled Testing of Arizona Test Dust	22
15	Extension Stand Welded for Vaporizer and Arizona Test Dust Tests	23
16	Computational Fluid Dynamic Model Mesh Used in Simulations	24
17	Correlation of MIC to Smokemeter for Aft and X Location	25
18	Correlation of MIC to Smokemeter for Forward Location	26
19	Correlation of MIC to Smokemeter for Sidewall Location	27
20	Denatured Alcohol Average Percent Light Transmission per Foot at X Location	28
21	Denatured Alcohol Average CO and CO_2 Gas Concentrations at X Location	29
22	Denatured Alcohol Average Temperature Rise at X Location	29

23	Denatured Alcohol Average MIC Voltage at X Location	30
24	Polyurethane Foam Average Percent Light Transmission per Foot at X Location	31
25	Polyurethane Foam Average CO and CO_2 Gas Concentrations at X Location	32
26	Polyurethane Foam Average Temperature Rise at X Location	33
27	Polyurethane Foam Average MIC Voltage at X Location	33
28	Alcohol-Soaked Rags Average Percent Light Transmission per Foot at X Location	34
29	Alcohol-Soaked Rags Average CO and CO_2 Gas Concentrations at X Location	35
30	Alcohol-Soaked Rags Average Temperature Rise at X Location	35
31	Alcohol Soaked Rags Average MIC Voltage at X Location	36
32	Shredded Newspaper Average Percent Light Transmission per Foot	37
33	Shredded Newspaper Average CO and CO_2 Gas Concentrations at X Location	37
34	Shredded Newspaper Average Temperature Rise at X Location	38
35	Shredded Newspaper Average MIC Voltage at X Location	38
36	Suitcase Average Percent Light Transmission per Foot at X Location	39
37	Suitcase Average CO and CO_2 Gas Concentrations at X Location	39
38	Suitcase Average Temperature Rise at X Location	40
39	Suitcase Average MIC Voltage at X Location	40
40	Forward Starboard Corner Percent Light Transmission per Foot Results	42
41	Aft Starboard Corner Percent Light Transmission per Foot Results	42
42	Forward Starboard Corner MIC Voltages	43
43	Aft Starboard Corner MIC Voltages	44
44	Forward Starboard Corner CO_2 Gas Concentrations	44
45	Aft Starboard Corner CO_2 Gas Concentrations	45
46	Forward Starboard Corner CO Gas Concentrations	45
47	Aft Starboard Corner CO Gas Concentrations	46

48 Forward Starboard Corner Temperature Rise Results 47

49 Aft Starboard Corner Temperature Rise Results 47

50 Vaporizer Average Percent Light Transmission per Foot at X Location 48

51 Vaporizer Average MIC Voltage at X Location 49

52 Arizona Test Dust Average Percent Light Transmission per Foot at X Location 50

53 Arizona Test Dust Average MIC Voltage at X Location 50

54 Heat Gun Average Temperature Rise at X Location 51

55 Heat Gun Average Percent Light Transmission per Foot at X Location 52

56 Heat Gun Average MIC Voltage at X Location 52

57 Exhaust Fumes Average Percent Light Transmission per Foot 53

58 Exhaust Fumes Average CO and CO_2 Gas Concentrations 53

59 Occupied Compartment Human CO_2 Gas Production (1 person) 54

60 Arizona Test Dust Percent Light Transmission per Foot (2 Feet From Recessed Pan) 55

61 Arizona Test Dust MIC Voltages (2 Feet From Recessed Pan) 55

62 Arizona Test Dust Percent Light Transmission per Foot (4 Feet From Recessed Pan) 56

63 Arizona Test Dust MIC Voltages (4 Feet From Recessed Pan) 56

64 Comparison of Computational and Experimental Resin Block Percent Light Transmission per Foot at X Location 67

65 Comparison of Computational and Experimental Resin Block MIC Voltages at X Location 67

66 Comparison of Computational and Experimental Resin Block CO and CO_2 Gas Concentrations at X Location 68

67 Comparison of Computational and Experimental Resin Block Temperature Rise at X Location 68

68 Comparison of Computational and Experimental Resin Block Percent Light Transmission per Foot at Forward Starboard Location 70

69 Comparison of Computational and Experimental Resin Block MIC Voltages at Forward Starboard Location 70

70 Comparison of Computational and Experimental Resin Block CO and CO_2 Gas Concentrations at Forward Starboard Location 71

71 Comparison of Computational and Experimental Resin Block Temperature Rise at Forward Starboard Location 71

72 Comparison of Computational and Experimental Resin Block Percent Light Transmission per Foot at Aft Port Location 72

73 Comparison of Computational and Experimental Resin Block MIC Voltages at the Aft Port Location 72

74 Comparison of Computational and Experimental Resin Block CO and CO_2 Gas Concentrations at Aft Port Location 73

75 Comparison of Computational and Experimental Resin Block Temperature Rise at the Aft Port Location 73

76 Comparison of Computational and Experimental Resin Block Percent Light Transmission per Foot at the Sidewall Starboard Location 74

77 Comparison of Computational and Experimental Resin Block MIC Voltages at the Sidewall Starboard Location 74

78 Comparison of Computational and Experimental Resin Block CO and CO_2 Gas Concentrations at Sidewall Starboard Location 75

79 Comparison of Computational and Experimental Resin Block Temperature Rise at Sidewall Starboard Location 75

LIST OF TABLES

Table		Page
1	Brief Descriptions of All Real Fire and Nuisance Sources Used for Experimentation	20
2	Extreme Detector Levels for Resin Block and Nuisance Sources for X Location and Perimeter Locations	58
3	Extreme Detector Levels for All Fire Sources	60
4	Alarm Times for the Resin Block and Nuisance Sources	63
5	Alarm Times for All Fire Sources	64
6	Algorithm Results	66
7	Extreme Detector Levels	77
8	Alarm Time Comparison—Computation vs Experimental	78

LIST OF ACRONYMS

%LT/ft	Percent light transmission per foot
ac	Alternating current
AS	Aerospace Standard
CFD	Computational fluid dynamic
CFVS	Cargo Fire Verification System
CO	Carbon monoxide
CO_2	Carbon dioxide
FAA	Federal Aviation Administration
FE/DE	Fire emulator/detector evaluator
fwd	Forward
LED	Light emitting diode
MEMS	MicroElectroMechanical Systems
MIC	Measuring ionization chamber
mL	Milliliter
NASA	National Aeronautics and Space Administration
NIST	National Institute of Standards and Technology
nm	Nanometer
ppm	Parts per million
T/C	Thermocouple
TSO	Technical Standard Order
UL	Underwriters Laboratory

EXECUTIVE SUMMARY

This report describes the development of a multicriteria alarm algorithm for the detection of aircraft cargo compartment fires. Current regulations require that most cargo compartments be equipped with a fire detection system that will alarm within 1 minute of the start of a fire. Flight tests are required to show compliance with this regulation. For safety purposes, the flight tests typically use an artificial smoke source that does not contain many of the elements associated with an actual fire, such as heat, carbon dioxide, and carbon monoxide. The aircraft industry has traditionally used smoke detector technology in cargo compartments. This type of instrumentation will alarm in the presence of smoke particles and also in the presence of many other small airborne particles such as dust or condensation. The current ratio of cargo compartment smoke detector false alarms to the detection of actual fires is approximately 100 to 1. This excessive false alarm rate could be reduced with the use of multicriteria fire detectors that would only respond in the presence of more than one component from an actual fire. The alarm algorithm presented in this report was developed through testing of a variety of burning materials and nuisance alarm sources in a narrow-body aircraft cargo compartment. The project also used a computational fluid dynamics model that predicts the transport of combustion products throughout a cargo compartment. The model was used to determine the effective range of the alarm algorithm to successfully detect fires in less than 60 seconds. The algorithm used a combination of threshold values and rate of rise of smoke particles measured with photoelectric and ionization detectors along with temperature and carbon dioxide gas measurements to successfully detect all test fires in less than 60 seconds and to achieve 100% immunity from nuisance alarm sources.

1. INTRODUCTION.

1.1 BACKGROUND.

Fire onboard an aircraft represents a dangerous in-flight situation. One critical area is the cargo compartment, which is mostly inaccessible during flight [1]. Although in-flight fires are rare, the consequences can be disastrous. False in-flight fire alarms produce their own consequences as well. As long as the crew is unable to differentiate between a true and a false warning, it has to follow certified procedures. The impact of the false fire or smoke warning in nonaccessible compartments is extensive and might include flight diversion, declaration of emergency situation that eventually leads to passenger evacuation, compartment inspection, fire extinguisher replacement, customer and passenger disappointment, and loss of confidence in the warning system [2].

The two main types of smoke detectors that are currently used for aviation cargo compartment fire detection are the photoelectric smoke detector and the ionization smoke detector. The photoelectric smoke detector works through a scattering of light principle, whereas the ionization smoke detector is based on a voltage/current drop principle. The operation of both detectors is thoroughly discussed in section 3. Previous research has shown that the photoelectric smoke detectors are more responsive to visible particles (larger than 1 micron) produced from smoldering fires [3]. Ionization detectors are more responsive to invisible particles (smaller than 1 micron) produced by most flaming fires [3]. Photoelectric detectors are used as the primary method of smoke detection in aircraft cargo compartments. Ionization detectors have a tendency to malfunction in environments of varying altitude and pressure, but are still in use to a smaller extent in cargo compartments and aircraft lavatories.

Current aircraft cargo compartment fire detection systems, which are primarily photoelectric smoke detectors, have false alarm rates as high as 99% [4]. False alarms are produced when particles produced from various nonfire sources disrupt the path of the light beam within a photoelectric detector. For ionization detectors, false alarms are obtained when small non-fire-related particles saturate the ionization chamber and obstruct the voltage/current between the plates in the chamber. Temperature, humidity, and pressure gradients in the compartment can lead to fog formation. Fog may form through supersaturation of humid air due to rapid pressure decrease and adiabatic cooling during takeoff and ascent [5]. Fog particles can lead to false alarms by scattering the light beam in a photoelectric detector. Furthermore, cargo or freight containers may emit dust or similar nuisance sources that also constitute a false alarm in both detectors. Current gas detection systems also fall short of the ideal; tests of commercially available carbon monoxide (CO) detectors showed various failures that included false alarms at low CO levels, and worse, no alarms at dangerous CO levels [6].

From the numerous in-flight changing conditions in the cargo compartment stated above, it was evident that implementing a more advanced fire detection system in the cargo area would essentially provide safer aircraft operation. The goal was to reduce the false alarm rate drastically and to improve safety and reliability through increased sensitivity. The number of incidents of false alarms from aircraft cargo compartment detection systems has been steadily increasing as the number of aircraft in the U.S. fleet increases [4]. This means that the ratio of

false alarms to the detection of actual fires is also on the rise; approximately on the order of hundreds to one [4]. Statistics like these require immediate attention to fire detection systems used on aircraft today.

1.2 OBJECTIVES.

Aircraft fire sources and their combustion mechanisms and products are diversified; therefore, there is no single physical parameter that would allow the detection of this wide fire spectrum [7]. Gas concentrations, temperature fluctuations, and particulate levels are three main parameters that make up their diversification. The objective was to develop and test a multisensor detector that used a common household ionization smoke detector, thermocouple, smokemeter, and a CO/carbon dioxide (CO_2) gas probe. These four sensors that make up the multisensor detector were housed in a recessed pan built into the ceiling of a Boeing 707 forward cargo compartment, which was the experimental test volume. A selection of real fire sources and nuisance sources were ground tested in order to produce a matrix revealing fire signature data from all four sensors. Specific fire signatures, such as percent light transmission per foot, temperature rise, gas concentration levels, and voltage drop, were measured to characterize each fire and nuisance source. Smoke density measurements for light obscuration were measured through the smokemeter, temperature changes through the thermocouple, combustible gas concentrations of CO and CO_2 from the gas probe, and voltage differences from the ionization chamber. Rates of rise measurements were also calculated for the data collected by all four sensors. All fire signatures were characterized not only by changes from the ambient of each sensor, but the rate of change from each sensor. The results obtained from these sensors produced a matrix of fire and nuisance source characteristics that were used in specifying alarm thresholds for multisensor alarm algorithm development.

A series of logic-based algorithms representing the multisensor detector was developed based on the matrix criteria and then compared to conventional aircraft smoke detectors. Once an optimized algorithm was developed for the multisensor detector, the physical range was determined through a series of computational testing done with a computational fluid dynamic (CFD) model developed by Sandia National Laboratories. This CFD model is a computer code that predicted smoke, heat, and gas species transport in cargo compartments [8]. The purpose was to establish agreement between experimental and computational results, which was necessary before using the CFD to estimate the physical radius of successful operation for the multisensor detector. By validating the CFD model with experimental results, it eliminated numerous experimental tests within the B-707 forward cargo compartment for spatial distribution analysis. Determining an acceptable range for the detector was essential for packaging, deployment, and implementation purposes for not only the B-707, but for other aircraft as well. The CFD model could then be used as a virtual detector for testing of the multisensor detector in various types of cargo compartments.

2. REVIEW OF LITERATURE.

2.1 HISTORICAL OVERVIEW.

The U.S. Federal Aviation Administration (FAA), along with other regulatory agencies throughout the world, require that cargo compartment fire detection systems provide a visual

indication to the flight crew within 1 minute of the start of a fire [9]. The detection systems most commonly used in aircraft cargo compartments have predominately been reflected-light smoke detectors and, to a smaller extent, ionization smoke detectors [8]. This method of fire detection has been the technology of choice by the aircraft manufacturing industry for at least the last 30 years [8]. Through Technical Standard Order (TSO)-C1d, the FAA requires that detectors meet standards referenced in SAE Aerospace Standard (AS) 8036 (wherein Underwriters Laboratory (UL) smoke box testing is referenced as appropriate to check alarm sensitivity), which specifies that the alarm must fall between 60 to 96 percent light transmission per foot (%LT/ft) [10].

Although UL Standards 268 requires alarm criteria to be evaluated at 2.1% obscuration per foot for the photoelectric residential detectors, cargo compartment detectors are designed to alarm at smoke levels between 4% and 40% obscuration per 0.305 meter or foot [10]. It is necessary to set the detection threshold at a lower level to compensate for typical particulate background levels and alleviate the possibility of a false alarm. Aircraft cargo compartment detection systems are designed to meet performance criteria laid out in Title 14 Code of Federal Regulations (CFR) Part 25.858, "Cargo or Baggage Compartment Smoke or Fire Detection Systems."

This states the following:

> "If certification with cargo or baggage compartments smoke or fire detection provisions is requested, the following must be met for each cargo or baggage compartment with those provisions:
>
> (a) The detection system must provide a visual indication to the flight crew within one minute after the start of a fire.
>
> (b) The system must be capable of detecting a fire at a temperature significantly below that at which the structural integrity of the airplane is substantially decreased.
>
> (c) There must be a means to allow the crew to check in flight, the functioning of each fire detector circuit.
>
> (d) The effectiveness of the detection system must be shown for all approved operating configurations and conditions."

2.2 CARGO COMPARTMENTS.

In a typical passenger transport aircraft, the approximately cylindrical fuselage is separated into the main deck and the lower cargo compartments by the floor of the main deck [11]. In typical cargo transport aircraft, the entire single deck is used for cargo. Aircraft cargo compartments are classified as Class A, Class B, Class C, or Class E [12]. Class A compartments are limited to a small container for use by flight crews and must be located around a crew duty station. Class B are accessible compartments or passenger carrying aircraft equipped with fire detection systems and rely on crewmembers to fight a fire with hand-held fire extinguishers. Class C are typically

inaccessible compartments on passenger carrying aircraft that are equipped with fire detection and suppression systems. Class E compartments are limited to all cargo aircraft and are equipped with fire detection systems. The cargo compartments on transport category aircraft are located inside the pressurized portion of the aircraft where the pressure lies between ambient ground atmospheric pressure to approximately the pressurization level at 8000 feet, 0.69 atmosphere [11].

2.3 TRANSPORT OF CARGO.

Cargo can be loaded in two different ways, either through individual cargo containers for large shipments or bulk loading of passenger luggage. The contents of cargo compartments range from clothing and other fabrics, to perishable items, such as fruits, vegetables, and even livestock [11]. To transport these types of organic cargo, the compartments must provide a specifically conditioned and controlled gaseous environment. Such organic cargo provides greater risk of nuisance alarms for the following reasons:

- Vegetation must be sprayed prior to compartment door closing, leaving a residual aerosol in the compartment.
- Livestock are a source of humidity and in addition emit CO_2, CO, and hydrocarbons.
- Dust becomes circulated in the compartment during the loading and unloading of cargo.
- Aircraft air intake may pick up exhaust emissions from taxiing aircraft and ground vehicles used for loading and unloading.

Fire detection systems must be intelligent enough to decipher between the nonfire and real fire alarms in order to alleviate the problems created by transporting such a broad range of cargo. A more definitive fire signature must be compiled along with a detection system that is programmed to alarm to the specific characteristics of the fire signature. Measurements of gas concentrations and particulate levels from the above cargo must be reported so that detector sensitivity is set above these background levels [11].

2.4 CURRENT TECHNOLOGIES.

“Currently, existing regulations do not preclude the use of any detection technology other than smoke particle detection or in combination with smoke particle detection [8].” To provide a safer flying environment, it was important to consider present technological advances in the field of aircraft cargo compartment fire detection. Multisignature alarm algorithm technology was one of many innovative detection methods that made significant improvements to aircraft fire safety. Video-based cargo verification systems, semiconducting fire gas detectors, and light emitting diode (LED)-based sensors were three important technologies that are discussed briefly in sections 2.4.2-2.4.4 to provide an overview of how much extensive research was done in this field in the past decade.

2.4.1 Multisensor Detectors and Algorithms.

An extensive amount of research has been done in the field of multisensor fire detection systems. The Building and Fire Research Laboratory at the National Institute of Standards and Technology (NIST) in Gaithersburg, Maryland, had conducted a series of fire and nuisance source tests in a fire emulator/detector evaluator (FE/DE). Two separate flaming, smoldering, and nuisance scenarios tailored for aircraft cargo compartments were emulated in the FE/DE to determine potential sensor combinations of gas, thermal, and particulate readings [13]. Measurements of laser light extinction, temperature, gas concentration, and analog output from photoelectric and ionization detectors at the test section were made to characterize the fire and nuisance sources [13]. The alarm threshold levels of fire gases, radiation, temperature, or other characteristics of fire must be specified [11]. This was similar to the present experimental testing that was performed in the B-707 cargo compartment to produce a matrix of data for determining thresholds for the multisensor algorithm.

The NIST FE/DE facility allows smoke detector manufacturers to see how their products react to vapor, varying humidity levels, smoke produced by different kinds of fires and even gases such as CO [13]. The experiments done in the FE/DE produced particulate, combustion gas, and temperature rise values that may be used to identify sensor combinations to discriminate between fire and nonfire scenarios. The next step would be the selection of various multisensor algorithms that can be tested through a simple logic-based program for optimum performance. This report extends experimental research to another level where it can be implemented for designing a multisensor detector through specific algorithms. This report experimented with a wider distribution of fire and nuisance sources to produce a more complete fire-signature matrix. The nuisance sources tested were selected based on anecdotal information from discussions with various industry groups about smoke detection systems in general. The levels of the individual nuisance sources tested were somewhat arbitrary but represented the levels that would cause a false alarm in typical aircraft smoke detectors.

Another type of advanced multisensor detector for aircraft present today is the two-dimensional multidetection fire sensor. The purpose of this sensor was to identify all phases of a fire by independent analysis of each stage shown below [14].

- Smoldering: Period during which heating begins and gasification occurs.
- Chemical Reaction: Period where complete development of pyrolysis occurs.
    - Ignition point sets off the beginning of combustion
    - Smoke emission observed
    - Moderate convection observed
- Flame: Fast exothermic reaction
    - Beginning of the flame, radiant energy generated around the flame
    - Completely developed fire, thermal convective energy
    - Smoke emission of hydrocarbons

The use of infrared detectors allowed for the detection of hot spots and radiant energy measurements emitted by the flame as the chemical reaction occurs [14]. For measurement of high temperatures associated with the flaming stage, two-dimensional sensors working in the very short wave spectrum yielded more precise results than traditional infrared cameras [14]. The hot spot was detected by using a thermographic camera, which was based on the analysis of the hot spot's luminance energy. Fire detection was based on analysis of the fluctuation of the flame's energy, whereas smoke detection, smoldering stage, was similar to that of the photoelectric principle and the light reflection transmission [14].

The National Aeronautics and Space Administration (NASA) Glenn Research Center also applied their expertise in MicroElectroMechanial Systems (MEMS) chemical sensors to this new multisignature fire detection concept. The MEMS sensor system developed by the NASA Glenn Research Center included a miniaturized CO and CO_2 gas sensor, a smoke particle detector, and integrated software [15]. The multisensor package compared various gas concentrations and smoke particle sizes to those values characteristic of an actual fire [15]. Tests of NASA's MEMS-based sensor system were also conducted at the FAA William J. Hughes Technical Center in the B-707 cargo compartment and yielded a successful zero false alarm rate when subjected to dust particles and high humidity levels [15]. The multisensor package sensed the onset of fire equally as well as conventional smoke detectors. The multisensor detector developed by NASA contained only two of the four detectors that were used in the multisensor detector that was analyzed in this project. Therefore, it would be safe to expect that a detector consisting of more sensing technologies would perform at a level comparable to or even surpassing the performance of a detector containing fewer sensors. With the additional thermal sensing capabilities and ionization technology implemented by the multisensor detector that was analyzed in this project, the result was a fire detection system that worked to effectively recognize the presence of fires while screening out false alarms.

With the development of multisensor detectors, alarm algorithm technology had gained increasing acceptance and attention since the late 1990s. NIST had been the pioneer for testing of smart smoke alarms with algorithm technology since 1998 [13]. Since then, numerous private industries and universities participated in joint efforts with government agencies such as NASA and the FAA to assess the feasibility of reducing false alarms through the use of combining smoke detectors. One study, conducted in 1999 by Hughes Associates in Baltimore, Maryland, involved the use of a conventional ionization detector with a CO gas sensor [16]. Patented alarm algorithms consisted of the product of smoke obscuration and the change in CO concentration [16]. Many of these earlier multisensor detectors focused on an alarm algorithm using fuzzy logic and neural networks for event classification and discrimination between fires and nuisance sources [16]. The majority of smoke detection projects were conducted for residential purposes only, not specifically for aircraft cargo compartments. A study conducted by the Department of Fire Protection Engineering at the University of Maryland produced advanced fire detection algorithms for use in residential occupancies [17]. Data from a home smoke detector project was analyzed to produce three algorithms yielding the best sensitivity and nuisance immunity. The three algorithms involved a combination of the following: temperature rise and CO; CO and ionization detector; and temperature rise, CO, and ionization detector [17]. Although algorithms designed for home smoke detector projects were not applicable to aircraft due to the varying

environmental conditions experienced during flight, detector combinations were still strongly considered for such applications.

2.4.2 Video-Based Detection.

A video-based Cargo Fire Verification System (CFVS) for commercial aircraft was developed to address the problem of frequent false smoke alarms that particularly concern long-range flights [5]. The system used low-cost charge-coupled device (CCD) cameras operating in the near infrared range to directly detect fire and hot spots [5]. In addition, LED illumination units were switched on and off to obtain images that were analyzed to detect obscuration. The CFVS was the first vision system suitable for actual deployment in a commercial aircraft. Experiments were done in the cargo compartment of the Airbus A340, and even though the CFVS was developed for this particular aircraft, it may be modified for other aircraft as well [18].

2.4.3 Semiconducting Gas Detector.

Current developments show that gas-sensing technologies have a potential to be new or additional fire detectors. Semiconducting gas sensors work on the principle of adsorption and desorption of gas molecules [19]. The sensors are able to detect gas concentrations and rate of rises selected for specific species produced from combustion. Sensor characteristics depend on the partial pressures, temperature, flow rates, and the sensor history [20]. Changing environmental conditions like temperature, airflow, pressure, and humidity put a burden on gas sensors. A high change in humidity influences the adsorption and reaction of other gas molecules such as oxygen-hydrogen groups on the sensor surface, which has a direct effect on the sensor signal [20]. Immunity against multiple false alarm sources, vibrations, electromagnetic effects, high reliability, and simple maintainability are challenges for such devices [20]. A change of the environmental temperature leads to a change in the sensor temperature and behavior.

Methods to stabilize the temperature by heating the sensor through radiation heaters in hybrid technology have been tested. An aircraft manufacturer has selected three experimental gas sensors for further analysis. These semiconducting gas sensors have been integrated into conventional optical smoke detectors for further analysis to aid in the detection of real fires [20]. The certification of new fire gas detectors in aircraft application is not currently clarified and requires further definition [20]. Due to safety considerations from igniting actual fires in-flight, theatrical smoke generators were used for integration test in the aircraft. These generators, however, did not yield the gas effluent stream produced by real fires.

2.4.4 Rugged LED-Based Detector.

The principle behind this technology is optical absorption spectroscopy technique [21]. Key gases produced by incipient fires are detected by optical absorbance measurements using inexpensive, rugged, mid-infrared LEDs [21]. Carbon dioxide is an important gas to monitor because its nonzero (approximately 350 parts per million (ppm)) ambient concentration allows the detection system to automatically confirm correct performance. Monitoring both CO and CO_2 reduces false alarm rates because the ratio of these gases due to combustion is known and should be significantly different from that due to biological cargo [22]. Spectroscopic detection

of CO and CO_2 is possible using commercially available LEDs with a 4.6-micrometer wavelength [21]. Two techniques are used to measure concentrations of CO and CO_2, direct absorption measurements using a single LED and differential absorption measurements using two LEDs [21]. It was found through experimentation that the differential absorption technique has a higher sensitivity than the direct absorption technique. This system is ideally suited for continuous monitoring in situations that require a small, low-cost alternative to conventional systems, such as in aircraft cargo compartments [21].

3. EXPERIMENTAL APPARATUS.

3.1 GENERAL DESIGN.

All experiments were performed at the FAA William J. Hughes Technical Center with the support and supervision of the Fire Safety Branch staff. An experiment was designed to study the effects of implementing a multisensor detector for improved fire safety in aircraft cargo compartments. Tests were conducted in the forward (fwd) cargo compartment of a B-707 fuselage. Figures 1 and 2 are diagrams of the B-707 forward cargo compartment with dimensions and total volume measurement.

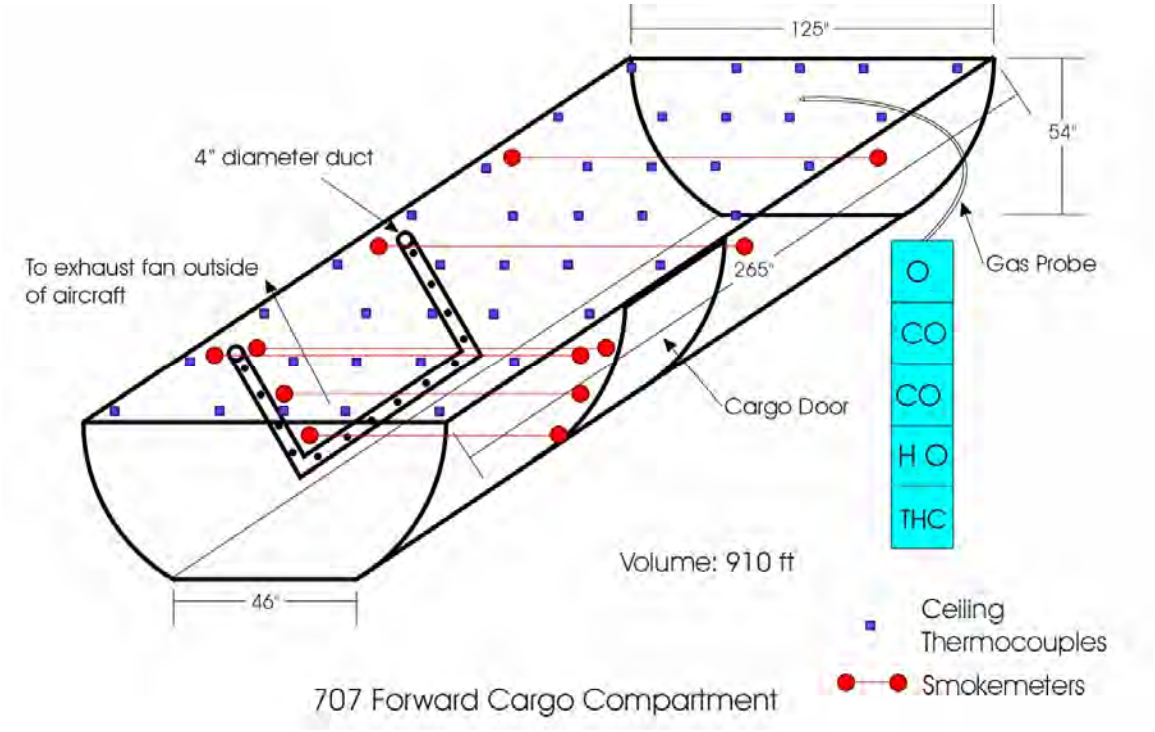

Figure 1. Three-Dimensional Side View of B-707 Forward Cargo Compartment With Instrumentation

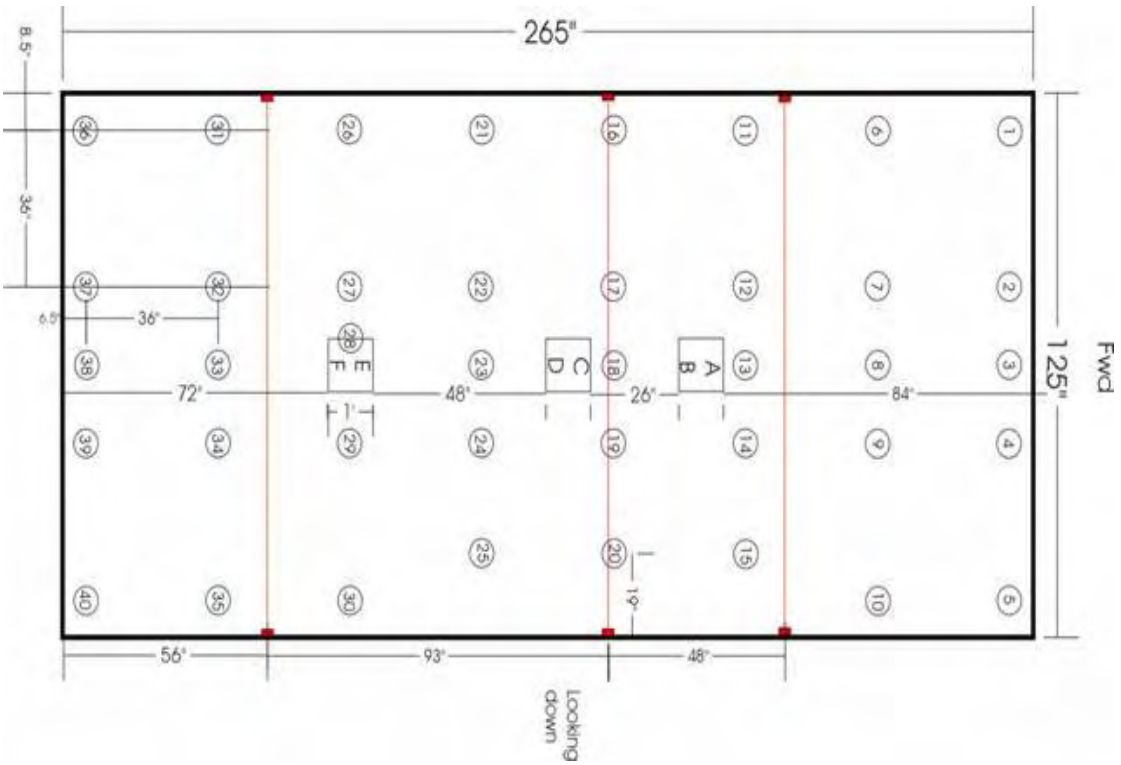

Figure 2. Two-Dimensional Top View of B-707 Forward Cargo Compartment

The schematics also visually depict the locations of all ceiling thermocouples. The smokemeters shown in both figures were used for purposes of testing functionality and accuracy of the instrumentation installed for this project.

All instrumentation for this project was installed in the central recessed pan region, location C-D in figure 2, where typically a conventional smoke detector would be mounted. The dimensions of the recessed pan were 8 inches wide by 8 inches long with a depth of 2 inches. A common household ionization smoke detector, thermocouple, smokemeter, and a gas probe were housed in the pan built into the ceiling of the B-707. Figure 3 shows the recessed pan region in the gray along with all four sensors mounted within the pan.

Housing the sensors in the recessed pan enabled experimental testing to accurately recreate detector responses from fire and nuisance scenarios in a cargo compartment and produced the most accurate measurements from each instrument. For the smokemeter laser measurements, the signal was passed through an op-amp to boost the signal-to-noise ratio for smaller fluctuations and more accurate measurements of percent light transmission per foot. The gas probe line extended from the recessed pan to an adjacent trailer that contained the gas analyzers and associated equipment. There was an approximate 8-second time lag for the gas probe measurements to reach the analyzers, which was accounted for in the analysis.

All instrumentation was interfaced to a data acquisition system in a control room where the outputs from each detector for each experiment was saved to a computer file for analysis.

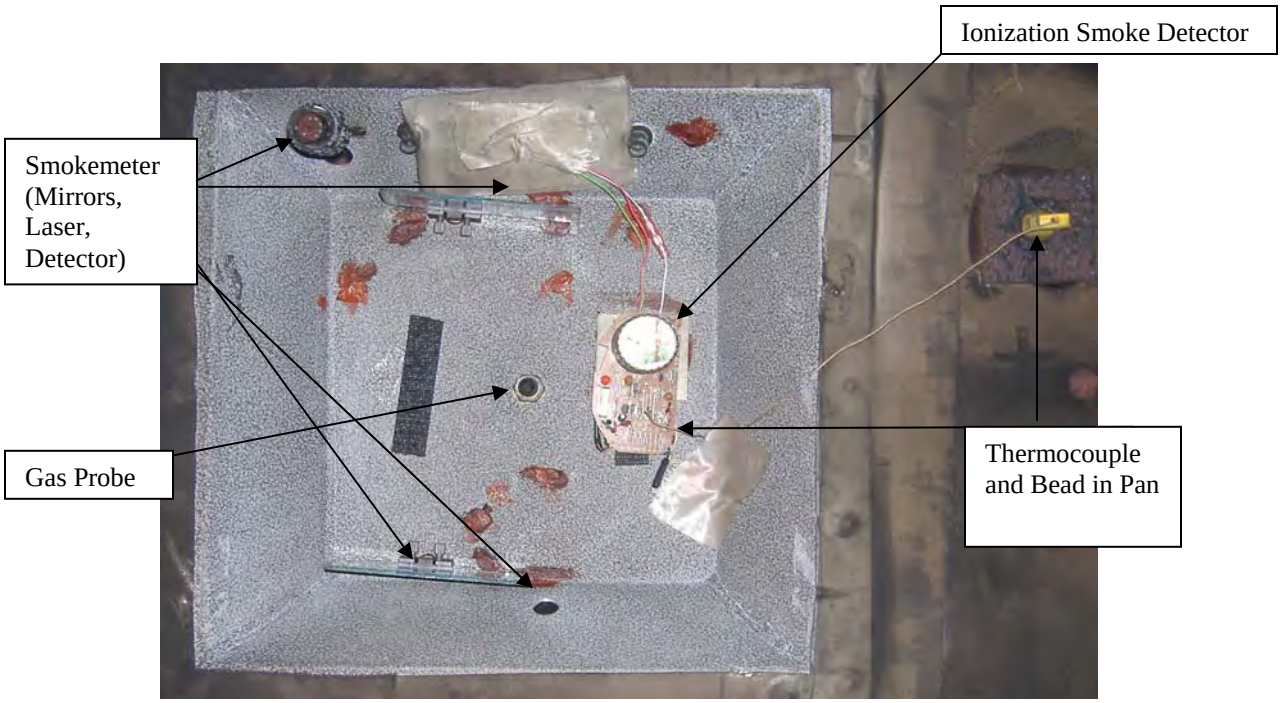

Figure 3. Recessed Pan Including All Sensor Instrumentation

Measurement units used for smoke detection in this project were percent light transmission per foot. These units were selected to allow direct comparison with the alarm point units used in TSO-C1d and the calibrated alarm points specified on aircraft smoke detectors. The ionization detector outputs data in volts, which is converted to a detector alarm point, as discussed in sections 3.2 and 3.4.3. The saved data could readily be exported to a Microsoft® Excel® spreadsheet for data processing.

3.2 MEASURING IONIZATION CHAMBER.

The Measuring Ionization Chamber (MIC) device is based on the ionization principle. Ionization theory stems from the existence of alpha-radiation particles amongst two plates with a voltage across them. "Ionization sensor smoke alarms contain a small amount of radioactive material, americium, embedded in a gold foil matrix within an ionization chamber. The matrix is made by rolling gold and americium oxide ingots together to form a foil approximately 1-micrometer thick. This thin gold-americium foil is then sandwiched between a thicker (~0.25 millimeter) silver backing and a 2-micron-thick palladium laminate [23]." This is thick enough to completely retain the radioactive material, but thin enough to allow the alpha particles to pass. The alpha particles ionize the oxygen and nitrogen atoms of the air in the chamber [23], shown in figure 4. This leaves a free electron with a negative charge and an atom missing one electron with a positive charge. The negative electron is attracted to the plate with a positive voltage, and the positive atom is attracted to the plate with a negative voltage. An electrical current is created across the two plates due to these electrons and ions. Figure 4 is a schematic of the two plates, with voltage applied in the ionization chamber.

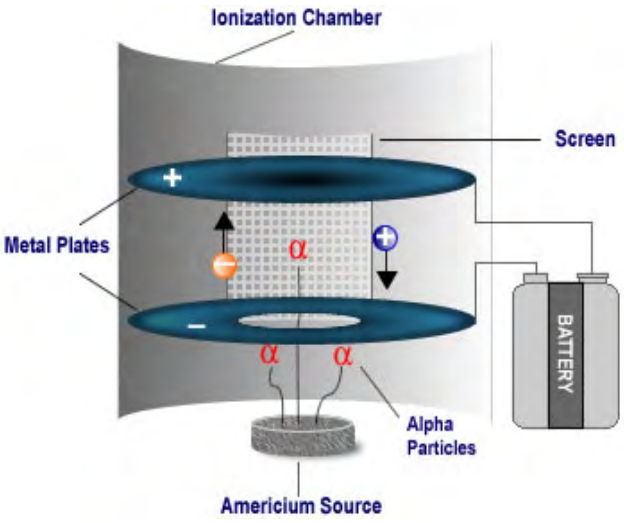

Figure 4. Ionization Chamber in Clean Air [23]

Figure 5 shows when smoke enters the ionization chamber, it disrupts this current. On the molecular level, the smoke particles attach to the ions and neutralize them. The smoke detector senses the drop in current between the plates and activates an alarm at predetermined threshold. This is all controlled on an integrated circuit chip on the circuit board of the smoke detector.

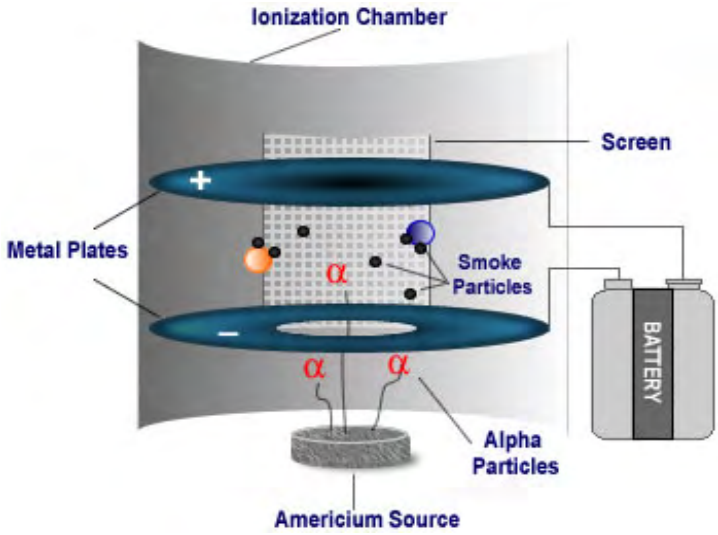

Figure 5. Ionization Chamber Subjected to Smoke Particles [23]

To understand how an ionization type smoke detector responds to different fire sources, quantitative measurements must be taken. An ordinary household residential ionization smoke detector was sufficient enough to produce results of the chamber voltage, in essence, creating a custom-made MIC. The ionization chamber is the part of the ionization smoke detector that contains the alpha radiation particles and provides the two plates with an applied voltage. On the integrated circuit chip of a Kidde Ionization Smoke alarm, model #0915K, the output pin from the ionization chamber was located (as discussed in private conversations with Tom Cleary and

Kidde engineers). Two wires from a variable power supply, which was kept constant at 9 volts, were soldered to the common and input pins on the circuit board of the detector. Two wires from the analog to digital analyzer were soldered to the common and output pin from the ionization chamber. In doing so, voltage output readings from the ionization chamber could be collected through the data acquisition system.

All Kidde ionization smoke alarms yield an output voltage between 2/3 and 5/9 of the input voltage (approximately 9 volts) for clean air. For the particular detector used in this research, the reference voltage for clean air was approximately 5.1 volts. This was the reference point, or the constant output voltage for a scenario with clean air, meaning no fire and no interferences.

TSO-C1d requires that detectors meet standards referenced in SAE AS 8036, which specifies that the alarm must fall between 60 to 96%LT/ft [10]. For purposes of analyzing the data, a correlation between the voltage output of the chamber and percent light transmission would need to be calculated. Finding a direct correlation between voltage output and percent light transmission was not trivial; in fact, there was no single correlation coefficient that sufficed for all fire sources. Each fire source would demand its own correlation coefficient for accurate conversion from volts to percent light transmission. An alternative method to determine the voltage at which this particular ionization detector will result in an alarm was conducted. The MIC was removed from the recessed pan and was wired, as shown in figure 6.

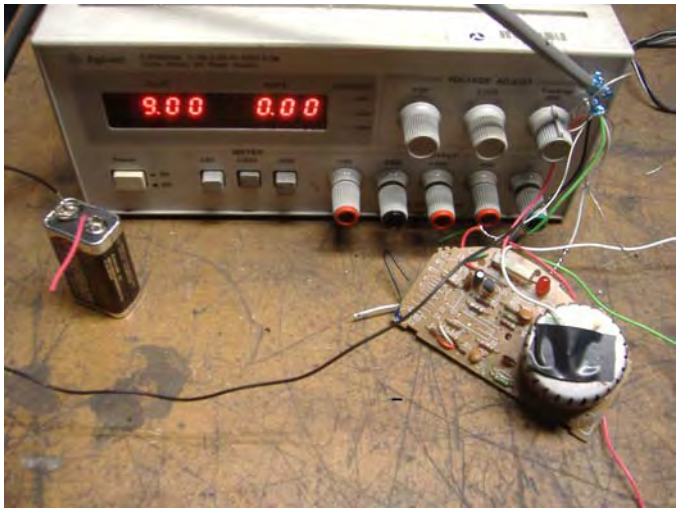

Figure 6. Alarm Threshold Detection Method Setup for MIC

The idea behind this alternative method was to manually adjust the ionization chamber voltage across the plates to simulate smoke in the chamber. A regular 9-volt battery was connected to the detector to supply power to the entire system. In addition, a variable power supply was connected to the chamber to manually regulate the voltage generated between the plates. The wiring for the collection of the voltage output readings from the ionization chamber remained the same. The reference voltage for clean air remained the same at 5.1 volts. The variable power supply, starting at the primary position of 9 volts, was then gradually decreased, and simultaneously, the ionization chamber voltage output collected by the data acquisition system revealed a slow decline from the clean air reference voltage. The voltage was decreased until the

detector went into alarm mode, when the output voltage from the chamber was noted. The process was repeated several times for repeatability purposes and eventually revealed the alarm point of this particular detector to be approximately 4.1 volts, 1 volt below reference voltage.

3.3 SMOKEMETER.

The last part of the experimental setup was designing a way for detecting the smoke density in the recessed region where a typical photoelectric smoke detector would be. Before discussing the experimental setup of the smokemeter apparatus, it is important to understand the principle behind a photoelectric smoke detector. The main principle by which the photoelectric smoke detector works is through the scattering of light [24]. Inside the smoke detector there is a light and a sensor positioned at 90-degree angles to one another [24]. Figure 7 represents the standard setup of a photoelectric detector.

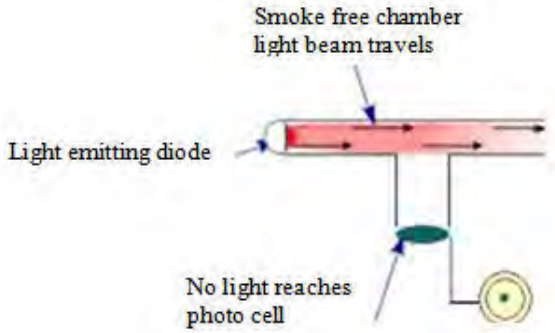

Figure 7. Photoelectric Detector in Clean Air [24]

In the normal case, the light from the light source on the left shoots straight across and misses the sensor. When smoke enters the chamber, however, the smoke particles scatter the light and some amount of light hits the sensor [24]. Figure 8 depicts this scenario where the smoke particles scatter the beam of light. The sensor then activates the alarm circuit in the detector. The alarm thresholds for photoelectric smoke detectors vary among different manufacturers. For common, household photoelectric smoke detectors, UL Standards 268 requires alarm criteria to be evaluated at 2.1 percent obscuration per foot for the photoelectric, or 97.9%LT/ft. However, detectors in aircraft cargo compartments traditionally have lower threshold levels to alleviate the problem of false alarms. For purposes of analyzing this data, results will comply with TSO-C1d, requiring the alarm point to fall below 96%LT/ft.

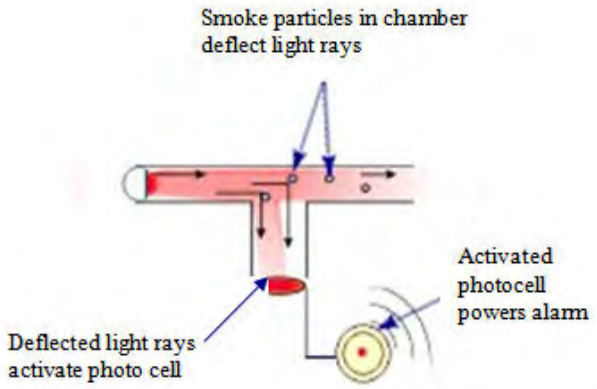

Figure 8. Photoelectric Detector Subjected to Smoke Particles [24]

Two commercial quality first surface mirrors were purchased with the following dimensions: 4-inch length, 1.5-inch width, and 0.13-inch thickness. The mirrors were then installed directly across from each other with an 8.5-inch gap separating them in the recessed region. A High Quality Fixed Laser Diode Module was installed directly across from mirror A in the pan. The laser operated in the 670-nanometer (nm) spectrum and was a fixed-focus circular beam with maximum output of 0.95-mil watts. There was a 6-inch-high compartment that stretched the entire length of the cargo compartment and separated the ceiling of the cargo compartment from that of the main deck floor. The recessed pan was built into this region, like the schematic shown in figure 9.

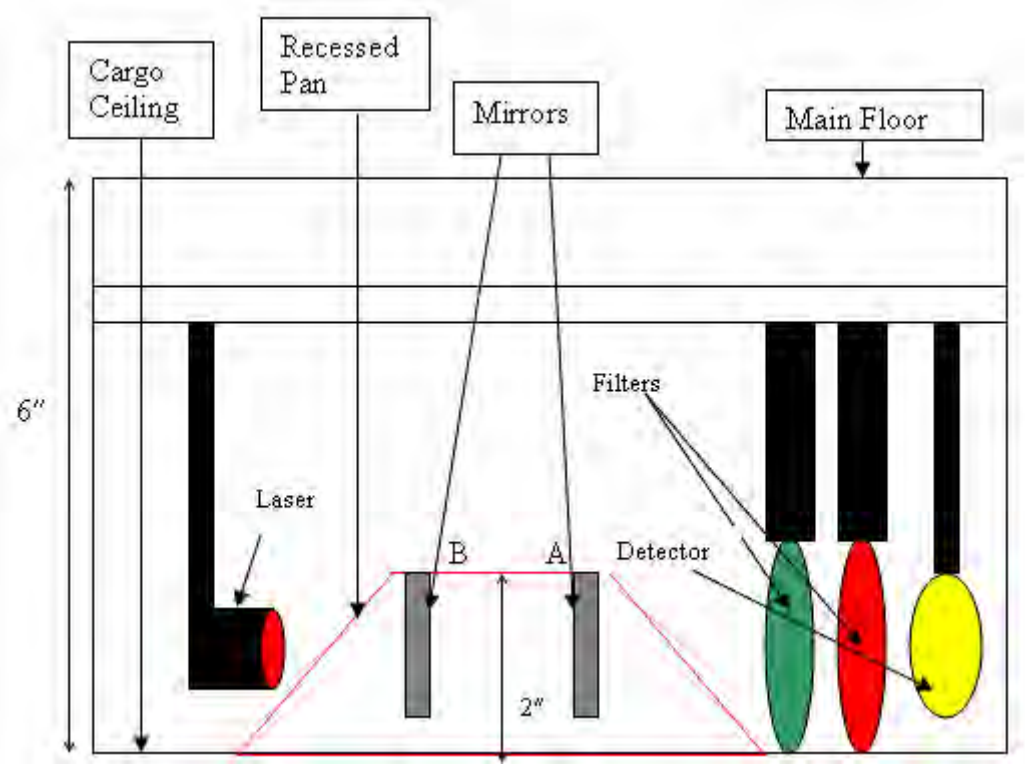

Figure 9. Two-Dimensional Schematic of Experimental Smokemeter Setup in Recessed Pan

The laser was installed outside of the recessed pan region so it would not affect the flow field of the plume from the fire source, which can also be seen in figure 9. The laser was then positioned at approximately a 5-degree angle to mirror A, still keeping it completely parallel with the vertical height of the other two mirrors. The angle that was made was with respect to the vertical plane, moving the laser from left to right, not up and down. This angle was important to produce a series of bounces between the mirrors to obtain light obscuration data in that region. The laser beam was bounced back and forth seven times before passing through the band-pass and infrared filters and finally hitting the coaxial silicon photodetector on the side of mirror A.

Figure 10 is a three-dimensional layout of the general physics and design of the smokemeter apparatus. It consisted of the laser, two mirrors that were offset to preserve surface area for bouncing the laser back and forth, one band-pass filter, one infrared filter, and a silicon photodetector. A path length of 5.17 feet was calculated from the seven laser beam bounces. Optical density measurement tests were then conducted by placing four different filters in front of the photodetector. This was done to verify that the apparatus was accurately recording the transmitted light intensity. The filters had optical density values of 0.22, 0.33, 0.44, and 0.98. The optical density values were converted to light transmission per foot for the 5.17-foot path length and plotted. Figure 11 shows the strong accuracy achieved between theoretical and experimental results of the optical density filter tests. Optical density tests of the smokemeter were performed prior to each experiment.

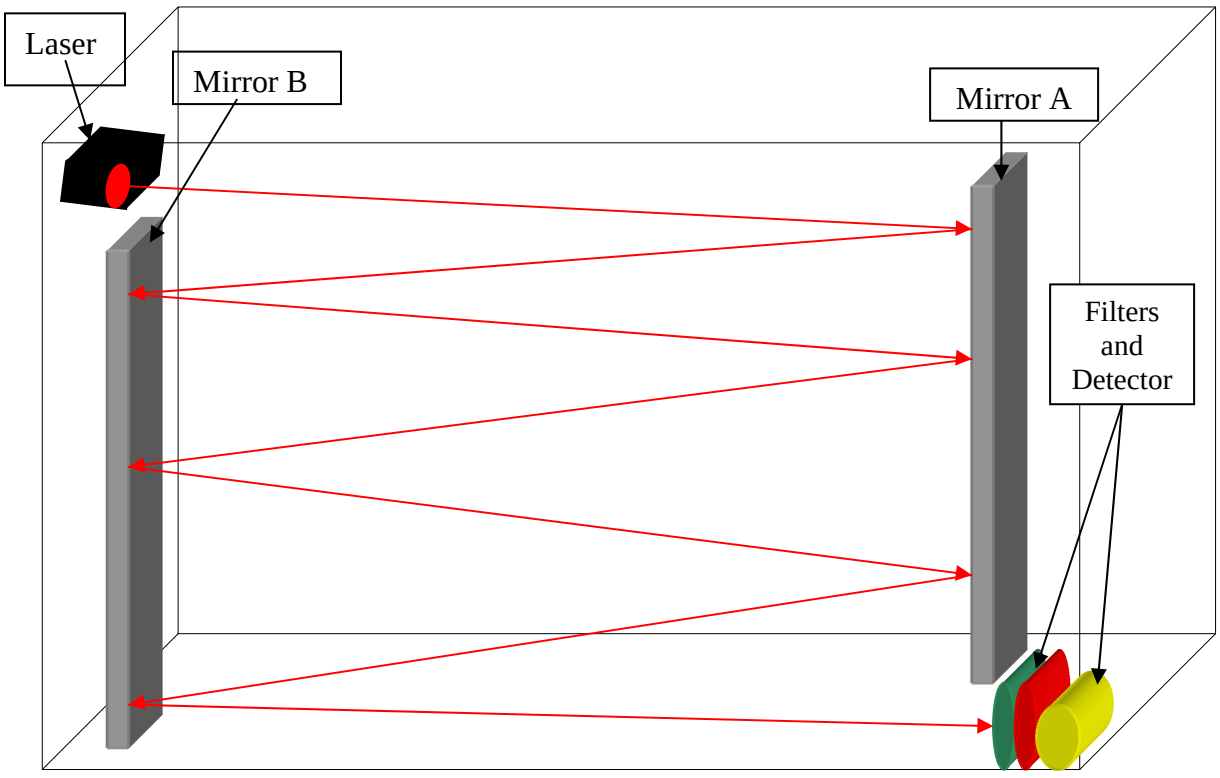

Figure 10. Three-Dimensional Schematic of Experimental Smokemeter Setup in Recessed Pan

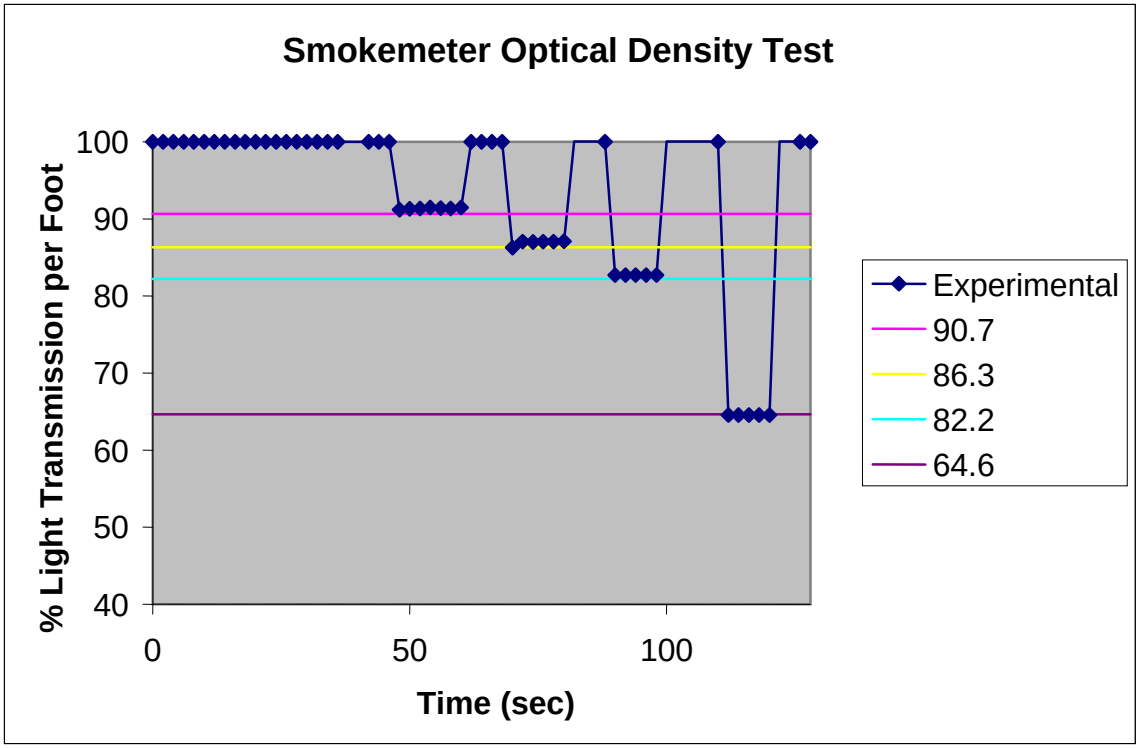

Figure 11. Comparison of Theoretical and Experimental Optical Density Tests for Calibration

3.4 COMPUTATIONAL FLUID DYNAMIC MODEL.

The FAA Smoke Transport Code is a physics-based CFD tool, which couples heat, mass, and momentum transfer. It provides information on smoke, gas species, and heat transport in cargo compartments with varying fire and sensor locations, compartment geometry, ventilation, loading, compartment temperature, and compartment pressure. The fire source term is specified in the model based on FAA experiments that measured the heat release rate, mass loss rate, and species generation rates of a standardized fire source [25]. The code consists of a preprocessor, an analysis module, and a postprocessor. The primary use of this code was to simulate fires in the B-707 forward cargo compartment to obtain relevant spatial distribution information such as the range of the multisensor detector. Results from the computational simulations were then compared to actual experimental results. Agreement between experimental and computational not only aided in validation of the CFD model, but essentially provided a basis for a virtual detector. A virtual detector eliminated the need for experimental testing and provided a more efficient, cost-effective way of determining multisensor detector capabilities and spatial distribution analysis. It was used to identify optimum multisensor detector locations and determine critical sensor levels for the multisensor algorithm. The CFD was used to determine the physical radius of successful operation of the multisensor detector for each specific algorithm. The range was valuable information that was pertinent in assessing the overall performance of the multisensor detector as compared to existing detectors.

The model allows users to work with predefined meshes for specific aircraft, such as the DC-10 and B-707, or allows for the creation of custom geometries. To completely solve a CFD

problem, the model uses a three-phase procedure. The first phase used the preprocessor to define the problem, essentially choosing a mesh or volume for the simulation. At this point, initial and boundary conditions were input. The second phase was the coupling of the preprocessor to the analysis module. The analysis module solves the CFD problem and produced results. The last phase was the postprocessor phase that was used to extract the results from the analysis module. To compare computational to experimental results, necessary conversions were made for light transmission data, gas concentrations, temperature data, and the MIC.

3.4.1 Light Transmission Data Conversion.

To obtain smokemeter readings in the units of percent light transmission per foot, soot concentration, and gas density, data output from the postprocessor was integrated along the total length of the cells that entirely comprised the volume of the recessed pan. Beer's Law, shown below, was then used to obtain the nondimensional light intensity ratio that can be readily converted to percent light transmission per foot [25].

$$\frac{I}{I} = e^{-\int_0^L k(x)dx}$$

$$\text{where } k(x) = C_{soot}(x) * \rho_{cell}(x) * \sigma_s$$

In Beer's Law, σ_s is the specific extinction coefficient ($7400 \frac{m^2}{kg}$), C_{soot} is the soot concentration ($\frac{kg}{kg}$), and ρ_{cell} is the gas density ($\frac{kg}{m^3}$). The specific extinction coefficient value is an accurate average that was based upon previous research on the soot morphology and optical properties from the flaming resin block. The equation below was used to convert the computational data to units of percent light transmission per foot for comparison to experimental data.

$$\frac{\%LT}{ft} = 100 \times \left[\frac{I}{I_0}\right]^{\frac{1}{L}}$$

where L is the original path length of the laser beam in feet [25].

3.4.2 Gas Data Conversion.

To obtain gas concentration data in units of ppm, the output from the model had to be converted from mass fraction units of (kg/kg). The computational concentrations were converted to the experimental concentration units using the following equation [25].

$$C_{gas}(ppm) = C_{gas}(in \frac{kg}{kg}) \times (\frac{\rho_{cell}}{\rho_{gas}}) \times 10^6$$

where

$$\rho_{cell} \text{ and } C_{gas}(in\frac{kg}{kg})$$

were obtained from the computational output, and the densities of CO and CO_2 are 1.145 kg/m^3 and 1.833 kg/m^3, respectively.

3.4.3 Measuring Ionization Chamber Correlation.

Gas concentrations, temperature, and smokemeter values were the only sets of data produced by the CFD postprocessor. Since the CFD model did not produce an output parameter for voltage difference from an ionization detector, an alternative method was found to obtain MIC data from the CFD for purposes of accurately comparing experimental and computational results. Both the ionization type detector and photoelectric detector worked on different principles, but exhibited the same type of declining behavior as their chambers became filled with particles. The decline of each detector was related to the type of fire or nuisance source, flaming or smoldering, and the various particle sizes produced from the fire or nuisance source. An analysis was conducted to find a pattern or simple correlation between the smokemeter and the MIC. Details of this analysis involving correlation curves and polynomial curve-fit equations will be discussed at the end of section 4.2.1.

4. EXPERIMENTAL PROCEDURE.

4.1 EXPERIMENTAL TESTING.

The coordinate system used in the smoke transport model of the B-707 consisted of an x axis that ran laterally across the compartment with the centerline equal to zero, positive x values in the starboard direction, and negative values in the port direction. A y axis ran longitudinally down the length of the compartment with z = 0 at the forward wall and increased in the direction towards the back wall of the compartment. A y axis ran vertically with y = 0 at the compartment floor and increased in the upward direction. Figure 12 shows the directions of the x and z axis.

Initial fire and nuisance source testing occurred at a central position denoted as the x location. The coordinates of this location were x = 0.14 meters and z = 3.81 meters. Figure 12 shows the coordinates of all test locations within the compartment.

This location was chosen as the central position because it was within inches of being directly beneath the recessed pan and also because it was the primary test location for numerous testing done previously in the B-707 cargo compartment. Perimeter testing was performed for the alcohol-soaked rags, shredded newspaper, and polyurethane foam as well. The two furthest distances in the compartment from the recessed pan, the forward starboard corner and the aft starboard corner, were chosen as ideal perimeter testing locations. The forward starboard location was at x = 0.43 meters and z = 0.28 meters. The aft starboard location was at x = 0.43 meters and z = 6.57 meters. Perimeter testing for the resin block involved a total of three locations; the forward starboard corner, the aft port corner, and the sidewall starboard side

location. The aft port location was x = -0.43 meters and z = 6.57 meters. The starboard sidewall location was x = 0.42 meters and z = 1.8 meters.

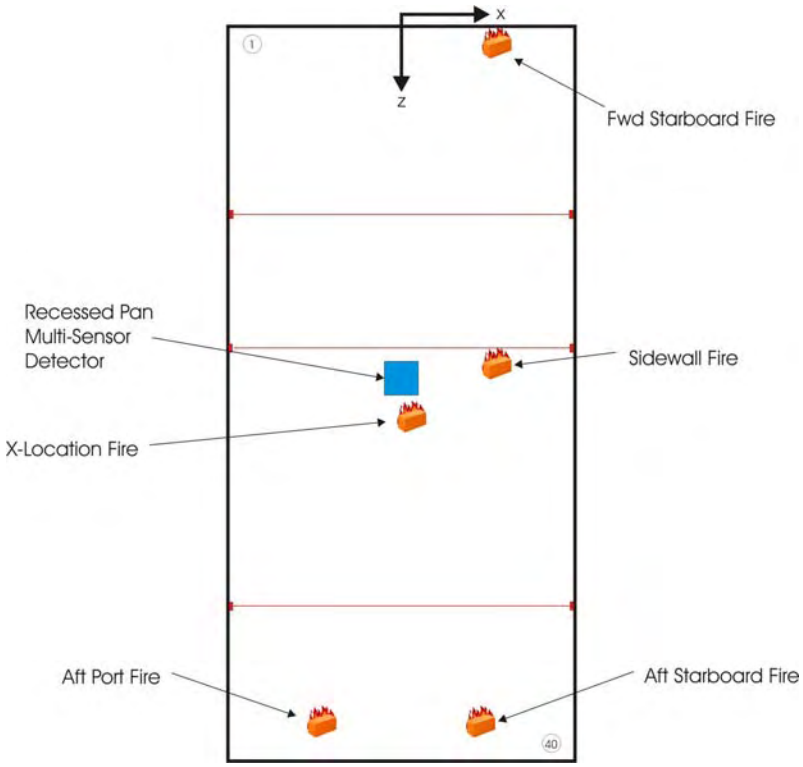

Figure 12. Cargo Compartment Coordinate System and Fire Locations

Experimental testing began with a repeatable fire source developed by the FAA, the resin block, as shown in figure 13. The fire source was comprised of a mix of six plastic resins in pellet form that were heated and pressed into a 4″ by 4″ by 3/8″ molded resin block [26].

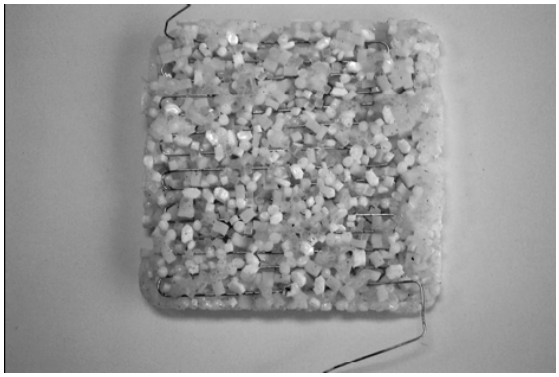

Figure 13. Resin Block, FAA Repeatable Fire Source

The six plastic resins that comprised the resin block were nylon, polyethylene, polyvinyl chloride, polystyrene, polybutylene terephthalate, and polyurethane [26]. Nichrome wire was attached to an alternating current (ac) power supply, embedded within the resin block, and used

as a heat source. A flaming fire source was produced by pouring 2 milliliters (mL) of heptane onto the resin block and simultaneously igniting the heptane and energizing the nichrome wire [26]. At time 0, the spark igniter was turned on and approximately 40 volts from a variable ac power supply was applied to the nichrome wire. Once the heptane had been ignited by the spark igniter and a flame was visible, the spark igniter was turned off. After 3 minutes, the ac power supply was shutoff and the fire continued to burn until it self-extinguished approximately 2 minutes later. The purpose of the standard 5-minute resin block test was to determine the accuracy and functionality of all instrumentation (gas probe, smokemeter, MIC, and thermocouples) since it was a repeatable fire source.

A broad range of real fire sources and nuisance sources were tested in the B-707 cargo compartment. Table 1 lists some brief details of each fire and nuisance source used for experimentation purposes. To ensure repeatability and accurate data collection, each test was conducted at least four times for averaging of the data before analysis.

Table 1. Brief Descriptions of All Real Fire and Nuisance Sources Used for Experimentation

Fire Sources	Nuisance Sources
1. Denatured Alcohol • (40 mL) • 4 minutes • Flaming	1. Vaporizer • Simulation of vapors from rapid pressure changes • 1 1/2 minutes
2. Polyurethane Foam • 9″ x 4″ x 4″ foam block • 4 minutes • Flaming	2. Arizona Test Dust • Simulation of dust from dirty containers or cargo itself • Box setup • 1 minute
3. Alcohol-Soaked Rags • 10-mL denatured alcohol • 1 rag with 1-square-foot area • 4 minutes • Flaming	3. Heat Gun • Simulation of container on hot day and thermal heat released • 2 minutes
4. Shredded Newspaper • 123-in.^{2} pan, 6-in. height • 2 minutes • Flaming and Smoldering	4. Occupied Compartment • Background CO_2 levels • 5 minutes
5. Suitcase • Assorted Fabrics • 5 minutes • Smoldering	5. Exhaust Fumes • Loading vehicle near cargo compartment before door closes • 4 minutes

4.1.1 Fire Tests.

For the alcohol tests, a small metal container was filled with 40 mL of denatured alcohol. At time 0, the spark igniter was momentarily activated to ignite the alcohol and then was switched off. All denatured alcohol tests were performed for 4 minutes.

The procedure for igniting a 9-inch-long, 4-inch-high, and 4-inch-wide block of foam used the spark igniter as well. First, 10 mL of denatured alcohol was used to soak the bottom of the foam block entirely. Then, the foam was pushed onto a 9-inch-long spike with a base, so that the foam entirely covered the spike. The spark igniter was then positioned directly at the base of the apparatus, where the foam block was soaked with alcohol. At time 0, the spark igniter was activated to ignite the foam, and then was switched off. Data was collected for approximately 4 minutes for all foam block tests.

For ignition of the shredded newspaper, a 5-inch piece of coiled nichrome wire was placed at a half-way height of 3 inches, directly in the middle of the pile of paper in the pan. The nichrome wire, which was attached to a variable ac power supply, functioned as a heat source. The idea was exactly the same as that for the heat source in the resin block. At time 0, 40 volts were applied and the sudden heat produced by the nichrome wire resulted in ignition of the pile of shredded newspaper. The shredded newspaper test was the shortest fire test and lasted approximately 2 minutes for a 6-inch-high pile of shredded newspaper in a 123-square-inch pan.

The procedure for igniting an alcohol-soaked rag was almost exactly the same as that of the shredded newspaper. This time however, the use of 10 mL of denatured alcohol was needed to obtain ignition of the rag. The alcohol was poured in the location where the nichrome wire was embedded within the rag, so that when the 40 volts from the variable ac power supply was applied, the heat generated from the wire ignited the alcohol and the rag simultaneously. Data was collected for approximately 4 minutes for all alcohol-soaked rag tests.

The suitcase fire was the primary smoldering fire source and was also the longest fire test. Igniters for the suitcase test consisted of a 15-inch piece of nichrome wire wrapped around a 3-by 8-inch piece of folded paper towel. The idea was the same as that of the alcohol-soaked rags and newspaper; however, a stronger heat element was needed for the suitcase to smolder since alcohol was not being used, hence the paper towel and longer piece of nichrome. The igniter was then placed inside the suitcase that was stuffed with a variety of assorted fabrics. The leads from the variable ac power supply were then attached to the two ends of the nichrome wire igniter source already positioned inside the suitcase. The suitcase was then zippered completely, only exposing an opening where the leads from the power supply to the nichrome were connected. This opening was also helpful in producing a successful smoldering suitcase by allowing oxygen into the suitcase. At time 0, the 40-volt ac power supply was switched on, kept on for approximately 3 minutes, and then switched off for the final 2 minutes of the test. Transition from smoldering to actual flame was possible at any point, depending on the flammability of the fabrics in the suitcase and the heat source at any given time.

After each fire test, the cargo compartment was ventilated until all instrumentation returned to ambient levels. After each individual test, the data collected was saved and exported to a Microsoft Excel file for analysis.

4.1.2 Nuisance Source Tests.

Nuisance tests were easier to implement; however, they were difficult to control. Fine Arizona test dust was used to simulate particulates that could be present within cargo compartments. Arizona test dust was obtained commercially from Powder Technology, Inc. The fine grade of test dust had a mean particle size of 9.1 microns and a standard deviation of 18.3 microns for the full range of particle sizes. An open-topped metal box, shown in figure 14 and measuring 1 by 1 foot by 14 inches high, was constructed to expose the sensors to the test dust. Approximately 10 grams of test dust was placed in the bottom of the box under a tube that directed a stream of compressed air at 60 lb/square inch against the bottom of the box to agitate the dust. The box was initially placed on the floor of the cargo compartment under the recessed pan, but this position did not result in any dust reaching the sensors. The box was then mounted on a small extension piece, measuring 7 1/4 inches high and shown in figure 15, to locate the box closer to the sensors in the recessed pan. This location did result in responses from the sensors to the agitated test dust.

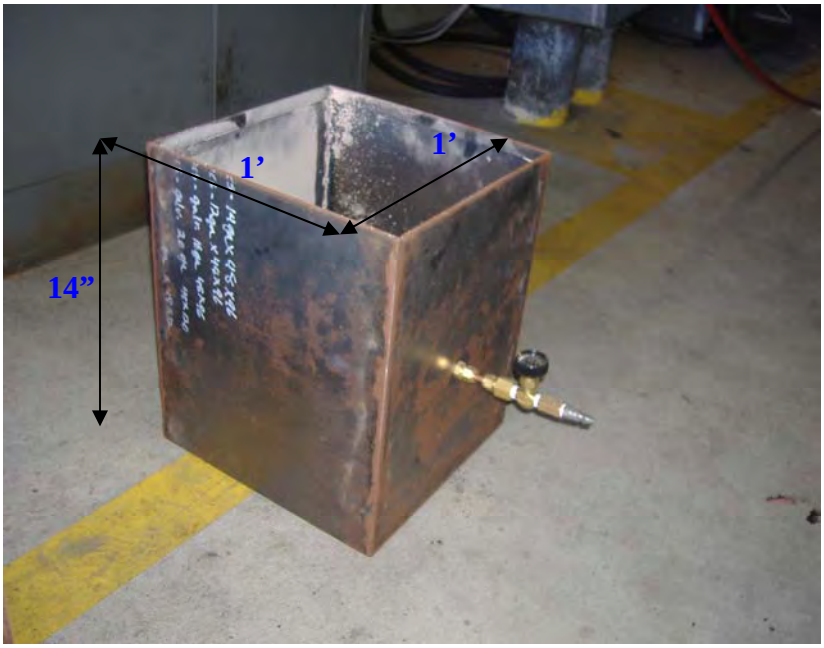

Figure 14. Box Setup Used for Controlled Testing of Arizona Test Dust

Figure 15. Extension Stand Welded for Vaporizer and Arizona Test Dust Tests

To simulate fog formation within the compartment from temperature, humidity, and pressure gradients, a DeVilbiss model #1200 household vaporizer was filled with water and 10 grams of salt. The vaporizer was placed at a location 9 inches off-center from the middle of the recessed pan region towards the starboard corner and 114 inches from the forward bulkhead wall. This location ensured that the vapors would spread directly into the recessed pan region where the detectors were mounted. An issue that was encountered was how much vapors should be allowed to enter the recessed pan region. This was resolved by conducting a few possible test methods. One involved the use of the stand and extension piece from figure 15 screwed together to mount the vaporizer flush against the recessed region. The 10 grams of salt helped to expedite the formation of the vapors to produce a more timely testing process. Immediately after vapor formation, the recessed pan was saturated with moisture, and it was evident that the vaporizer was too close. Tests were then conducted with the vaporizer on the floor; however, this failed to cause the sensors to respond. The vaporizer was then placed on the extension piece from figure 15. This location resulted in sensor responses without oversaturating the recessed pan region with moisture.

A heat gun was used to simulate the thermal energy that could be released from a cargo container sitting on the tarmac on a hot summer day, and then being loaded into the compartment. An industrial-grade variable temperature Master Appliance Corporation VT750 heat gun was placed directly beneath the recessed pan, approximately 39 inches from the ceiling height to the top of the gun itself. The duration of the heat gun experiments was approximately 146 seconds.

The exhaust fumes test was conducted to represent the nuisance scenario caused by the introduction of CO and CO_2 from ramp vehicles adjacent to aircraft with open cargo compartment doors. A common warehouse forklift was used to simulate this scenario. The forklift was positioned just outside the cargo compartment door with the exhaust fumes directed into the compartment through a 4-foot tube with a 6-inch diameter. The test duration for this scenario was approximately 4 minutes.

The final nuisance scenario was the introduction of CO_2 into the compartment from the respiration of personnel present in the compartment during baggage loading and unloading. To test this scenario, an FAA technician was positioned in the compartment just beneath the

recessed pan housing the multisensor detector for approximately 5 minutes. The technician then vacated the compartment, and data was taken for an additional 5 minutes.

4.2 COMPUTATIONAL TESTING.

A CFD model was used to assess validation and functionality purposes of both the model and the multisensor detector. Simulations were setup, run, and analyzed for comparison to experimental tests. Since the heat source term in the CFD model represented the resin block, comparison between experimental and computational results was conducted for only the resin block. For each experimental resin block test, both x location and perimeter tests, an identical test was simulated in the CFD Model for comparison. The computational processing time was approximately 1/2 hour for every 100 time steps on an Intel® Pentium® 4, 3.4 GHz computer with an average of about 1 hour of computational run time for each minute of real time. Although this may have seemed time-consuming, the benefits of the CFD over experimental were far greater. The next paragraph provides a brief explanation of the procedure that was followed to set up fire simulations in the CFD model.

The first step was choosing a particular mesh, or volume, to be used in the simulation. Once a mesh was generated, the built-in preprocessor, which included zoom, pan, and rotate functions, provided visual feedback of the geometry. The preprocessor then could be used to add or delete cells from the mesh, locally refine the mesh, and apply initial and boundary conditions.

Figure 16 displays what the mesh looked like from the front view and the side view, respectively [27]. By refining the mesh, it was possible to customize the dimensions of each cell shown in the figure. For purposes of this project, the cell dimensions were left at default values for the B-707 pre-existing mesh.

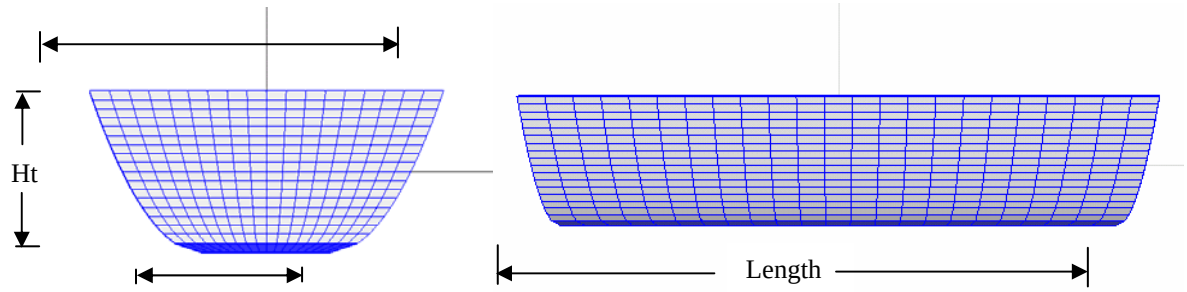

(a) Front View (b) Side View

Figure 16. Computational Fluid Dynamic Model Mesh Used in Simulations

After the mesh was loaded, the wall temperature boundary condition of 293 K and the heat transfer coefficient to the walls of 7.0 W/°Km^2 were input by accessing the mesh drop-down menu. Although the B-707 compartment could be ventilated up to a rate of 17 cubic feet per minute, ventilation was not used in experimental tests, and therefore, no initial conditions for velocity inlets or outlets were necessary for the CFD model. The fire was then placed by selecting the particular cell for the desired location of the fire and then using the Fire Icon on the graphical user interface. The time step was then set to 0.05 second, with an output file printed

every 40 time steps, for the duration of the 300-second simulation. This produced data points every 2 seconds. Computational data was then converted to units identical to those of experimental data for comparison. In sections 3.4.1 and 3.4.2, light transmission and gas concentration conversion equations were presented. To provide a complete comparison of computational to experimental data, a method was devised to produce computational MIC values based on computational percent light transmission data.

Experimental MIC voltage data from numerous experimental resin block tests in the x location were averaged and plotted against experimental percent light transmission per foot data in hopes of finding an appropriate correlation for the resin block. Analysis of figure 17 revealed a correlation of the MIC to the smokemeter in the form of a second-order polynomial with respect to percent light transmission per foot. The polynomial displayed on the graph accurately represented the data curve for both the resin block at the x location and the aft location. The relevant time frame in which the polynomial fit and resin block data curves must be within good agreement to produce accurate results is up until the alarm threshold point for each detector. It appeared that from the reference voltage of 5.1 volts to the alarm threshold point of 4.1 volts, the polynomial accurately modeled the behavior of the experimental MIC data. The polynomial was then substituted to solve for MIC values in the CFD model by using the already converted percent light transmission data from the CFD.

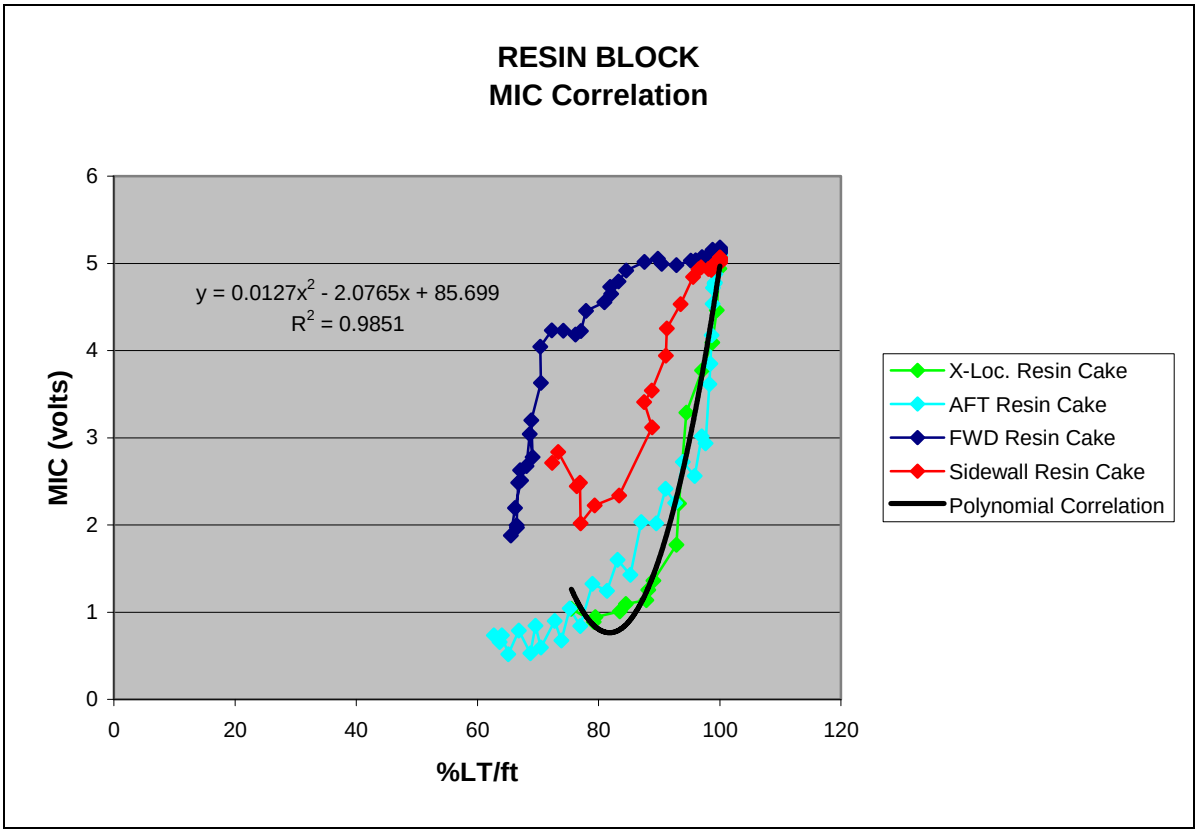

Figure 17. Correlation of MIC to Smokemeter for Aft and X Location

The forward starboard corner and sidewall starboard perimeter locations were not accurately modeled by the previous polynomial and, therefore, were given other suitable polynomial equations to produce MIC data. Figures 18 and 19 show the MIC correlation plots for the resin block at the forward starboard corner location and sidewall starboard location, respectively. Each MIC correlation polynomial equation was dependent on the percent light transmission per foot data from the converted computational data to produce an accurate correlated MIC voltage value for each time step. Figure 18 displays the curve generated from averaging the MIC and smokemeter data of three different forward starboard corner resin block experimental tests. The same averaging technique was also used to generate the plot of MIC versus percent light transmission per foot for the sidewall location in figure 19.

The correlation discovered between the MIC voltage difference and the smokemeters' percent light transmission per foot was crucial for comparison of computational and experimental results. The four polynomial equations listed below were used in conjunction with CFD percent light transmission data to determine CFD MIC voltage data. The dependent variable "x" in all equations is the converted percent light transmission data obtained from the CFD simulations.

- X Location Volts = $0.0127*(x^2) - 2.0765*(x) + 85.699$
- Aft Location Volts = $0.0127*(x^2) - 2.0765*(x) + 85.699$
- Fwd Location Volts = $0.0047*(x^2) - 0.8738*(x) - 35.163$
- Sidewall Location Volts = $0.0028*(x^2) - 0.3833*(x) + 15.372$

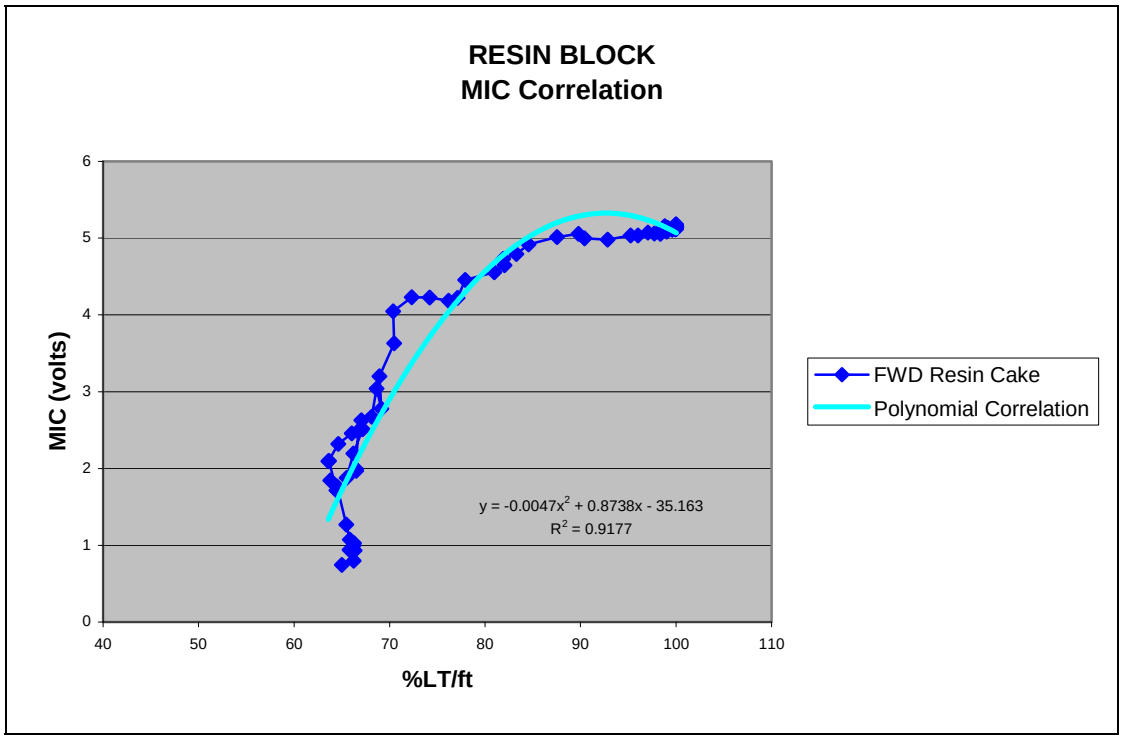

Figure 18. Correlation of MIC to Smokemeter for Forward Location

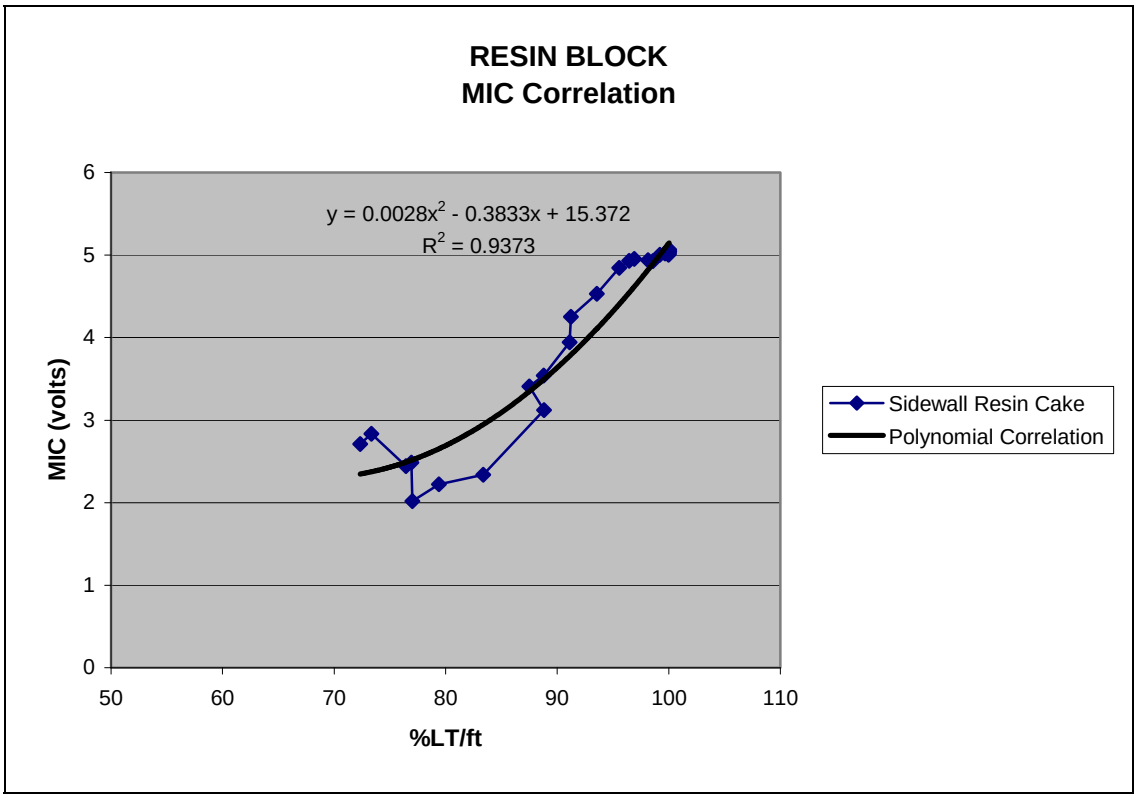

Figure 19. Correlation of MIC to Smokemeter for Sidewall Location

5. RESULTS AND DISCUSSION.

5.1 DATA ANALYZING METHOD.

To ensure accurate data collection by the multisensor detector from all fire and nuisance sources, all sources were tested at least four times each at the same location in the cargo compartment. Data was then analyzed for each individual test yielding four temporal plots each of percent light transmission per foot, CO and CO_2 gas concentrations, temperature rise, and MIC voltage for all fire and nuisance sources. The four plots from each sensor were then superimposed onto one graph that also contained an average plot to determine if repeatability with a variation of less than 5% of the average was attained. Once attained, the next step was to take the average of each individual category to produce an overall average temporal variation for percent light transmission per foot, CO and CO_2 gas concentrations, temperature rise, and MIC voltage difference for that specific source per time step, every 2 seconds. For each categories overall average, the average rate of rise was calculated by taking the difference of two consecutive data points and dividing it by the time step of 2 seconds. This same process was performed for all fire and nuisance sources, yielding an overall average for each sensor output. All average values were combined to formulate a matrix of ten parameters that aided in the development of a multisensor algorithm.

5.2 EXPERIMENTAL FIRE TESTING.

5.2.1 Denatured Alcohol.

The pool of 40-mL denatured alcohol was the first fire source to be experimented with and analyzed. The analysis began with the fire source at the x location. The results for each respective sensor are shown in the following figures along with a detailed description of the important intervals to note on each plot. Figure 20 is a plot of the average percent light transmission from four fire tests measured by the recessed pan smokemeter apparatus.

Note that for denatured alcohol, obscuration of the laser did not occur until about 90 seconds. At this point, the percent light transmission gradually decreased to its absolute minimum of 86%LT/ft.

Figure 21 shows the average gas concentration rise levels produced by the flaming pool of denatured alcohol. The efficient combustion of denatured alcohol produced very little CO, but the CO_2 rose to a maximum of about 1800 ppm. Ordinary background levels of CO_2 were approximately 350 ppm; however, since background levels were subtracted from the acquired data, the values began at 0 ppm.

Figure 22 is a plot of the temperature rise associated with the denatured alcohol for not only the recessed pan thermocouple, but also for each thermocouple around the perimeter of the recessed region.

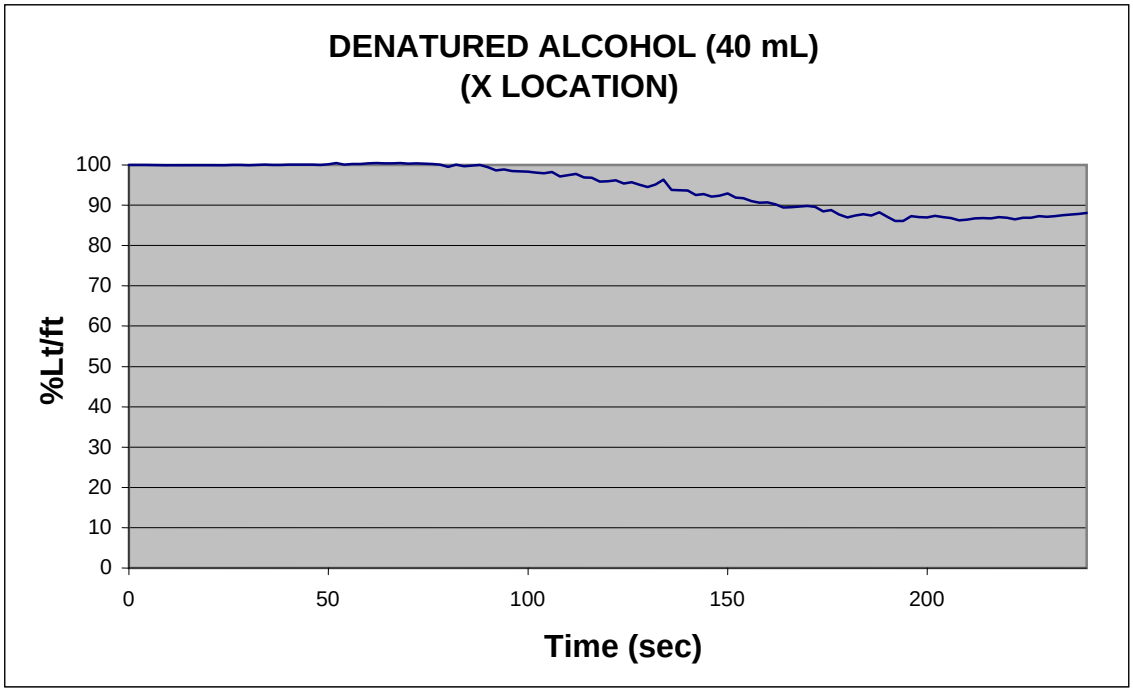

Figure 20. Denatured Alcohol Average Percent Light Transmission per Foot at X Location

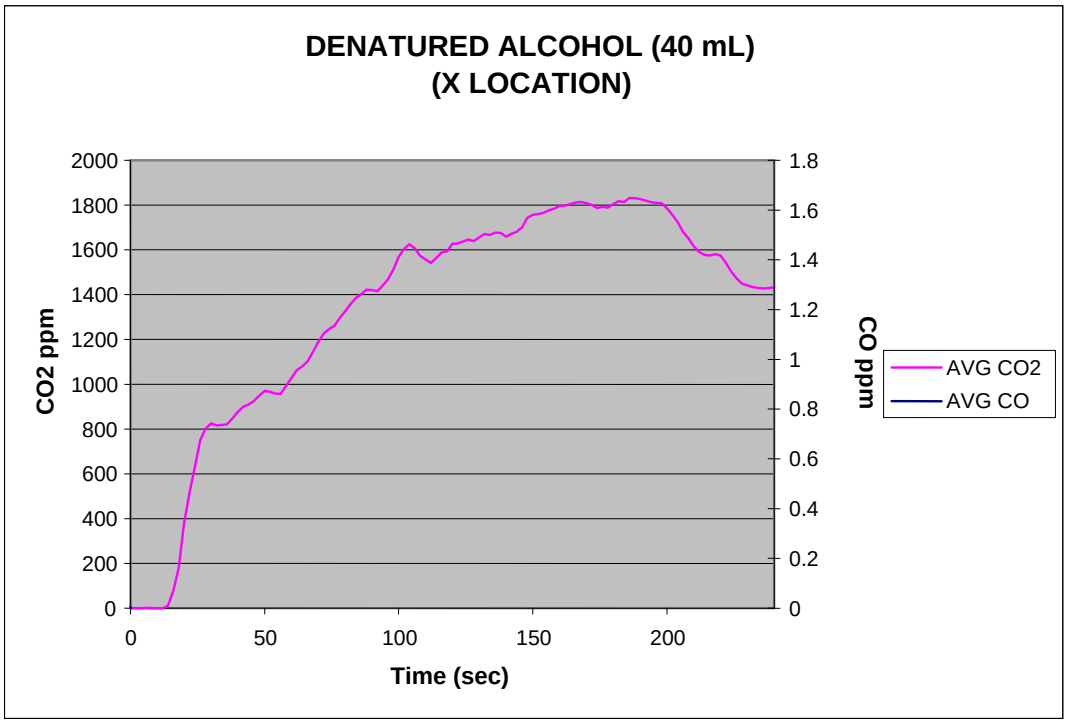

Figure 21. Denatured Alcohol Average CO and CO_2 Gas Concentrations at X Location

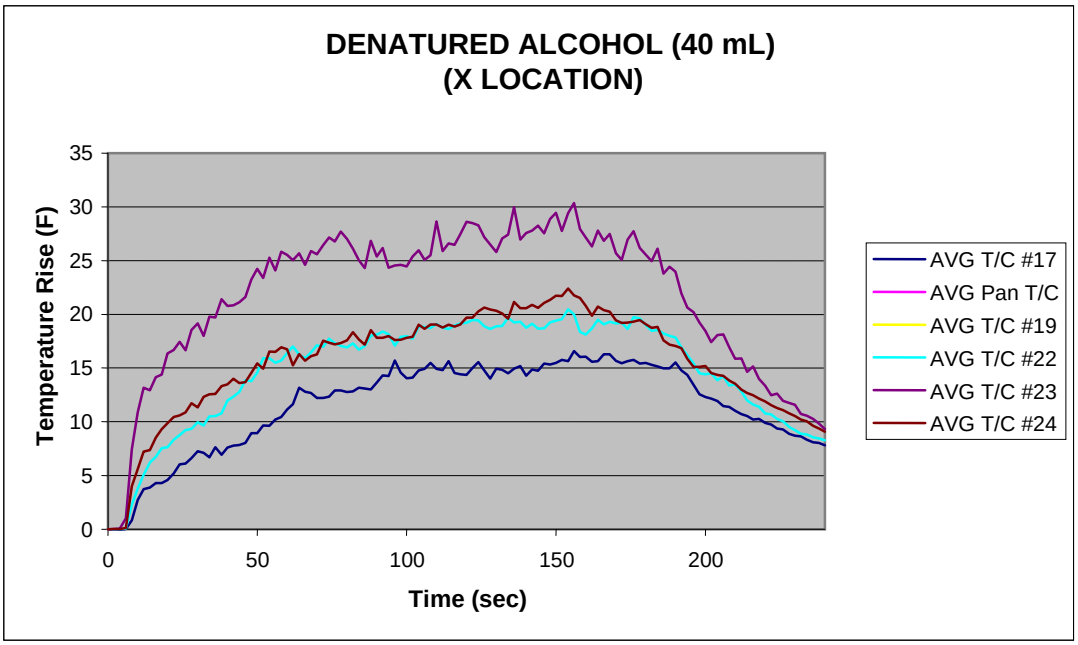

Figure 22. Denatured Alcohol Average Temperature Rise at X Location

Thermocouple response occurred within the first 5 seconds of ignition of the denatured alcohol due to the flaming nature of the fire source. The denatured alcohol produced a rapid increase in temperature for thermocouple 24, located directly above the fire source. For all other thermocouples, there was a slightly more gradual increase in temperature rise. As expected, thermocouples 22, 23, and 24 all have greater rate of rise of temperature because they were located at a closer distance to the fire source. The pan thermocouple, being the second furthest away from the fire source, yielded a relatively slow increase in temperature with an absolute maximum temperature increase of 13 degrees.

The MIC voltage for the denatured alcohol fire is plotted in figure 23. Although ionization detectors are generally more sensitive to flaming fires than smoldering combustion, this fire did not cause the MIC to cross the alarm threshold of 4.1 volts. The denatured alcohol fire did not generate any response at all by the MIC until approximately 180 seconds into the test.

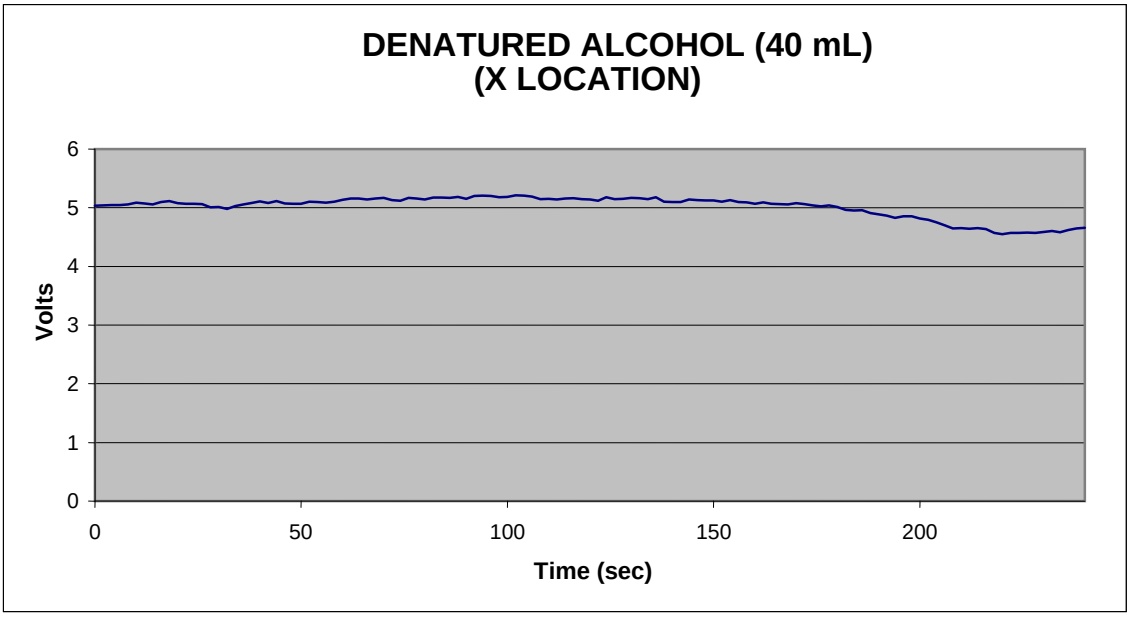

Figure 23. Denatured Alcohol Average MIC Voltage at X Location

5.2.2 Polyurethane Foam.

The fire source that was experimented with next was that of polyurethane foam. Polyurethane foam was also considered a flaming fire source and produced a high heat signature, which will be noted in later figures. Figure 24 represents the average percent light transmission, and as shown, the smokemeter was affected by the burning foam block almost immediately. From test ignition, the light transmission decreased steeply to a minimum of 91.5%LT/ft at about 43 seconds. After this point, the smokemeter began to stabilize at approximately 95%LT/ft as the foam block kept burning until it extinguished at 4 minutes.

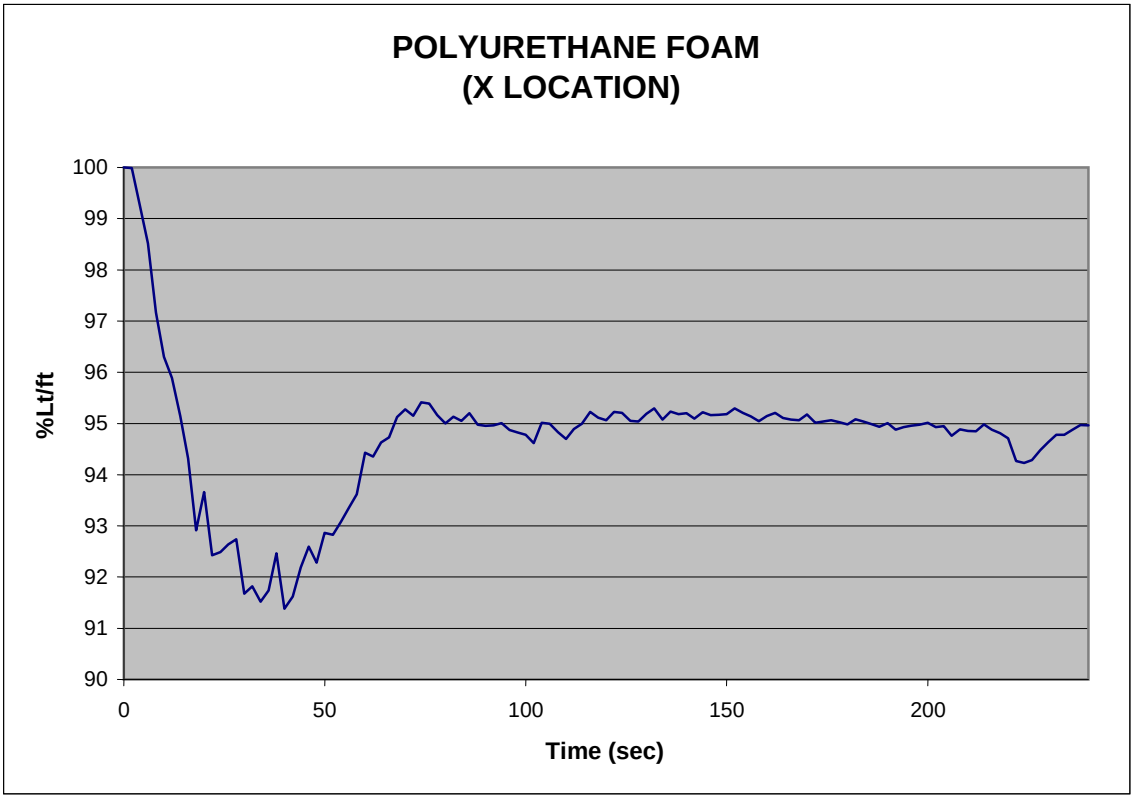

Figure 24. Polyurethane Foam Average Percent Light Transmission per Foot at X Location

Figure 25 is the average gas concentration rise data produced from the polyurethane foam fire source. After about 8 seconds, both the CO and CO_2 levels began to rise simultaneously. The CO level peaked at 15 ppm, whereas the CO_2 level went off scale above 2100 ppm. The CO_2 analyzer had an actual range of 0 to 2500 ppm but was limited to about 2100 ppm for these tests due to subtracting out the initial ambient CO_2 level of approximately 400 ppm. After the CO reached its maximum of 15 ppm at 45 seconds, it underwent a rapid decrease to its minimum value of 7 ppm at about 130 seconds before rising again.

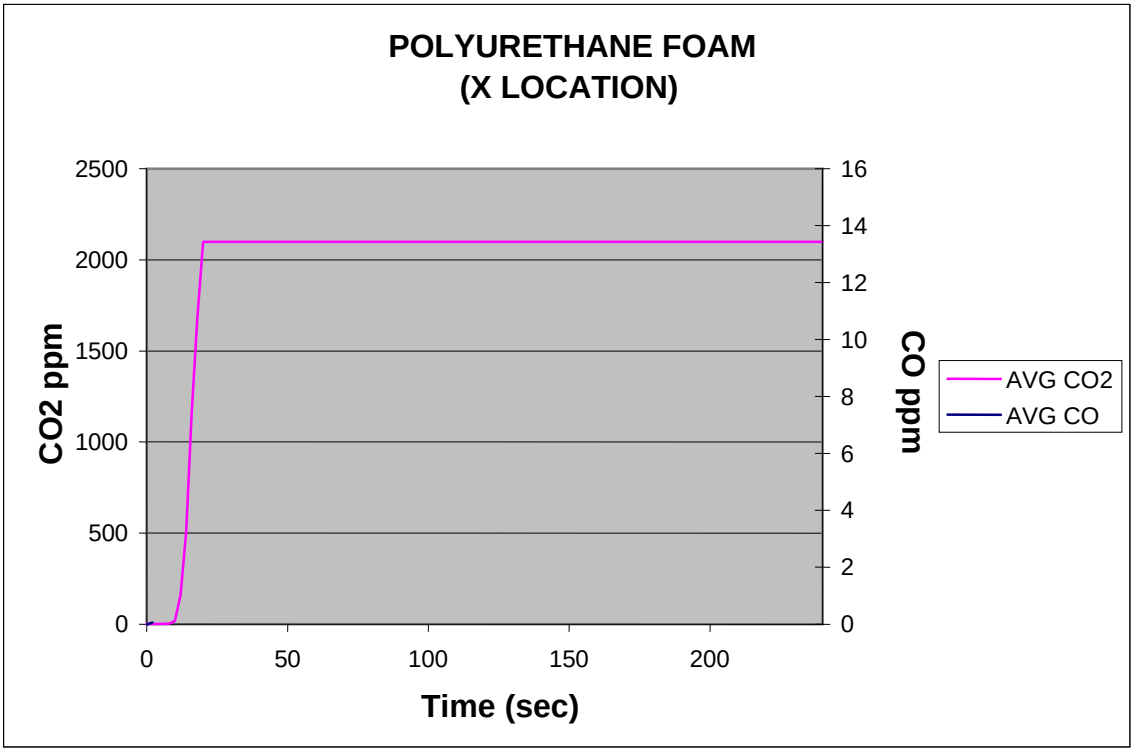

Figure 25. Polyurethane Foam Average CO and CO_2 Gas Concentrations at X Location

Figure 26 shows the temperature rise associated with the flaming polyurethane foam. Trend lines among all thermocouples followed the same behavior, although the magnitudes differed due to each thermocouples distance away from the fire source. It was important to note the time when all thermocouples began to stabilize and decreased from their maximum. From figure 26, at 25 seconds, all thermocouple temperature rise readings began to stabilize at their respective magnitudes. After approximately 75 seconds, the data showed a gradual decrease in temperature rise, which was attributed to the slower burning process of the partially charred foam block.

Figure 27 reveals the typical behavior of the MIC, starting out at the reference voltage of 5.1 volts, and decreasing past its alarm threshold point at approximately 25 seconds into the fire test. The foam block, due to its flaming nature, produced particles smaller than 1 micron, which caused an immediate response in the MIC. The larger scale solid physical composition of the polyurethane foam block produced a greater response from the MIC than the smaller scale liquid alcohol test, which did not even trigger the MIC into alarm mode. Although both sources were flaming sources that should be detected by the MIC, the difference in the heat release rates of the two fire types affected both the volume and buoyancy of the products of combustion.

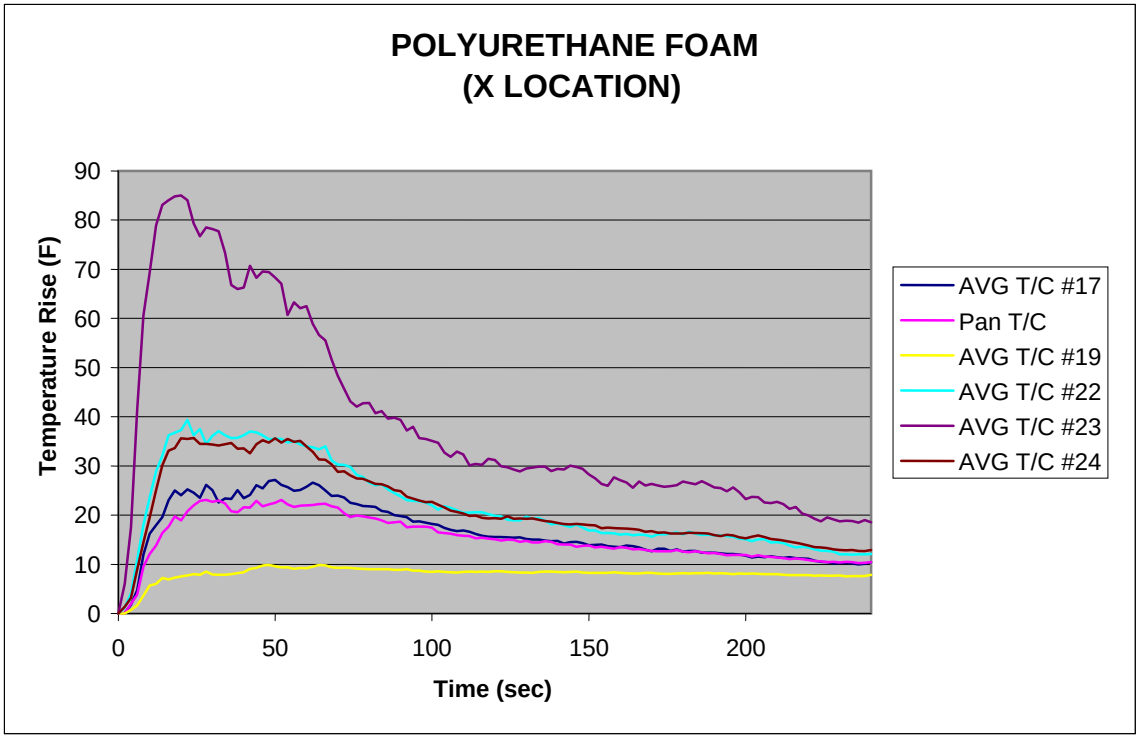

Figure 26. Polyurethane Foam Average Temperature Rise at X Location

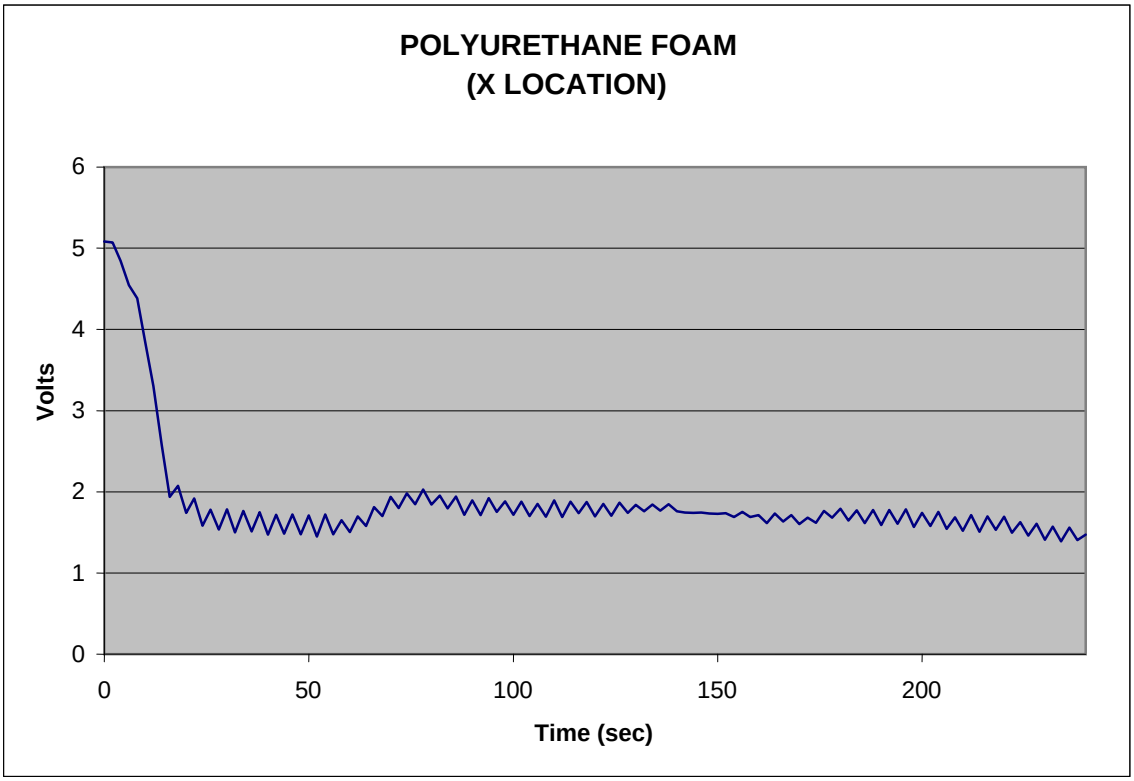

Figure 27. Polyurethane Foam Average MIC Voltage at X Location

5.2.3 Alcohol-Soaked Rags.

The next fire source that was tested was rags soaked with 10 mL of denatured alcohol. As shown in figure 28, the smokemeter responded fairly quickly, but the fire generated relatively little smoke with minimum level of 94.5%LT/ft at about 50 seconds into the test. The percent light transmission thereafter began to increase until almost returning to 100%. Looking at figure 29, the gas concentrations from the alcohol-soaked rag produced more CO than denatured alcohol by itself, as shown in figure 21. The CO_2 levels rapidly increase to near the highest range of the gas analyzer within 90 seconds and then plateau. Figure 21, with only denatured alcohol, showed a more gradual increase and slightly smaller magnitude for the CO_2 compared to the alcohol-soaked rags.

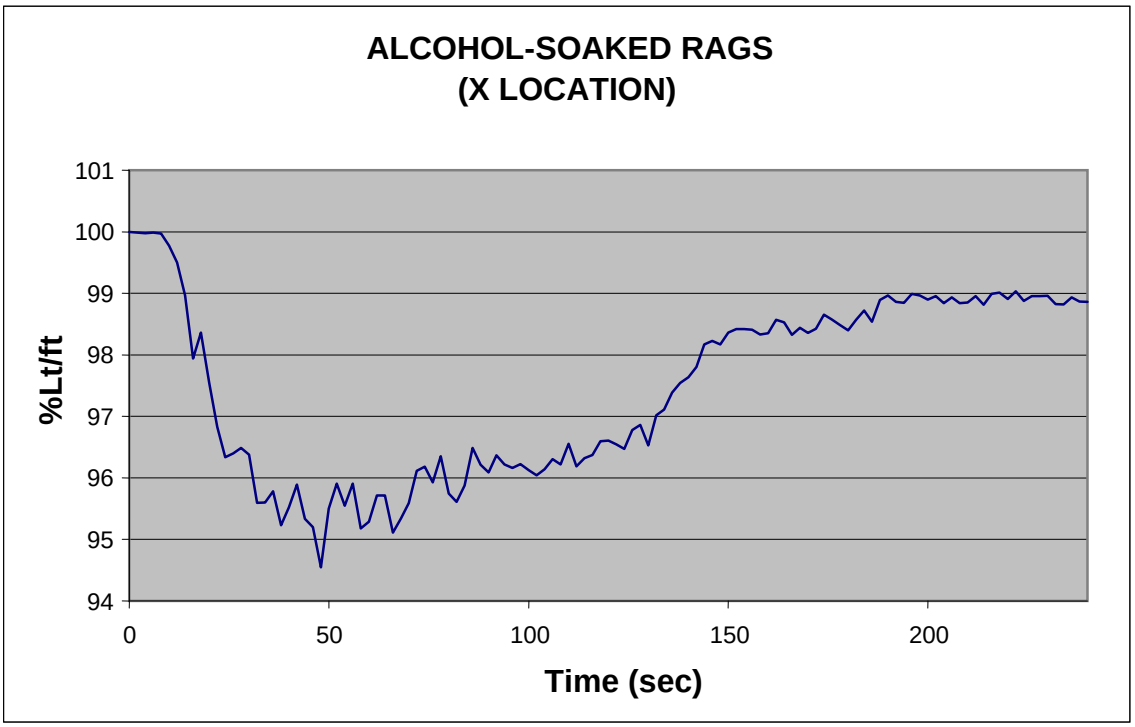

Figure 28. Alcohol-Soaked Rags Average Percent Light Transmission per Foot at X Location

The temperature rise level in figure 30 was similar to previous temperature profile trends with the exception of the difference in magnitudes. The temperature rise increased to its maximum at about 1 minute for all thermocouples and then began to taper off and stabilize between 10 and 20 degrees for all but one thermocouple. The MIC data in figure 31 showed the first steady decrease at about 15 seconds into the test. The alarm threshold point was crossed just after 25 seconds. As shown in figures 27 and 31, the MIC output oscillated around a value of just under 2 volts shortly after the detector went into alarm. Once the detector is in alarm, the MIC voltage output is no longer related to the quantity of particles the detector senses (as discussed in private conversation with Kidde engineers).

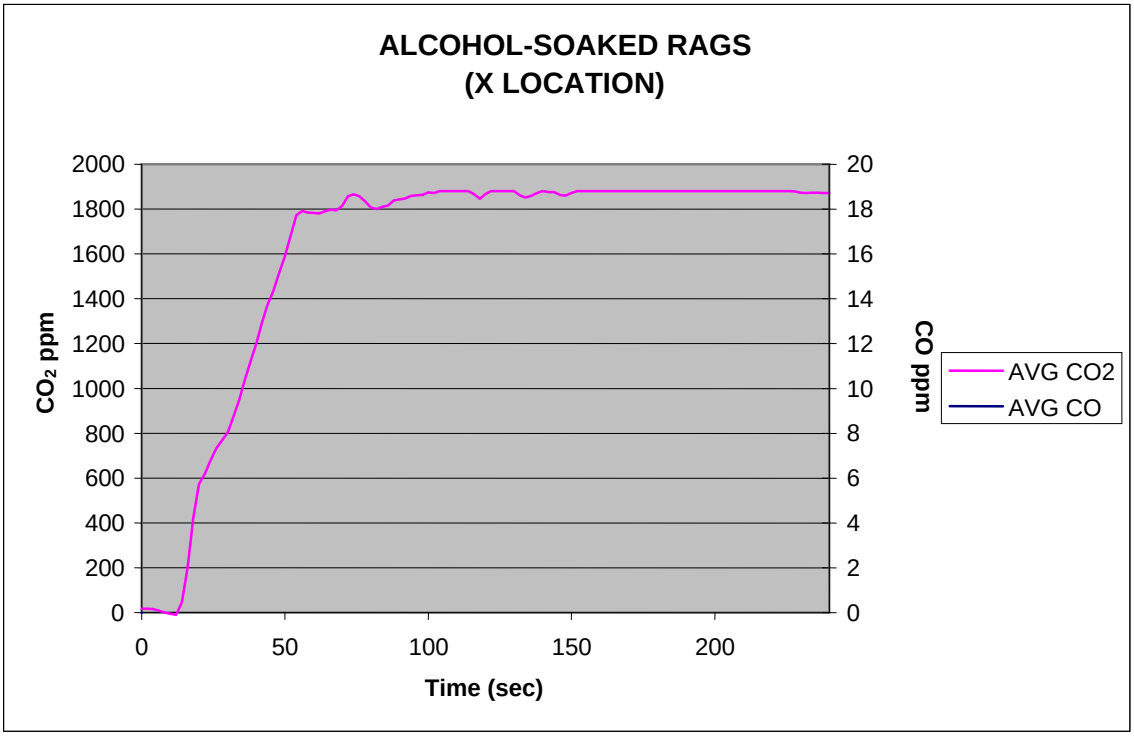

Figure 29. Alcohol-Soaked Rags Average CO and CO_2 Gas Concentrations at X Location

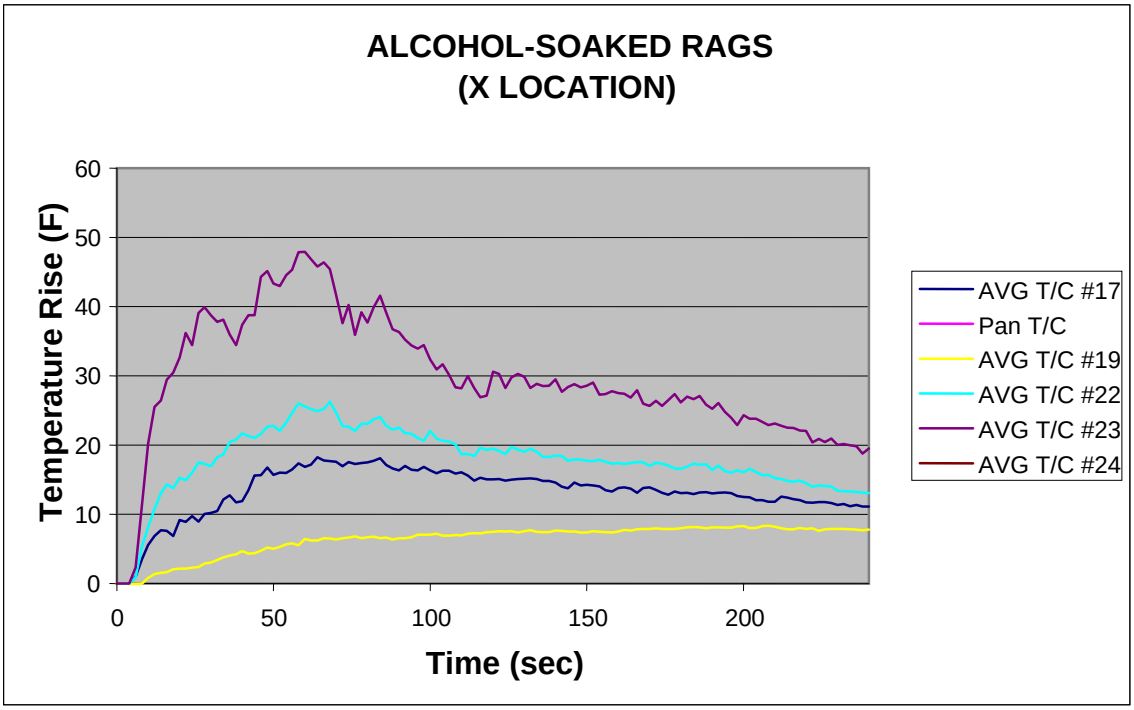

Figure 30. Alcohol-Soaked Rags Average Temperature Rise at X Location

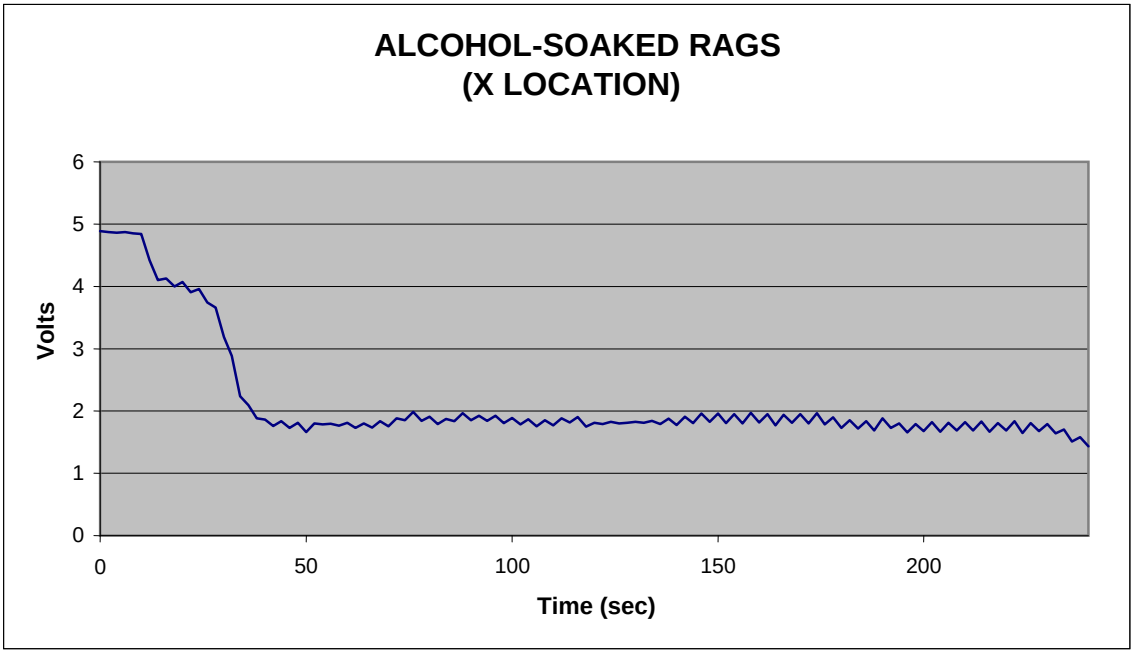

Figure 31. Alcohol-Soaked Rags Average MIC Voltage at X Location

5.2.4 Shredded Newspaper.

The shredded newspaper tests produced a flaming fire with very dense smoke. Figure 32 shows the smokemeter data that fell below the alarm threshold level after about 30 seconds and reached a minimum of close to 50%LT after 100 seconds. Figure 33 shows the average CO and CO_2 levels and the rapid rise of both gases. The CO_2 levels went off scale after approximately 40 seconds.

The temperature rise profiles in figure 34 demonstrated the relatively high heat release rate produced by a pan of shredded newspaper. At approximately 10 seconds, the thermocouples indicated a change in temperature within the compartment. At this point, the newspaper was smoldering with the transition to flaming combustion occurring between 15 and 20 seconds, producing the rapid temperature rise shown in figure 34. Further analysis of figure 34 revealed a 35 degree maximum temperature rise from the recessed pan thermocouple. This was the highest temperature rise for the recessed pan thermocouple for all fire tests. Figure 35 further emphasized the transition process of the newspaper from smoldering to flaming after 15 seconds by the rapid decrease in the MIC between the 15- and 20-second time frame. The MIC dropped past the alarm threshold point almost immediately after the flame was initiated, just before the 20-second mark.

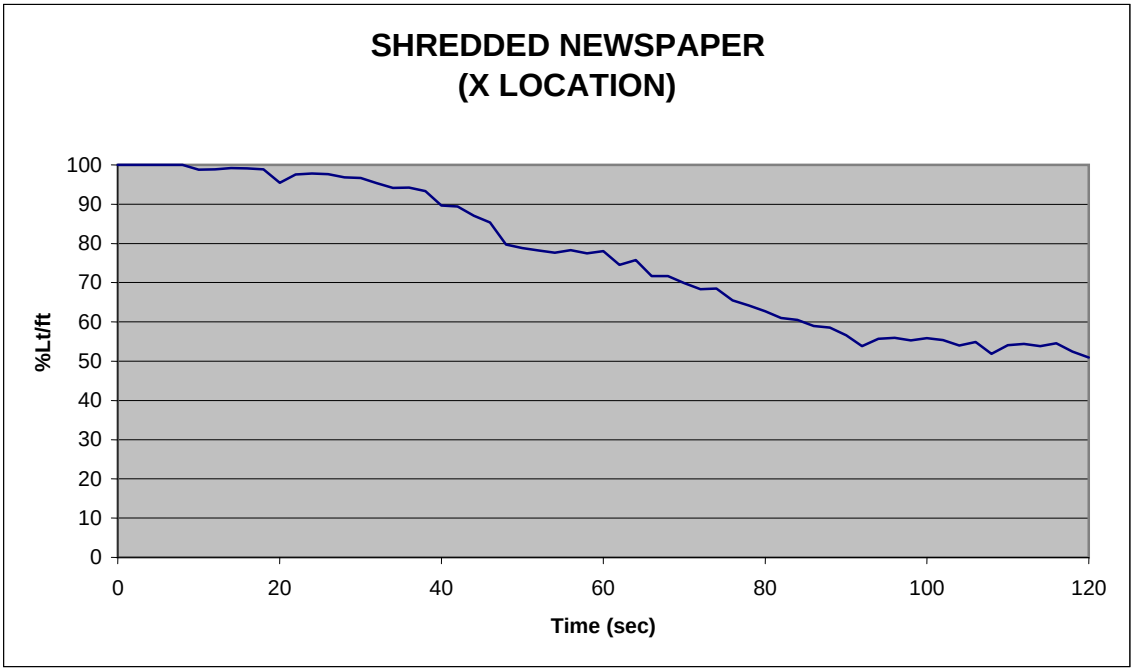

Figure 32. Shredded Newspaper Average Percent Light Transmission per Foot

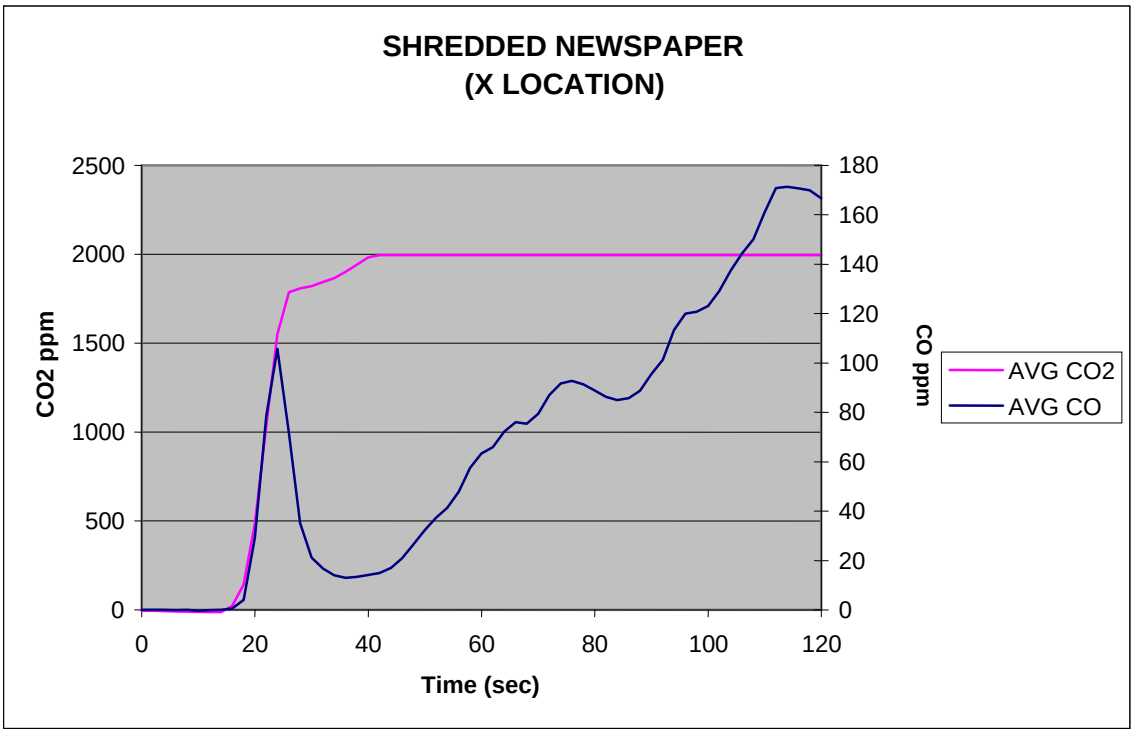

Figure 33. Shredded Newspaper Average CO and CO_2 Gas Concentrations at X Location

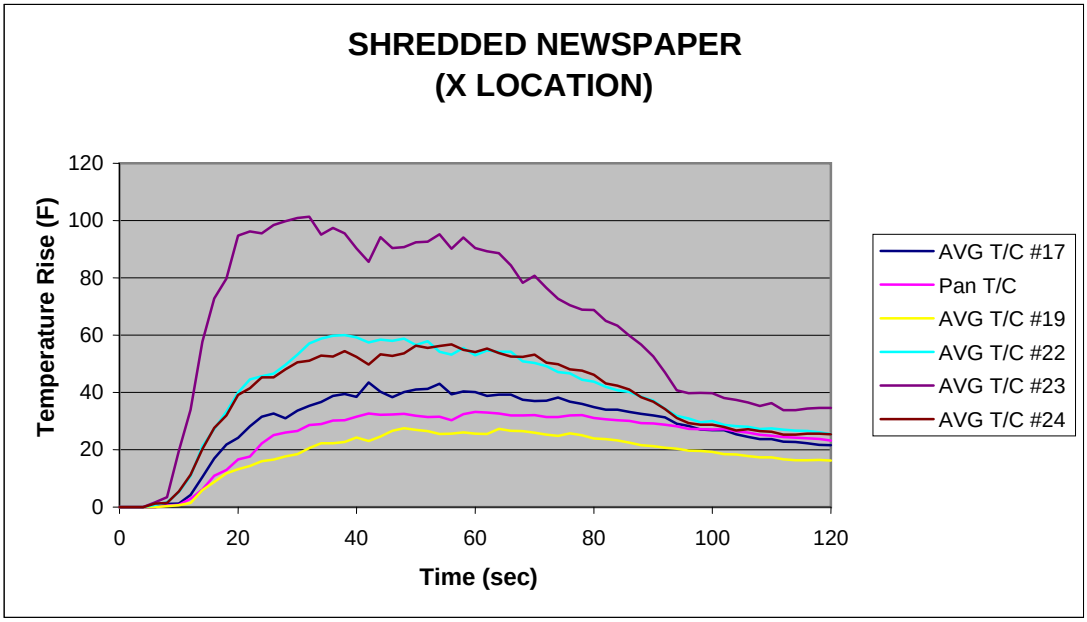

Figure 34. Shredded Newspaper Average Temperature Rise at X Location

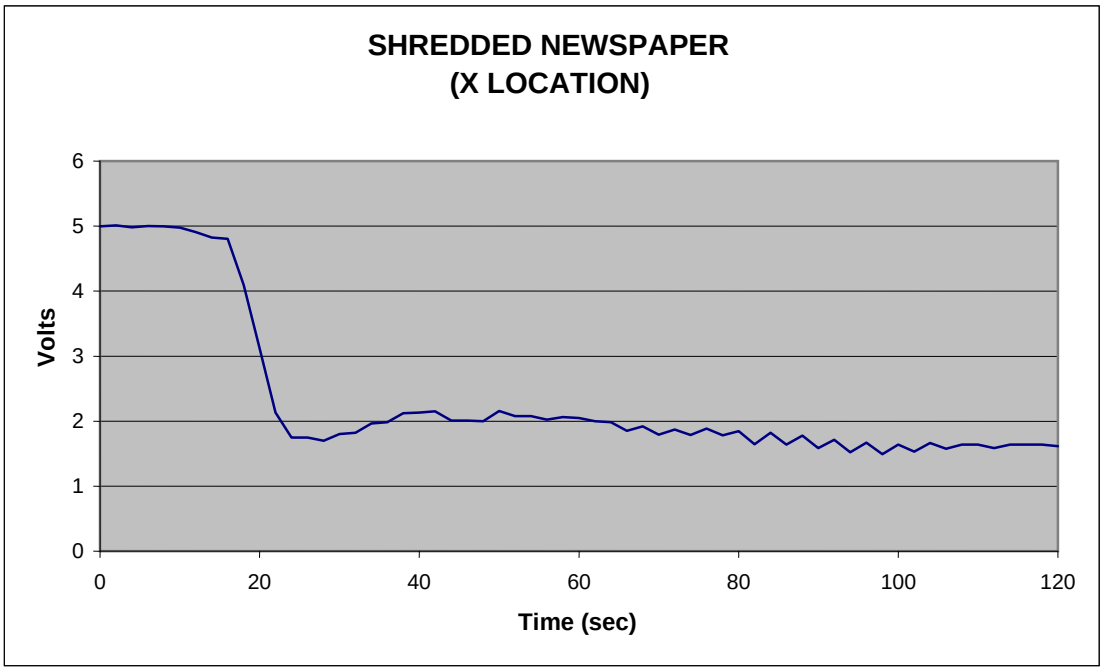

Figure 35. Shredded Newspaper Average MIC Voltage at X Location

5.2.5 Suitcase.

Figure 36 shows the gradual decrease in percent light transmission for the smoldering suitcase tests. The suitcase test lasted for 6 minutes and was the longest lasting smoldering fire source. Compared to the other fire sources, the suitcase produced much higher levels of CO, with a peak

slightly above 350 ppm. This was attributed to the less efficient combustion associated with smoldering fires. After 5 minutes, the suitcase usually transitioned from smoldering to flaming. The transition was evident in figure 37 at approximately 300 seconds with a significant change in the ratio of CO_2 to CO.

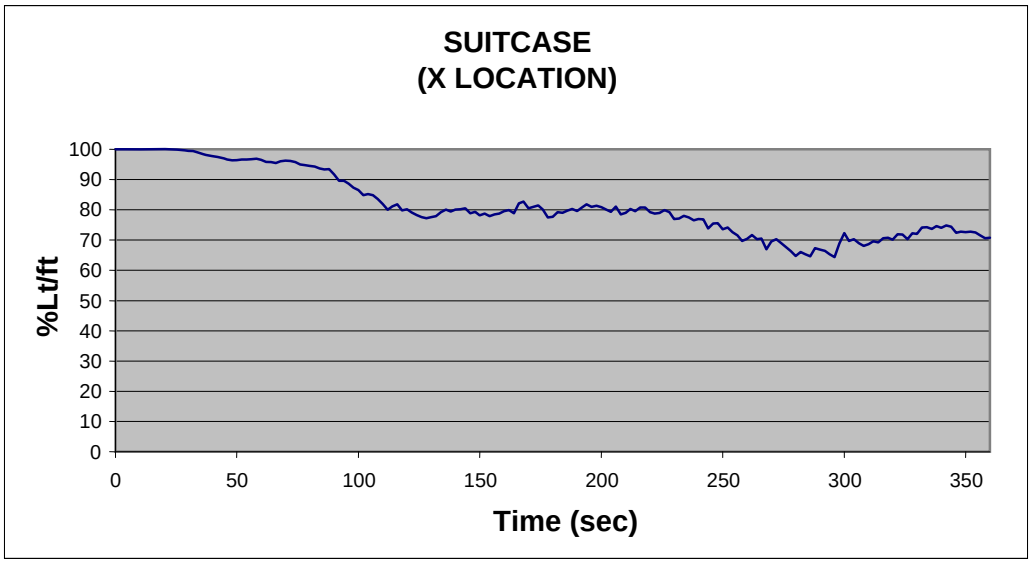

Figure 36. Suitcase Average Percent Light Transmission per Foot at X Location

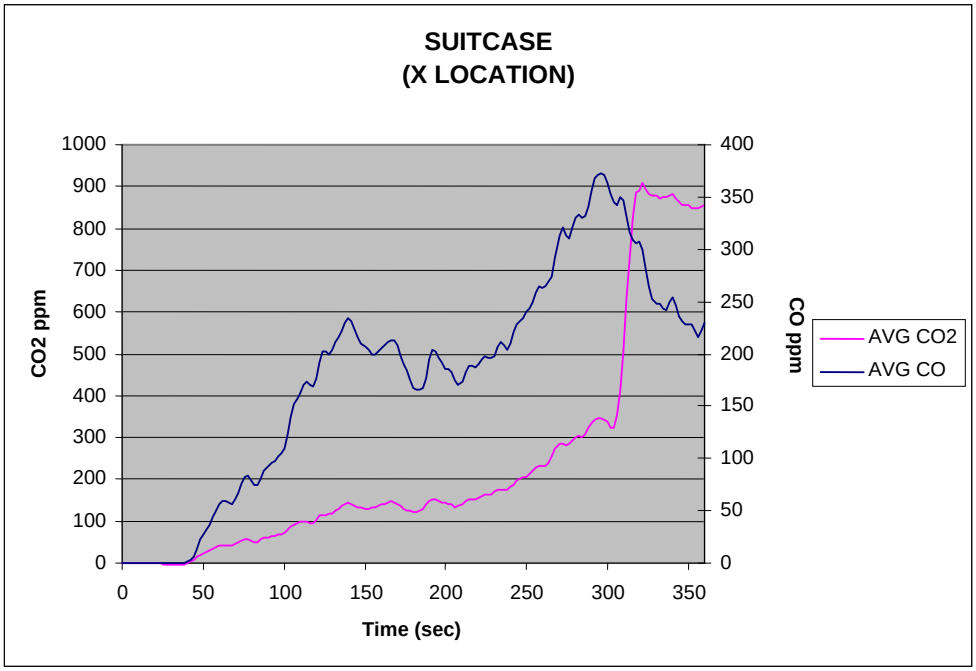

Figure 37. Suitcase Average CO and CO_2 Gas Concentrations at X Location

Figure 38 shows the rapid increase in temperature rise at the 5-minute mark, where the fire source transitioned from smoldering to flaming. The suitcase produced less than a 5-degree temperature rise for the first 5 minutes of smoldering. The pan thermocouple increased linearly from about 2 degrees to its maximum of 8 degrees during the 1-minute flaming period. The MIC voltage did not drop below its threshold point of 4.1 volts until after 2 minutes into the test. Figure 39 shows that the MIC demonstrated a considerably slower response for a smoldering fire source than that of the previous flaming fire sources, with the exception of the denatured alcohol tests.

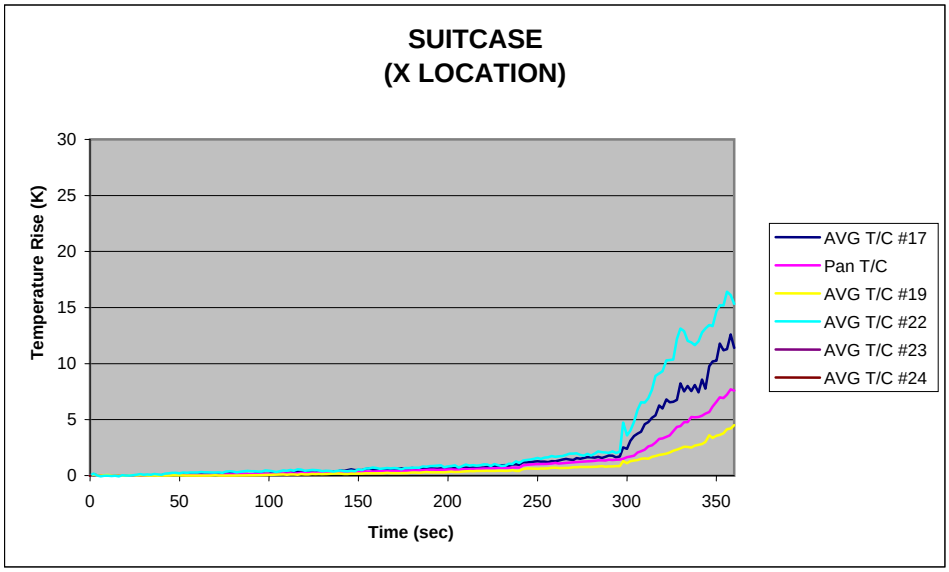

Figure 38. Suitcase Average Temperature Rise at X Location

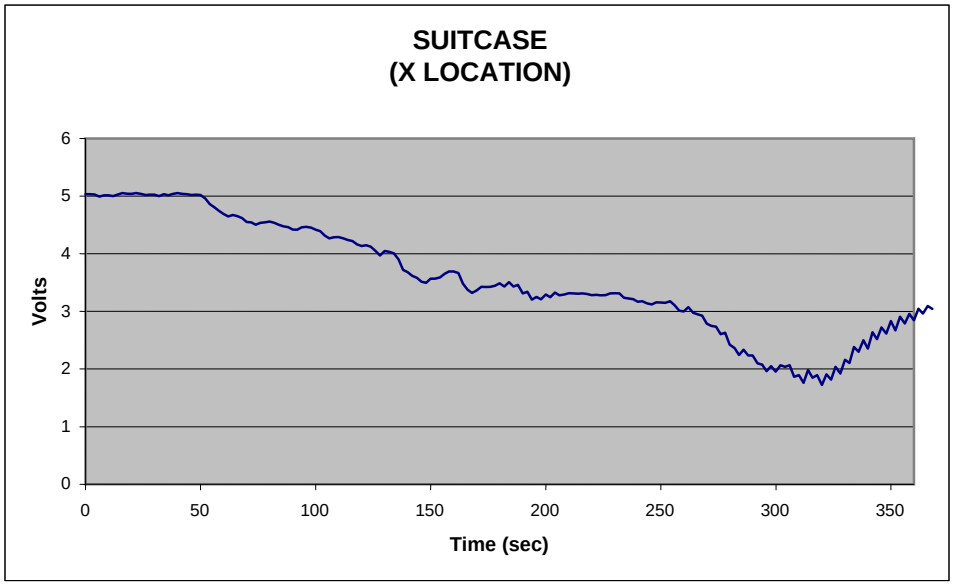

Figure 39. Suitcase Average MIC Voltage at X Location

5.3 PERIMETER EXPERIMENTAL FIRE TESTING.

Multiple detectors are typically installed throughout the ceiling of cargo compartments to ensure rapid detection regardless of the fire location. The previous experiments at the x location spot provided useful data for the initial algorithm development. However, perimeter testing was necessary to determine a functional range of the multisensor detector. Perimeter testing data was also used to produce alarm algorithm threshold levels for fires not in the immediate vicinity of the detector. Polyurethane foam, shredded newspaper, and alcohol-soaked rags were the three fire sources chosen for perimeter testing at the two locations furthest from the multisensor detector. Those locations were the forward starboard corner and the aft starboard corner. The three sources were selected because they were highly repeatable, readily available, and produced significant response in sensor levels. The burning suitcases were not very repeatable, and the smaller scale nature of the denatured alcohol did not produce a significant fire signature. The coordinates and physical locations for all perimeter locations were previously shown in figure 12.

5.3.1 Smokemeter.

Figures 40 and 41 show the smokemeter response from all three fire sources at both the forward starboard corner and aft starboard corner, respectively. For the forward starboard location, the polyurethane foam provided the fastest response from the smokemeter at about 20 seconds. This was followed by the alcohol-soaked rags at 25 seconds, and then close after by the shredded newspaper at 28 seconds. It was interesting to note that the opposite sequence was followed at the aft location. In the forward starboard location, the foam produced a faster response, but the shredded newspaper surpassed the foam in minimum percent light transmission after 75 seconds. The alcohol-soaked rags produced a slight decrease in the smokemeter, but was not significant enough to exceed the photoelectric alarm threshold point of 96%LT/ft. The aft starboard location was closer to the recessed pan, and the smokemeter was affected more by the alcohol-soaked rags and exceeded the photoelectric alarm threshold point at 50 seconds. Figure 41 showed this behavior along with the predictable further decay of percent light transmission from the shredded newspaper. The reduction in light transmission during the foam fire tests was similar in both locations, with a slightly lower percent light transmission level achieved from the further forward starboard location. Both the foam and newspaper sources show good indication that they would be detectable even at the furthest locations within the cargo compartment from the multisensor detector.

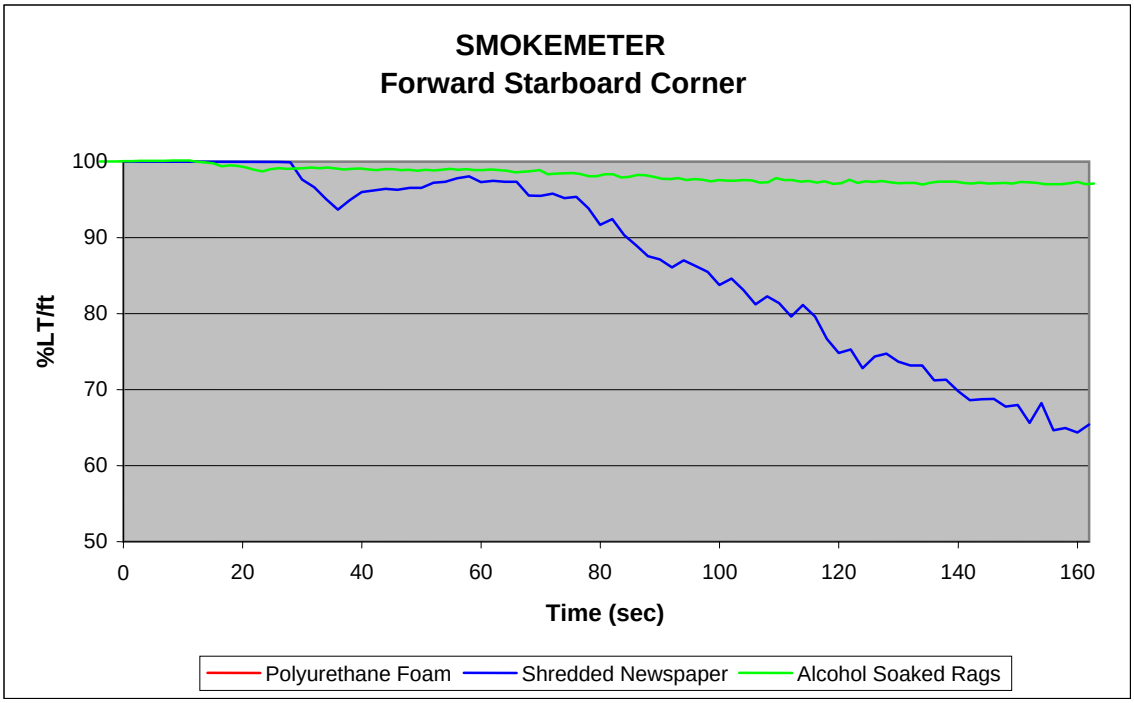

Figure 40. Forward Starboard Corner Percent Light Transmission per Foot Results

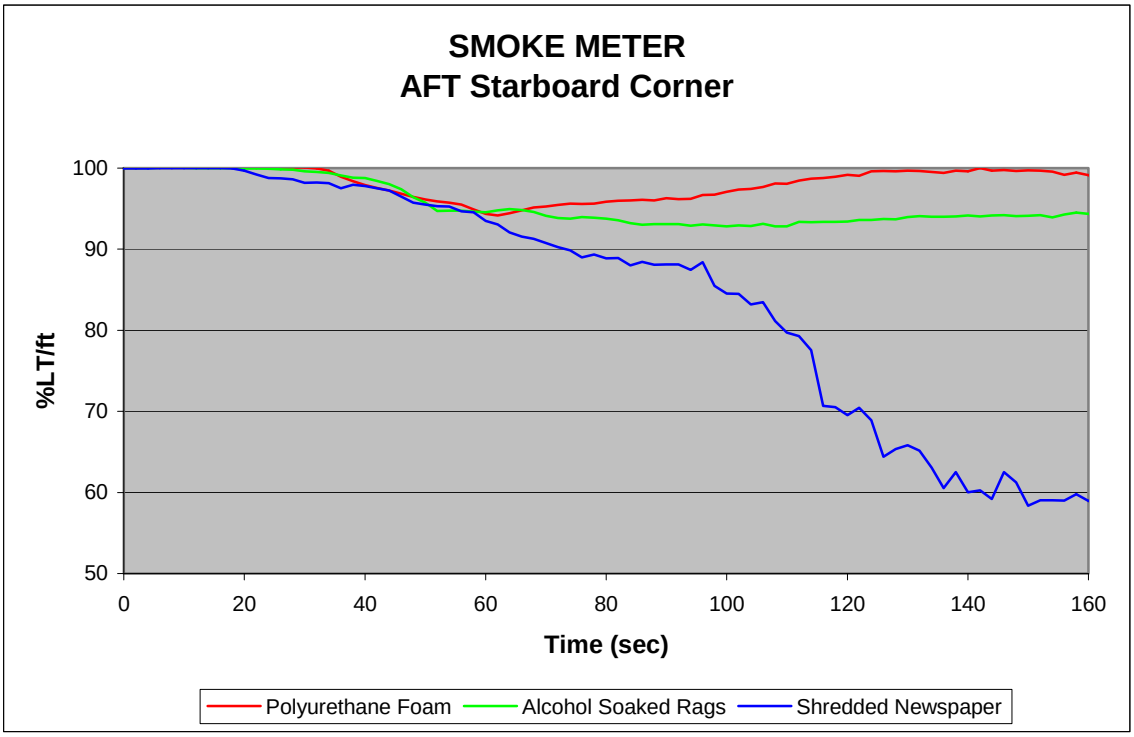

Figure 41. Aft Starboard Corner Percent Light Transmission per Foot Results

5.3.2 Measuring Ionization Chamber.

The MIC data in figures 42 and 43 showed that the polyurethane foam produced the faster response time from the sensor at the forward starboard location, but the slowest response time at the aft starboard location. At the forward location, the foam test triggered the MIC into alarm mode at 22 seconds. MIC response was not obtained until about 33 seconds for the foam test at the aft location. Although at the forward location, the alcohol soaked rags did not produce enough smoke to exceed the photoelectric alarm threshold point, it was able to trigger the MIC into alarm mode at 34 seconds. This was due to the flaming nature of the alcohol-soaked rag that produced particles that were detected by the MIC. The MIC did not exceed the alarm point until 46 seconds for the alcohol-soaked rags at the aft location. The shredded newspaper once again produced the slowest response time for the forward location, producing a rapid decrease in the MIC at a delayed 35 seconds and exceeding the alarm threshold 1 second later. For the aft location, the newspaper produced the fastest response time, followed by the alcohol-soaked rags, and then the foam.

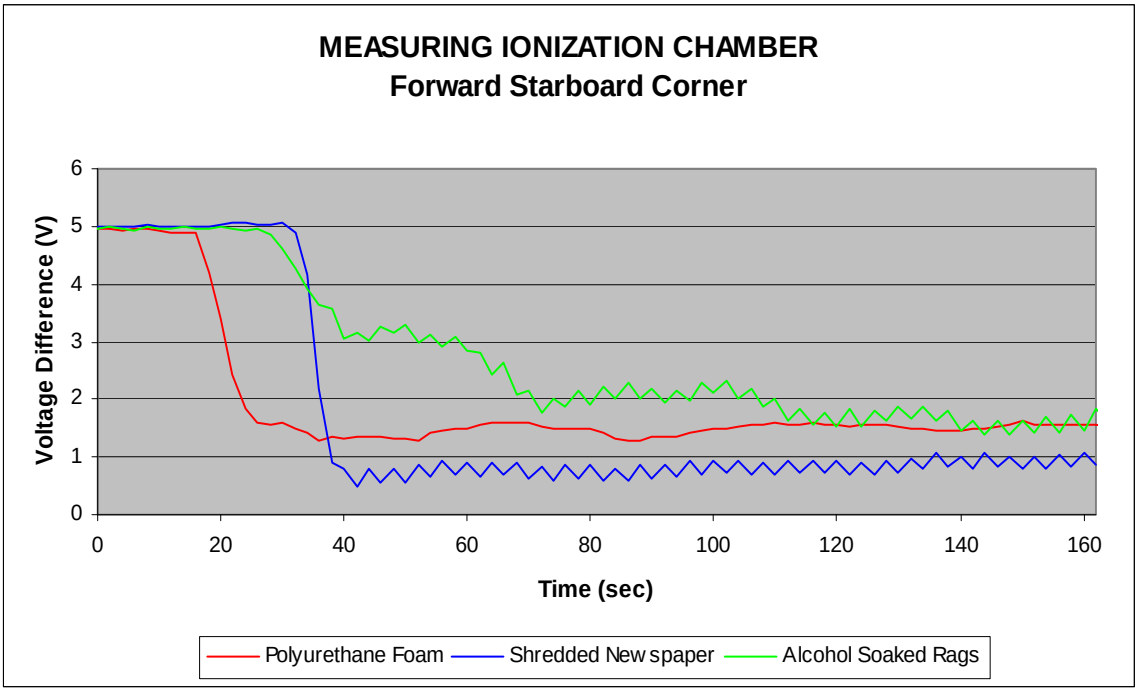

Figure 42. Forward Starboard Corner MIC Voltages

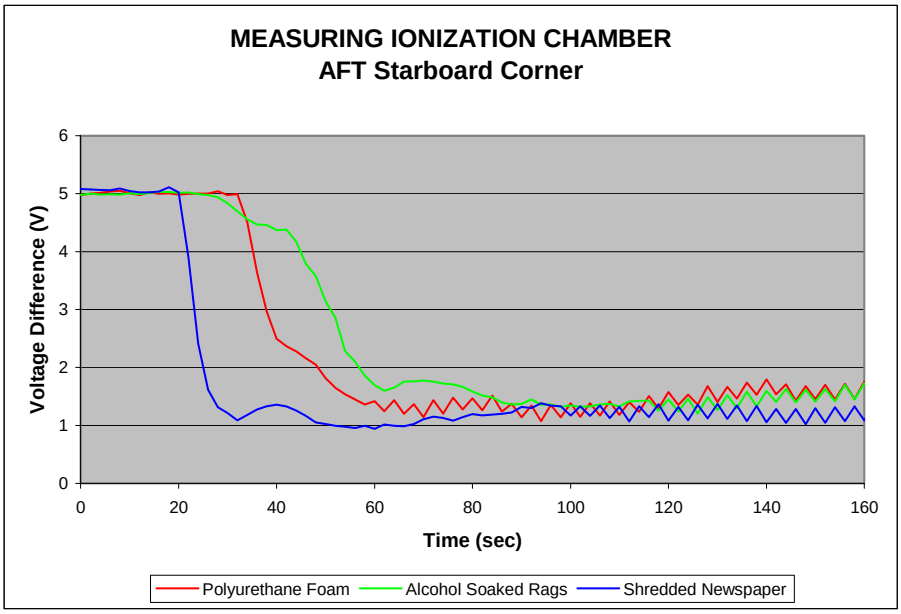

Figure 43. Aft Starboard Corner MIC Voltages

5.3.3 The CO_2 Gas Probe.

The CO_2 gas concentration rise for fires in the forward starboard corner in figure 44 showed the polyurethane foam and shredded newspaper both exceeding the upper limit of the analyzer range and the alcohol-soaked rags reaching about 1700 ppm. Figure 45 shows all three fire sources exceeding the upper limit of the analyzer. The sequential behavior for the gas probe data began with the foam increasing first, and then followed by the rags and newspaper for the forward location. Once again, the opposite sequence was observed for the aft location.

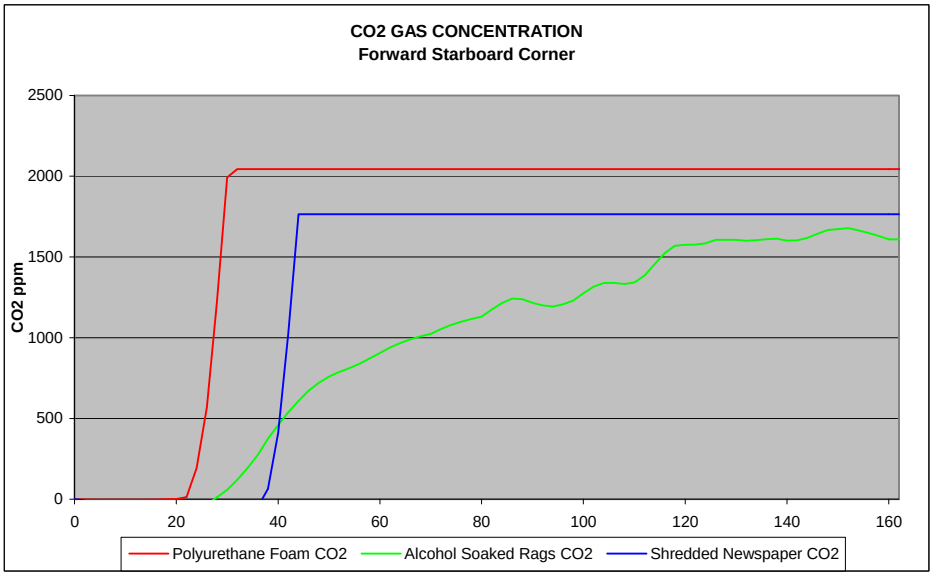

Figure 44. Forward Starboard Corner CO_2 Gas Concentrations

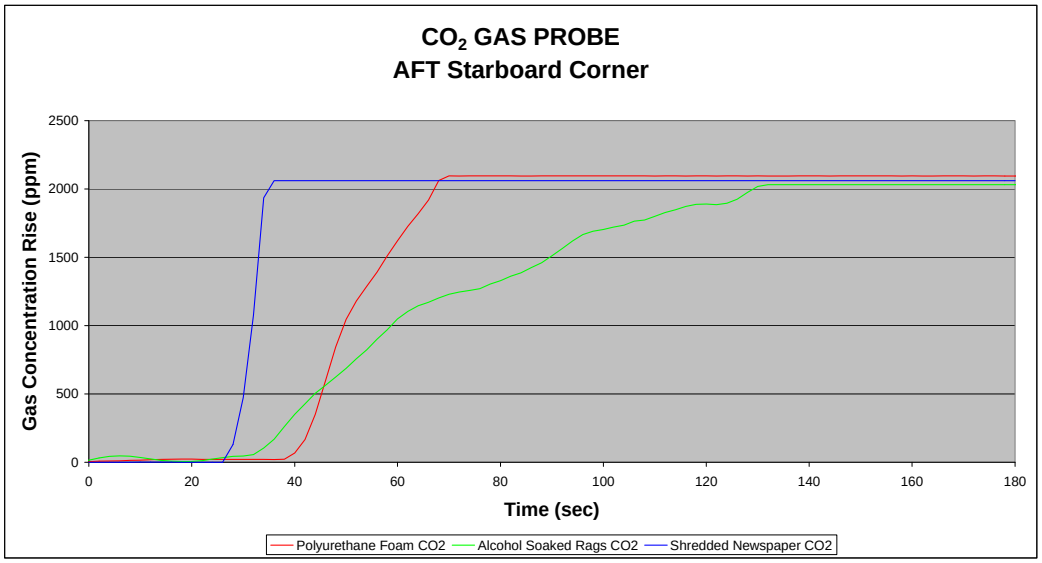

Figure 45. Aft Starboard Corner CO_2 Gas Concentrations

5.3.4 The CO Gas Probe.

Figures 46 and 47 show the significantly higher production rate of CO for the shredded newspaper fires compared to the alcohol-soaked rags and foam fires in the forward and aft starboard locations. However, the relatively low levels of CO produced by the alcohol-soaked rags and foam fires still produced measurable levels at the recessed pan. The response sequence for CO for the three fire types remained the same as the previously measured fire signatures at these locations.

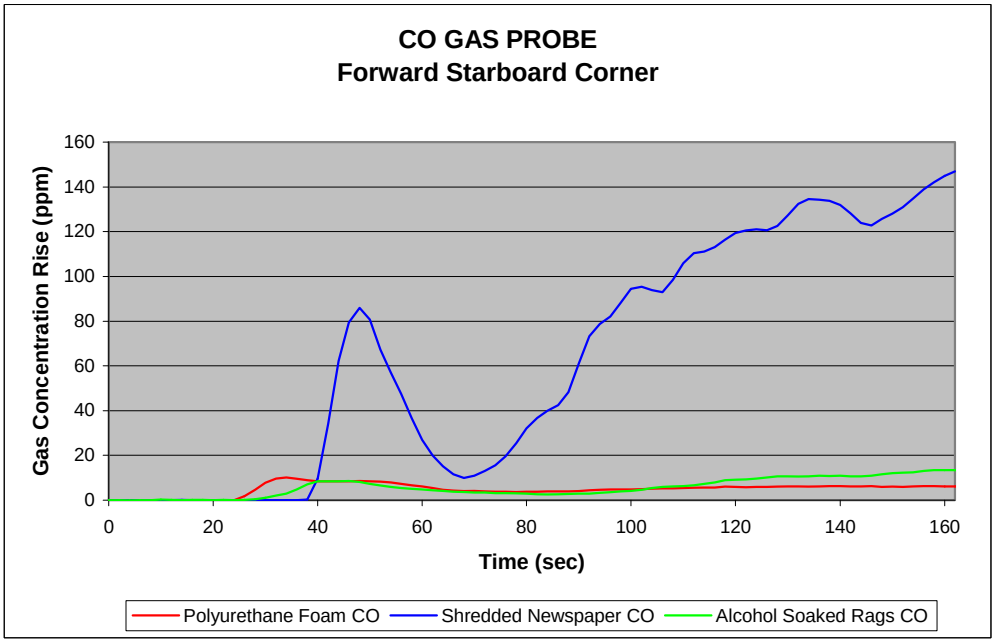

Figure 46. Forward Starboard Corner CO Gas Concentrations

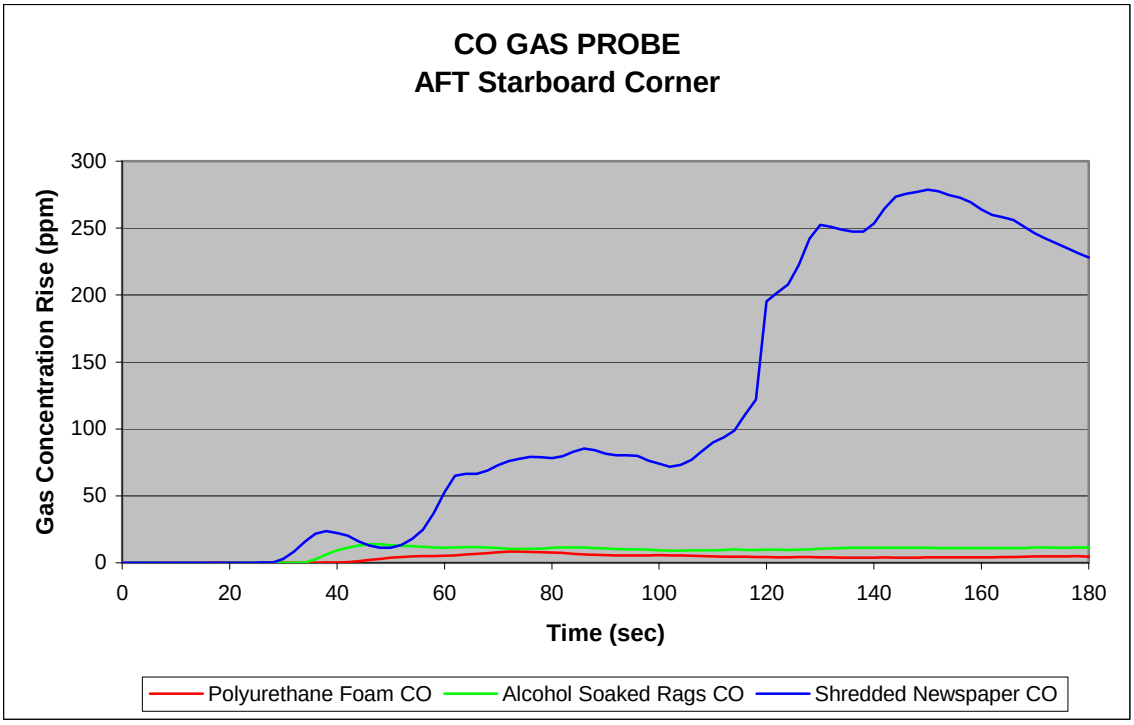

Figure 47. Aft Starboard Corner CO Gas Concentrations

5.3.5 Thermocouple.

Figures 48 and 49 showed temperature rise profiles for all three fire sources for the forward starboard location and aft starboard location, respectively. The shredded newspaper fires produced the greatest temperature rise in both the forward and aft locations. The temperature rise in the aft location was slightly higher than the forward location for all the fire sources due to the closer proximity of the fires to the sensors. These perimeter test were useful in showing that even at the furthest corners of the compartment, the fires produced measurable heat signatures to the thermocouple within the recessed pan.

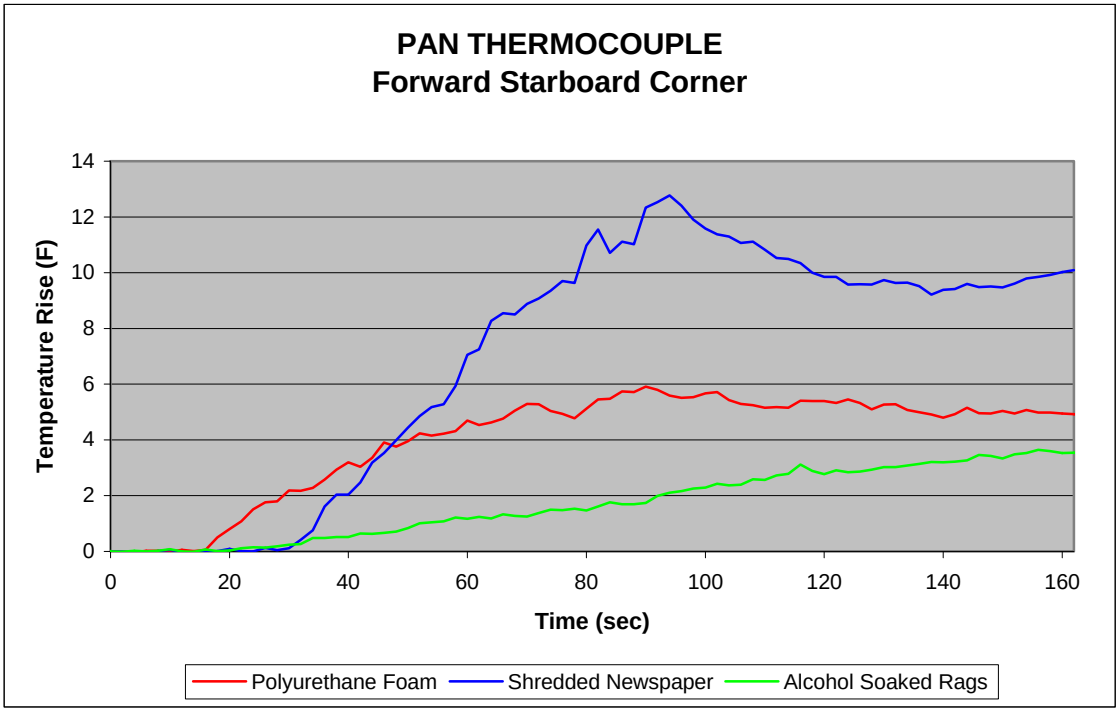

Figure 48. Forward Starboard Corner Temperature Rise Results

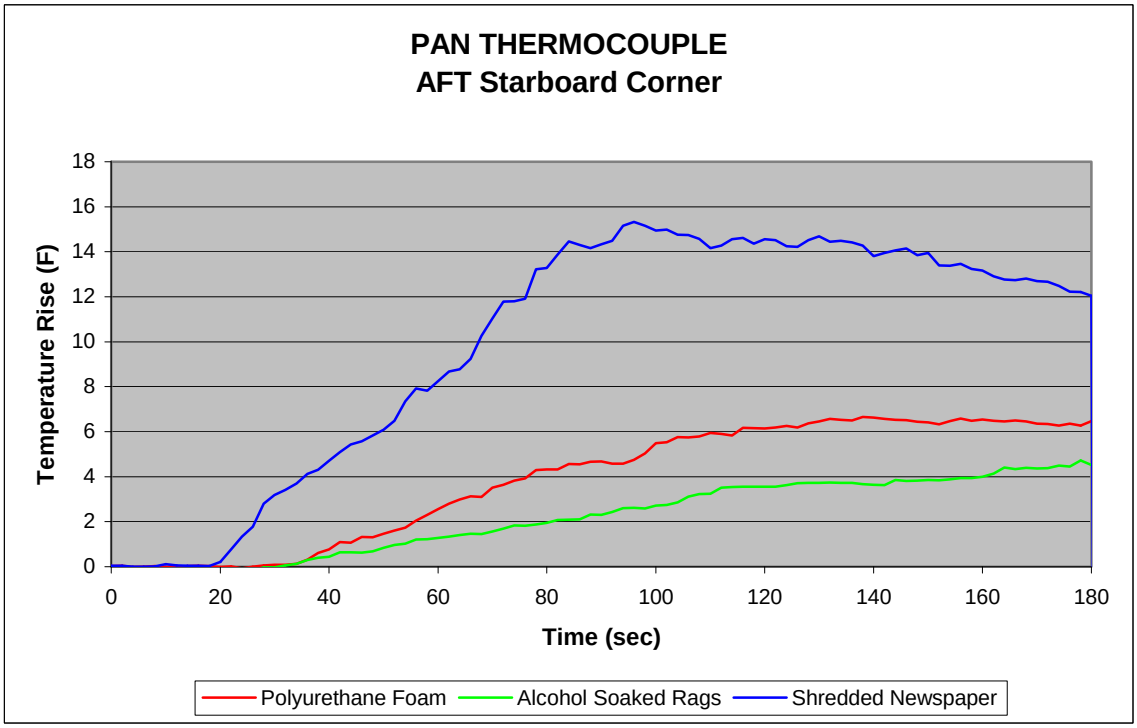

Figure 49. Aft Starboard Corner Temperature Rise Results

5.4 EXPERIMENTAL NUISANCE TESTING.

5.4.1 Vaporizer.

The first nuisance source that was experimented with was the household vaporizer source. As explained in section 4.1.2, the vaporizer was mounted on top of an extension piece that rested on the compartment floor. This provided realistic responses from the smokemeter and the MIC, which is shown in figures 50 and 51. Figure 50 revealed a gradual linear decrease in the percent light transmission until about 30 seconds where the minimum of 42%LT/ft was attained. The smokemeter stayed at this level for the duration of the 90-second test. Figure 51 revealed the minor effect the vaporizer had on the MIC. Beginning at its reference voltage of about 5.1 volts, the MIC fluctuated as it dropped close to 4.8 volts. The ionization chamber produced only a small drop in voltage because it was exposed to droplets larger than 1 micron in size that condensed out from the water vapor. Gas concentration and temperature rise data were negligible for the vaporizer source.

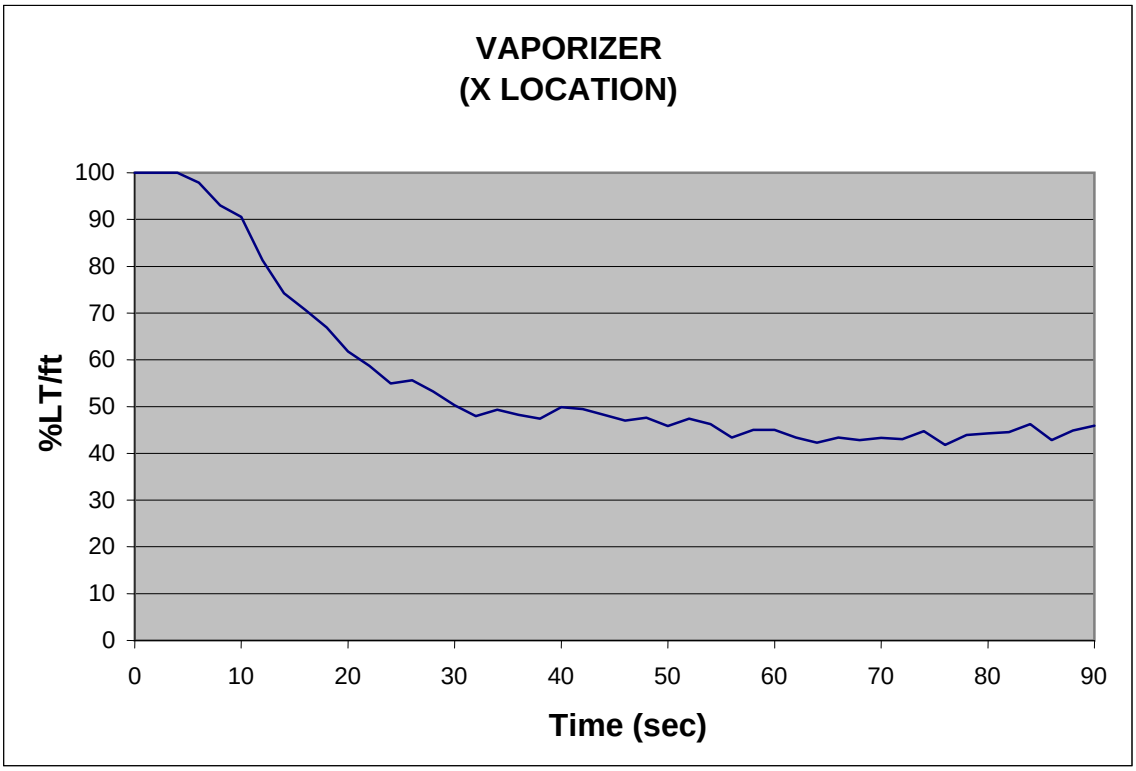

Figure 50. Vaporizer Average Percent Light Transmission per Foot at X Location

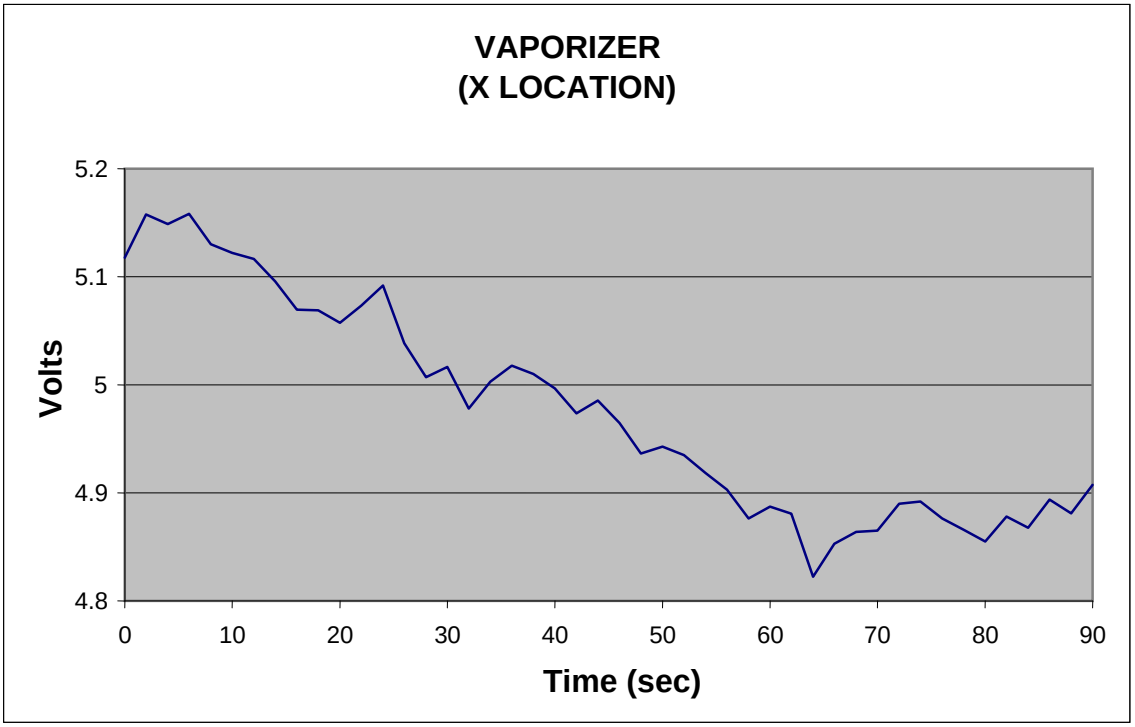

Figure 51. Vaporizer Average MIC Voltage at X Location

5.4.2 Arizona Test Dust.

Figure 52 shows the reduction in light transmission caused by agitated test dust under the multisensor detector. The smokemeter reached a minimum percent light transmission level of almost 91% at around 10 seconds. The light transmission values fluctuated above and below the potential alarm point of 96%LT/ft after the initial minimum value at 10 seconds. Figure 53 shows the voltage output of the MIC sensor when exposed to the test dust. The test dust caused a minimum voltage close to 2.8 volts, which was sufficient to cause the MIC to alarm. The MIC output rose back above the alarm threshold after about 20 seconds. This information was taken into consideration when setting threshold levels in the logic-based algorithm. Arizona test dust had no effect on gas concentration and temperature rise levels.

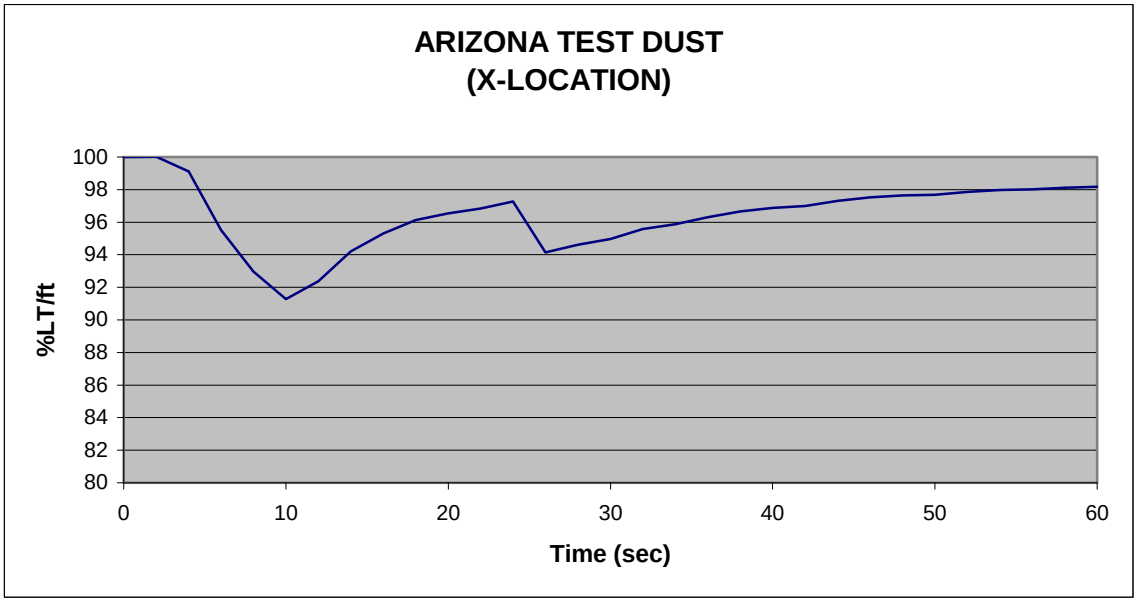

Figure 52. Arizona Test Dust Average Percent Light Transmission per Foot at X Location

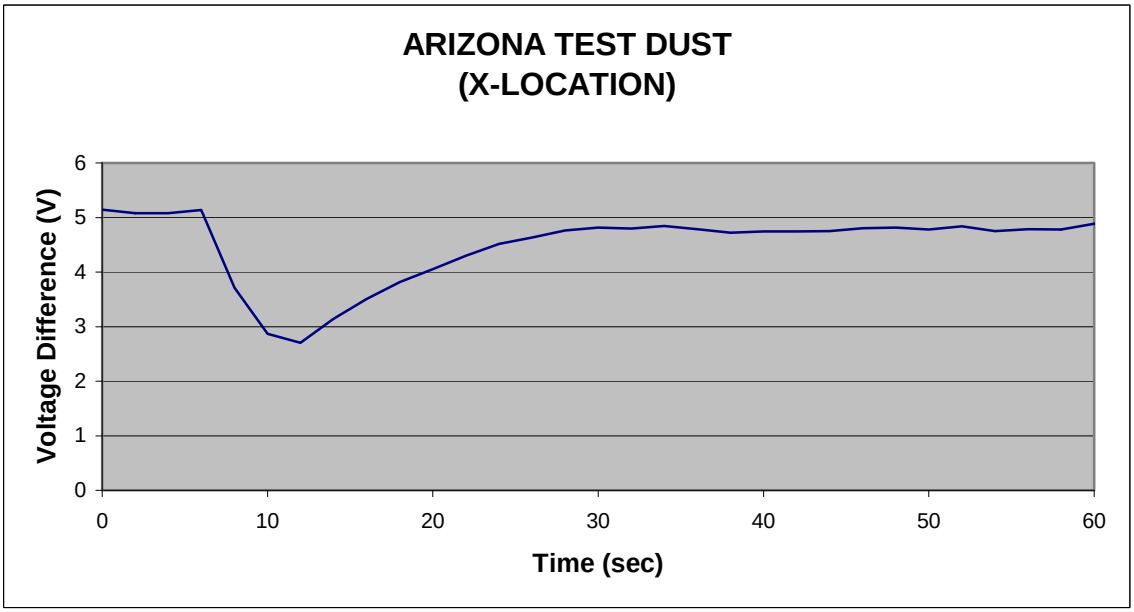

Figure 53. Arizona Test Dust Average MIC Voltage at X Location

5.4.3 Heat Gun.

Figure 54 shows the temperature rise produced from the heat gun located 39 inches directly below the recessed pan. The pan thermocouple experienced the largest temperature rise of about 23 degrees. Figure 55 and 56 showed that the smokemeter and MIC also experienced some significant unexpected effects from the heat gun. To try to determine the reason for the heat gun effect on these instruments, additional tests were conducted with a radiant heat source. The radiant source produced a similar temperature rise on the pan thermocouple but did not include the forced ventilation produced by the heat gun. These tests produced a negligible change to the smokemeter but still caused a change in the MIC voltage output. The change to the MIC was much less than the heat gun test with a minimal output of about 4 volts. The heat gun test appears to have caused some distortion and vibration of the smokemeter mirrors that reduced the intensity of the laser beam striking the photodetector. The air velocity from the heat gun appears to significantly lower the MIC output compared to the effect of heat alone in the radiant heat test. These results increase the uncertainty of the smokemeter and MIC data in the previous fire tests.

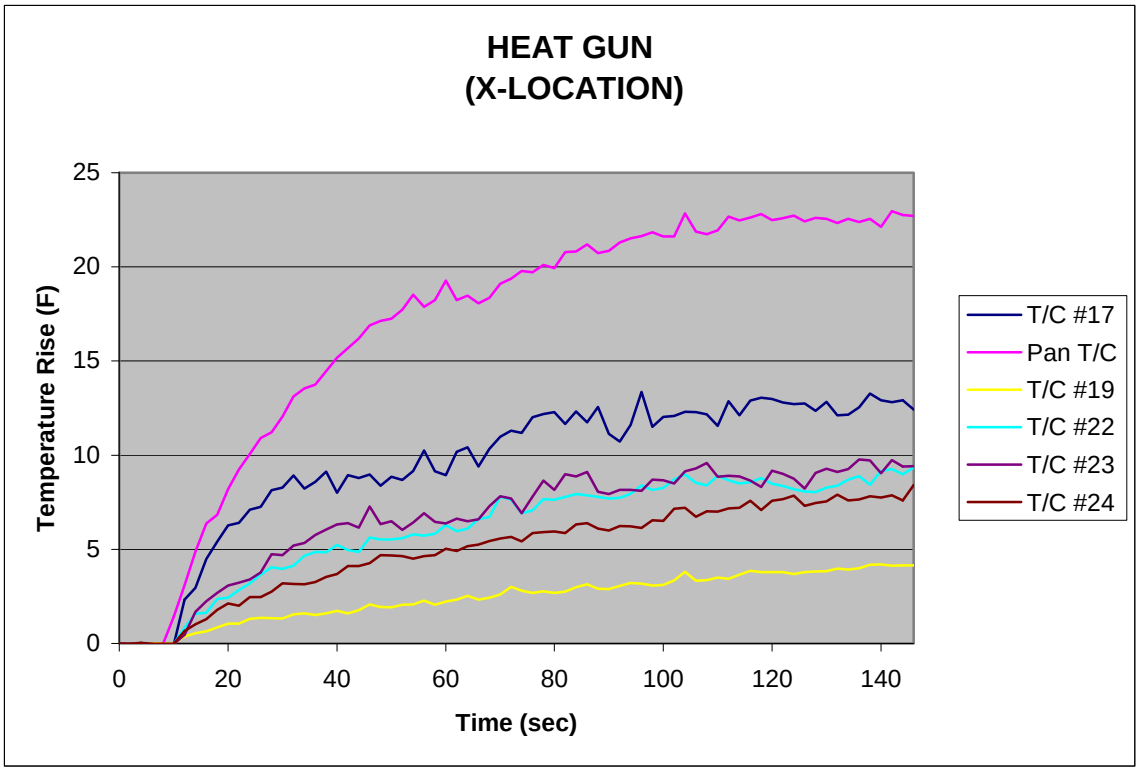

Figure 54. Heat Gun Average Temperature Rise at X Location

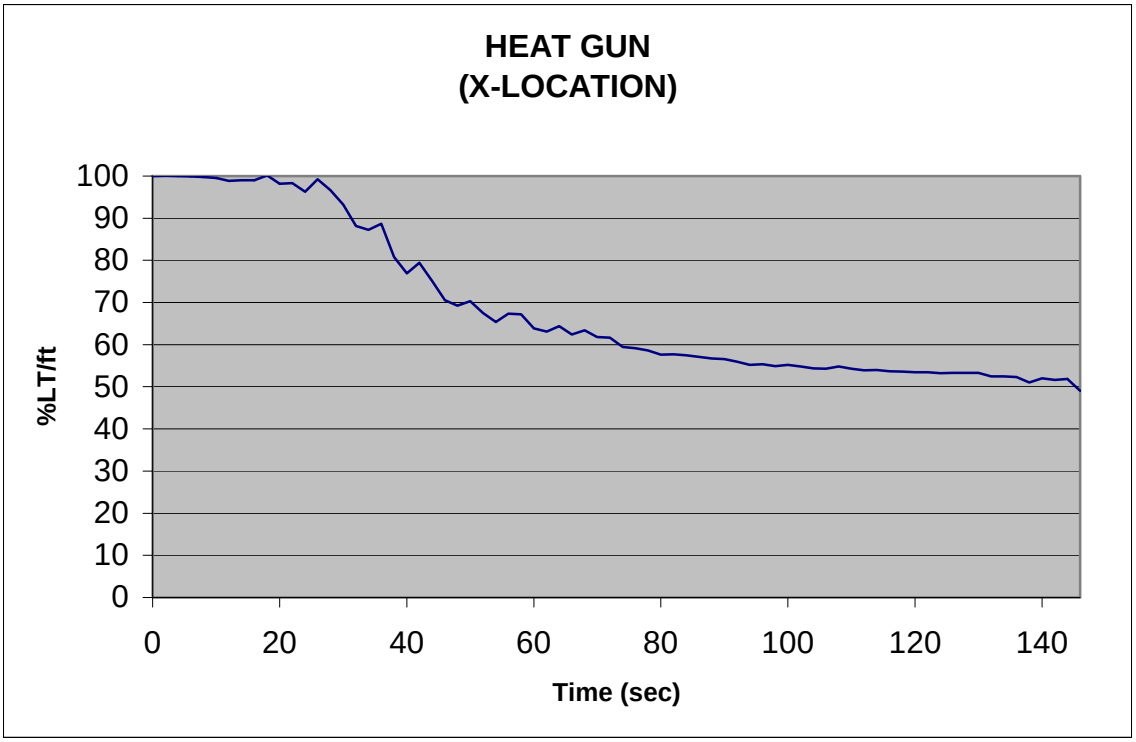

Figure 55. Heat Gun Average Percent Light Transmission per Foot at X Location

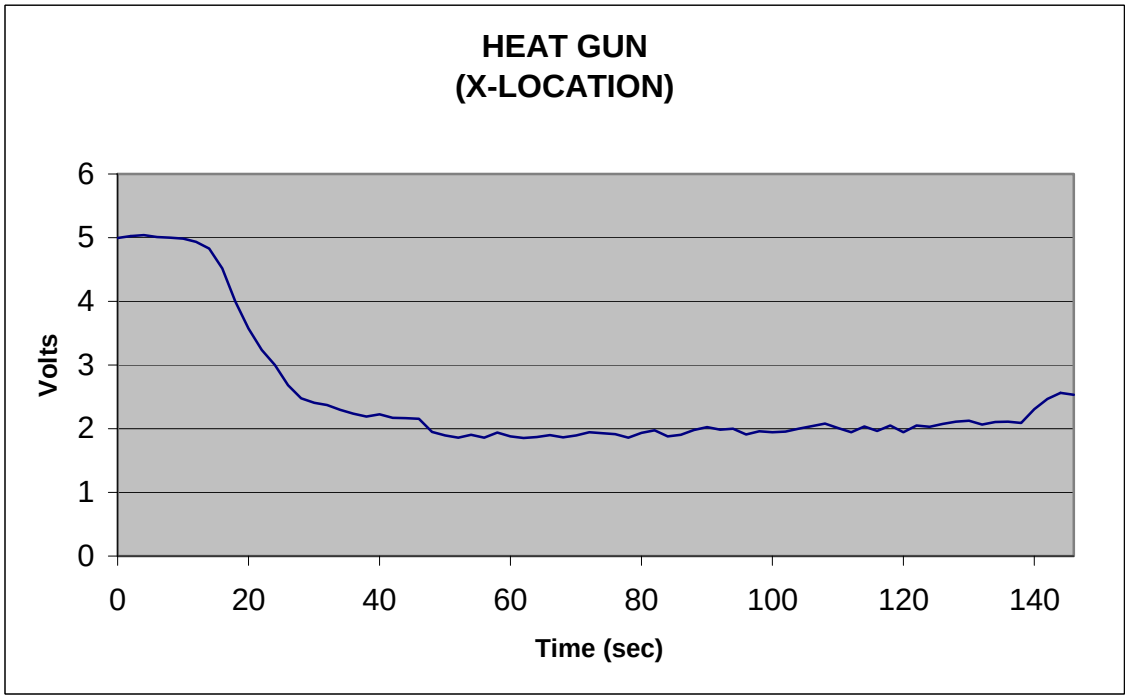

Figure 56. Heat Gun Average MIC Voltage at X Location

5.4.4 Exhaust Fumes.

Gasoline- and diesel-powered equipment is commonly present adjacent to cargo compartments during loading and unloading. To simulate this potential false alarm scenario, a warehouse forklift was positioned just outside of the cargo compartment open door with the forklift exhaust directed inside the cargo compartment. Figure 57 shows the effect that the exhaust fumes had on the smokemeter. The smokemeter decreased gradually to almost 94%LT/ft, and then slowly increased back to a nonalarm level of 98%LT/ft during the 4-minute test. CO and CO_2 gas concentration levels from the forklift nuisance source test are shown in figure 58. Maximum levels of 700 and 500 ppm were obtained for CO_2 and CO, respectively. The forklift exhaust fumes had no effect on the MIC and thermocouples.

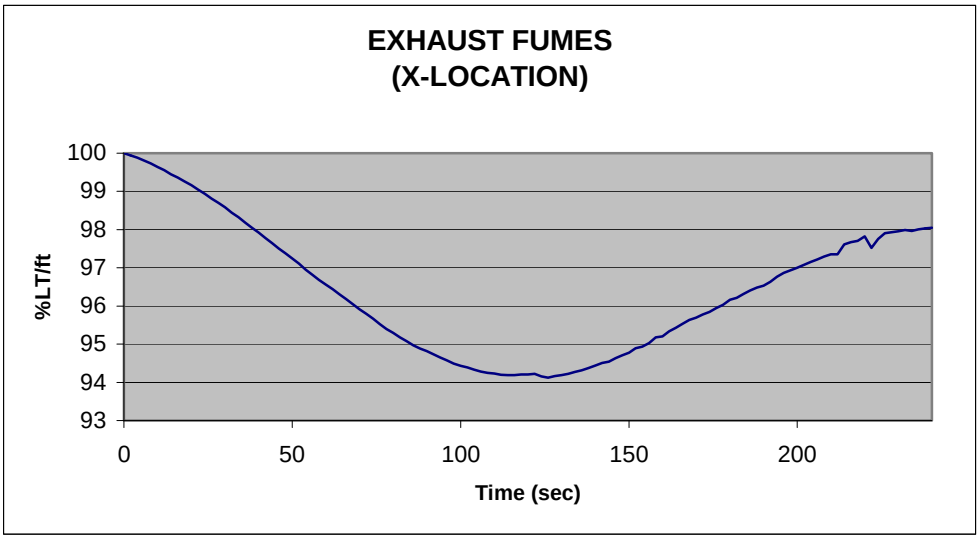

Figure 57. Exhaust Fumes Average Percent Light Transmission per Foot

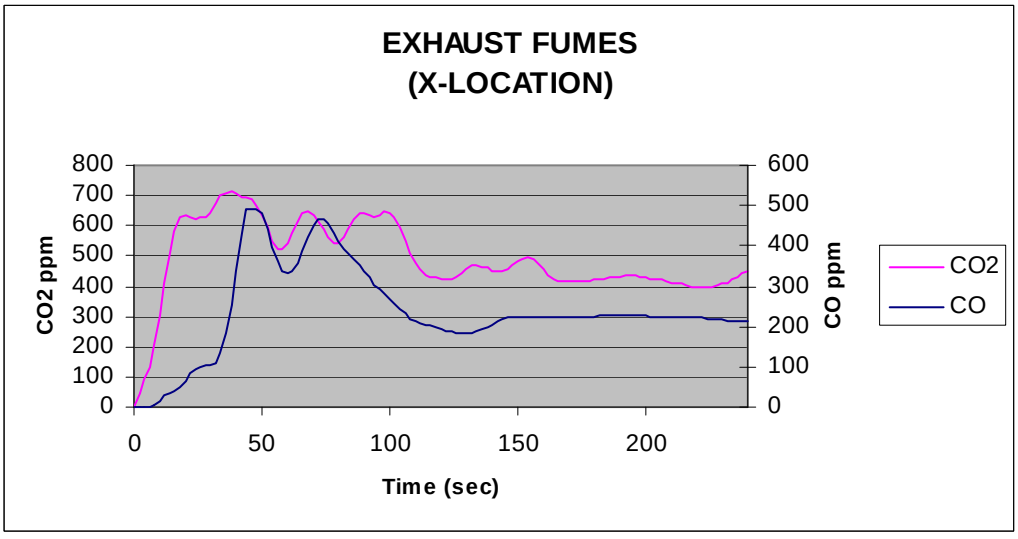

Figure 58. Exhaust Fumes Average CO and CO_2 Gas Concentrations

5.4.5 Occupied Compartment.

A potential source of CO_2 in a cargo compartment is that caused by respiration from a baggage handler inside the compartment and by the carriage of livestock. Figure 59 is a plot of the human CO_2 production from one individual in the cargo compartment. The individual occupied the compartment for a 300-second time period between 100 and 400 seconds. The compartment was then vacated and data was recorded for an additional 60 seconds. The presence of an individual within the cargo compartment had no effect on the MIC, temperature rise levels, or the smokemeter.

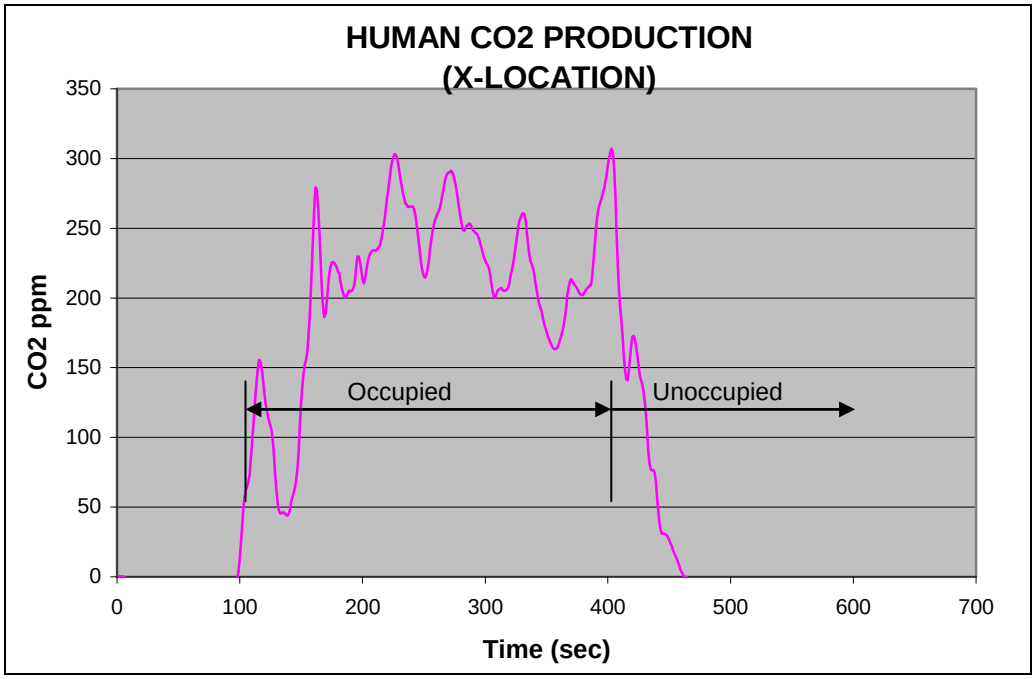

Figure 59. Occupied Compartment Human CO_2 Gas Production (1 person)

5.5 PERIMETER EXPERIMENTAL NUISANCE TESTING.

The Arizona test dust nuisance source was the only nuisance source used for perimeter testing since the other four sources produced no significant effect at small distances away from the instrumentation. The actual box setup and procedure for releasing the test dust was discussed previously in section 4.1.2. The Arizona test dust tests were conducted at two perimeter locations. The two locations were 2 and 4 feet forward of the recessed pan. Figures 60 and 61 show smokemeter and MIC response at the first location, respectively. The test dust surpassed the photoelectric detector threshold point of 96%LT/ft at 6 seconds and the MIC threshold point of 4.1 volts at 8 seconds. Figures 62 and 63 showed the results from the smokemeter and MIC at the second location, respectively. These figures show that the Arizona test dust at 4 feet away from the detectors did not produce significant changes in either the MIC or smokemeter. The Arizona test dust did not produce a change in temperature or CO and CO_2 at either location.

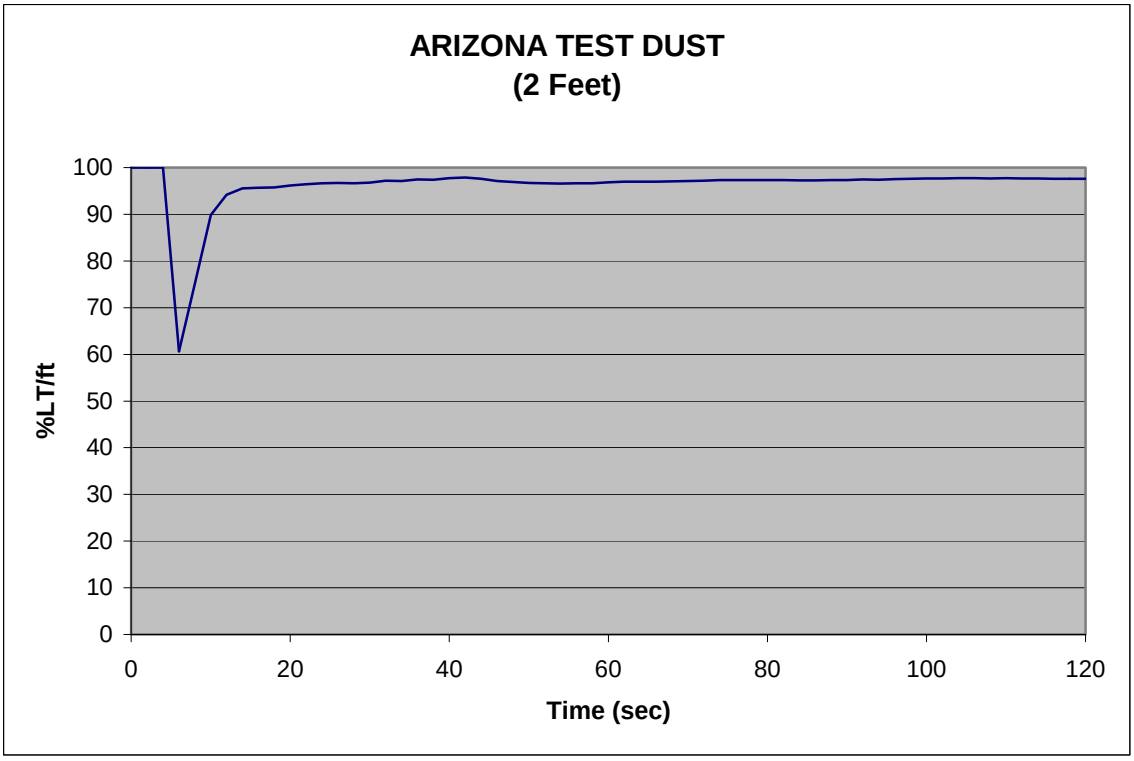

Figure 60. Arizona Test Dust Percent Light Transmission per Foot (2 Feet From Recessed Pan)

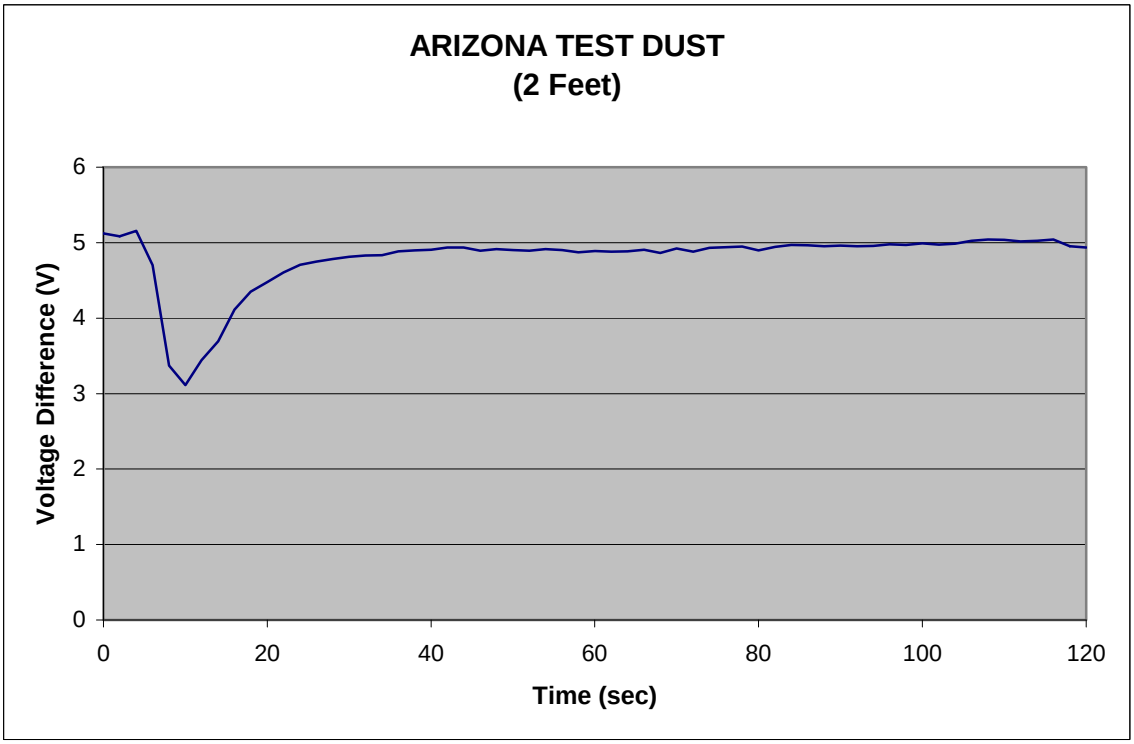

Figure 61. Arizona Test Dust MIC Voltages (2 Feet From Recessed Pan)

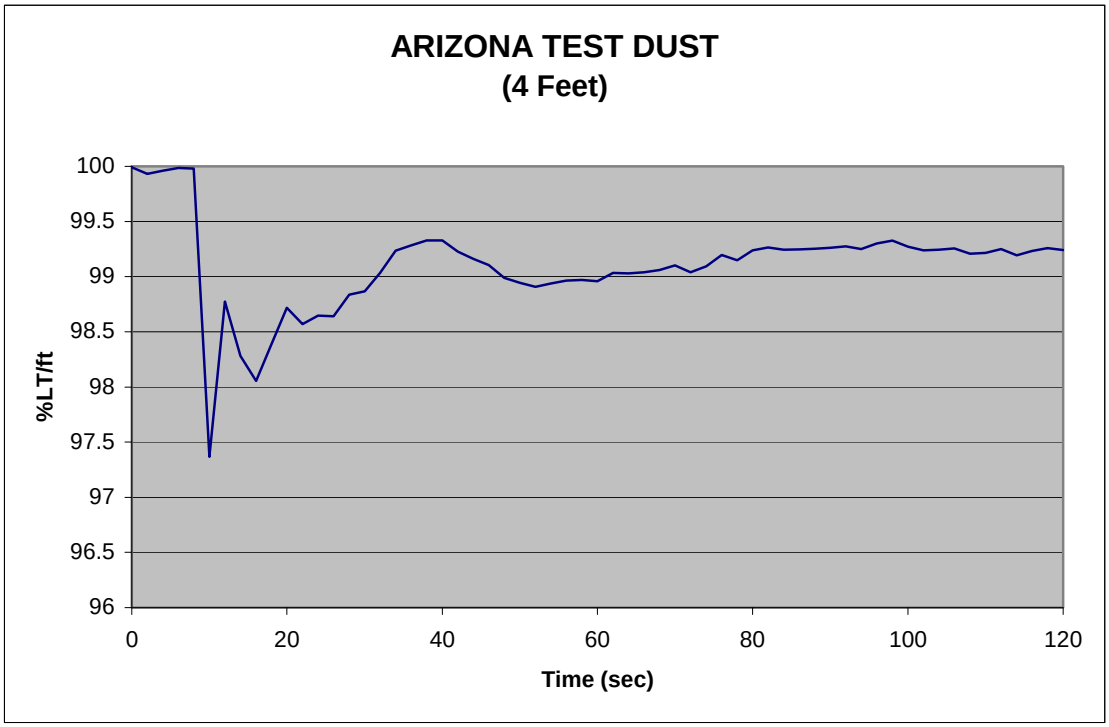

Figure 62. Arizona Test Dust Percent Light Transmission per Foot (4 Feet From Recessed Pan)

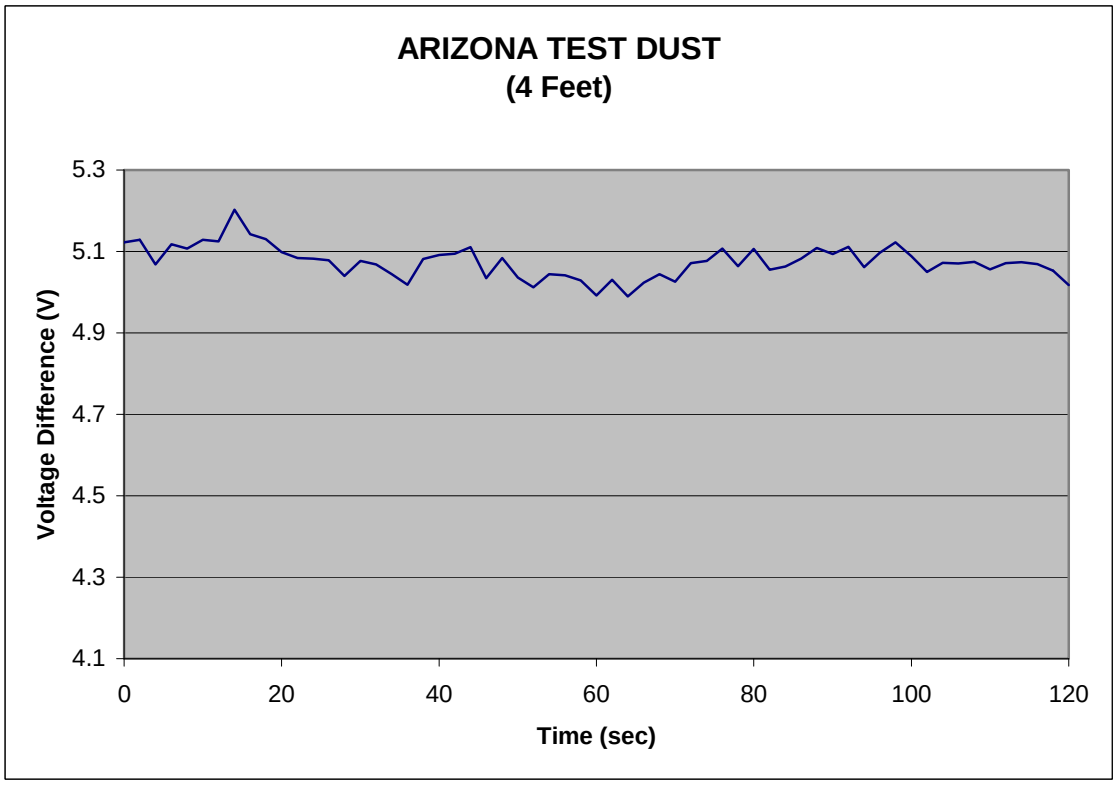

Figure 63. Arizona Test Dust MIC Voltages (4 Feet From Recessed Pan)

5.6 ALGORITHM DEVELOPMENT.

The idea behind developing an algorithm based on four sensors required a select combination of various parameters. The four sensors that made up the multisensor detector each contributed two important parameters to the logic-based algorithm. Apart from using the primary output from each sensor, the rate of rise of each primary output was found to be an integral part of designing a more complete algorithm. A complete algorithm that would be able to detect fires is based on the following:

- Temperature changes from ambient
- Gas concentration changes from ambient (CO and CO_2)
- Percent light transmission per foot
- MIC voltage difference
- Rate of rise of temperature
- Rate of rise of gas concentration (CO and CO_2)
- Rate of decline of percent light transmission per foot
- Rate of decline of MIC voltage difference

By combining the rate of rise with the changes from ambient conditions parameter, it was possible to design a completely optimized algorithm. To reduce the complexity of the multiparameter algorithm development process, a threshold matrix was designed. The threshold matrix displayed all the extreme values obtained by each sensor for each particular fire source or nuisance source for both x location testing and perimeter testing. The rate of rise extreme values were also included in the matrix. The matrix was then characterized by sections beginning with the resin block testing, from both the x location and the perimeter. This was followed by the extreme detector level results obtained from nuisance sources and real fire sources at the x location, along with each sources' respective perimeter testing. Table 2 shows the matrix of extreme detector levels for the resin block and nuisance sources along with their respective perimeter locations. Table 2 also lists the extreme rate of rise levels attained for each sensor for all five nuisance sources, the resin block, and respective perimeter testing. The table allowed for easy characterization of vital information such as the lowest possible voltage difference attained by the MIC, or the lowest percent light transmission achieved by the smokemeter for a particular location. The basis for setting primary algorithm threshold levels was predominantly influenced by the nuisance source data shown in table 2. The algorithm development process involved trial and error by choosing arbitrary values influenced by the extreme values from nuisance source data from each sensor output in the threshold matrix to produce alarm response times within 1 minute, while providing false alarm immunity. The threshold matrix indicated the extremities of how each fire or nuisance source impacted each of the sensors. This information was valuable because, during algorithm development, it was essential to know which fire or nuisance source had a greater impact on each sensor. This allowed for characterizing the behavior of each sensor with reference to the fire or nuisance source that it was most sensitive to.

Table 2. Extreme Detector Levels for Resin Block and Nuisance Sources for X Location and Perimeter Locations

	MIC (Volts)	Rate of Rise (Volts/sec)	Smokemeter (%LT/ft)	Rate of Rise (%LT/ft/sec)	CO (ppm)	Rate of Rise CO	CO_2 (ppm)	Rate of Rise CO_2	Temp. Change (°F)	Temp. Rate of Rise
REFERENCE SOURCE										
Resin block (X location)	0.589	-0.522	48.743	-3.036	108.889	4.580	1497.116	49.026	9.831	0.815
PERIMETER TESTING										
Resin block (Fwd)	0.583	-0.246	59.959	-1.522	86.243	3.571	1076.050	34.180	3.831	0.312
Resin block (Aft)	0.447	-0.340	55.755	-0.010	88.763	2.369	997.473	58.431	6.782	0.302
Resin block (Sidewall)	0.691	-0.391	53.372	-2.722	94.696	2.777	1245.117	24.185	5.352	0.332
NUISANCE SOURCE										
(X location)										
Arizona test dust (Container)	2.801	-0.694	91.276	-1.798	0.088	0.047	0.135	0.078	0.037	0.018
Vaporizer (Fog formation)	4.822	-0.029	41.823	-4.653	0.107	0.076	5.231	0.619	2.159	0.289
Exhaust fumes (Forklift loading)	4.845	-0.046	94.126	-0.149	493.172	45.242	712.394	55.237	0.294	0.137
Heat gun (Heated container)	1.854	-0.262	49.049	-3.982	0.274	0.106	0.539	0.144	22.967	0.889
Occupied compartment (Human)	4.850	-0.023	98.966	-0.029	0.095	0.024	307.159	23.041	0.087	0.026
PERIMETER TESTING										
Arizona test dust (Under pan)	2.705	-0.713	70.513	-10.582	0.045	0.028	0.103	0.087	0.046	0.031
Arizona test dust (2 feet)	3.110	-0.665	60.638	-19.684	0.045	0.028	0.103	0.087	0.046	0.031
Arizona test dust (4 feet)	4.990	-0.038	97.366	-1.308	0.045	0.028	0.103	0.087	0.046	0.031

Temp. = Temperature

Table 3 displays the extreme detector levels for all five fire sources. Extreme detector levels for the perimeter testing of alcohol-soaked rags, polyurethane foam, and shredded newspaper were also listed in the table. The forward starboard corner and the aft starboard corner perimeter data were also averaged, and detector levels were characterized and listed for each sensor. Rate of rise data for all sensors for each fire test was also calculated, and their extreme levels were included in the matrix to assist with algorithm development.

With the creation of tables 2 and 3, the following methodology was implemented when the first basic algorithm was designed.

- For the MIC, a value was chosen that was below most of the extreme levels from nuisance sources. This eliminated alarms from all nuisance sources except for the Arizona test dust and the heat gun.

- For the smokemeter, values that were relatively close to the TSO-C1d, about 96%LT/ft, were chosen. This was done to maintain current detection levels of photoelectric detectors.

- For the gas probe, a value that was above most of the extreme levels for both CO and CO_2 gas concentration for all nuisance sources was chosen. This eliminated alarms from all nuisance sources except the exhaust fumes and the occupied compartment.

- For the thermocouple, a value that was above most of the extreme levels for all nuisance sources was chosen. This eliminated alarms from all nuisance sources except the heat gun.

The above methodology provided the blueprint for designing five algorithms for evaluation. Although there are infinitely many combinations of sensor levels, the advantage of implementing a multisensor algorithm over conventional detectors was the focus of this report. After threshold levels for each sensor were selected, the next step was to incorporate a simple algorithm based on IF, AND, OR logic. All algorithms were tested using Microsoft Excel macros that applied each algorithm to data produced from all fire and nuisance sources, per time step. The first alarm algorithm had the following criteria that would trigger the multisensor detector into alarm mode:

$$\text{IF } \{ (\text{CO ppm} > 2 \text{ OR } CO_2 \text{ ppm} > 30) \text{ AND } (\,^\circ\text{F} > 3 \text{ OR VOLTS} < 4.7)) \quad (1)$$

$$\text{AND } (\%\text{LT/ft} < 97) \} \text{ THEN} \rightarrow \text{ALARM}$$

Table 3. Extreme Detector Levels for All Fire Sources

	MIC (Volts)	Rate of Rise (Volts/sec)	Smokemeter (%LT/ft)	Rate of Rise %LT/ft	CO (ppm)	Rate of Rise CO	CO_2 (ppm)	Rate of Rise CO_2	Temp. Change (°F)	Temp. Rate of Rise
FIRE SOURCES										
(X location)										
FLAMING SOURCES										
Denatured alcohol (40 mL)	4.552	-0.038	86.089	-1.239	1.624	0.119	1831.611	99.377	13.154	0.529
Alcohol-soaked rags	1.430	-0.322	83.655	-1.184	14.191	1.428	1880.348	110.544	14.674	1.016
Polyurethane foam	1.390	-0.736	91.385	-0.702	15.128	2.211	2098.261	321.620	23.051	2.844
SMOLDERING SOURCES										
Shredded newspaper	1.491	-0.497	51.799	-2.808	171.324	24.803	1994.328	276.974	33.145	2.398
Suitcase	1.965	-0.103	64.367	-1.744	372.643	10.697	346.922	9.406	1.423	0.095
PERIMETER TESTING										
Alcohol-soaked rags (Average)	1.341	-0.257	95.627	-0.195	21.074	1.508	1885.504	83.748	4.619	0.117
Polyurethane foam (Average)	1.216	-0.247	94.604	-0.373	6.703	0.779	2070.223	192.934	5.699	0.200
Shredded newspaper (Average)	0.785	-0.695	72.410	-2.449	157.376	19.125	1912.648	214.622	13.945	0.391
Alcohol-soaked rags (Fwd)	1.370	-0.271	96.955	-0.279	2426.186	112.548	1678.543	50.625	3.659	0.166
Polyurethane foam (Fwd)	1.278	-0.501	92.476	-0.754	1011.260	157.490	2044.346	385.902	5.910	0.276
Shredded newspaper (Fwd)	0.497	-0.990	74.829	-1.475	1194.612	140.035	1764.622	369.124	12.777	0.670
Alcohol-soaked rags (Aft)	1.198	-0.287	90.787	-0.512	1385.884	172.563	2032.288	46.734	5.055	0.139
Polyurethane foam (Aft)	1.074	-0.431	94.169	-0.375	838.361	43.948	2096.167	124.795	6.656	0.225
Shredded newspaper (Aft)	0.942	-0.745	69.521	-3.422	1952.917	367.176	2060.719	429.367	15.32 7	0.651

Temp. = Temperature

In the logic-based algorithm, the first set of criteria that had to be realized dealt with only gas concentration levels. Once this criterion was met, the algorithm proceeded onto the thermocouple temperature rise and MIC criteria. Finally, if the fire signature being analyzed had successfully passed the previous two sets of criteria, the last would be that of the smokemeter. Once all criterion and threshold levels were satisfied, the algorithm signaled the multisensor detector into alarm mode. This primary algorithm included only the changes from ambient conditions for all sensors, not rate of rise criteria. False alarm immunity and faster alarm time response were the main goals behind the algorithm, and they can be achieved by simple logical statements. For example, to provide immunity from the heat gun, test dust, and vaporizer, the inclusion of gas concentration criteria in the algorithm would prevent the detector from going into alarm mode. The importance of the threshold matrix can be seen through this simple example. The matrix gave indication as to which sensor was susceptible to a particular fire or nuisance source and at what levels it was prone to alarm at.

The next algorithm that was considered was solely dependent on the rate of rise of each sensor output. The logic behind designing this algorithm was the same as that for the first algorithm based on changes from ambient. Acceptable rate of rise values for all sensors that were above those of most of the nuisance alarm thresholds were chosen. After selection of these values, combinations of different criteria sets were used to design the new algorithm. The logical expressions below show the actual algorithm:

$$\text{IF } \{ (d[CO]/dT > 1 \text{ OR } d[CO_2]/dT > 10)$$

$$\text{AND } (d[\%LT/ft]/dT > 0.1 \text{ OR } d[VOLTS]/dT > 0.1 \text{ OR } d[°F]/dT > 0.15) \} \quad (2)$$

$$\text{THEN} \rightarrow \text{ALARM}$$

For incoming fire signature samples, the first set of alarm algorithm criteria needed to be satisfied involved gas concentration rate of rise levels. This was due to the aforementioned reasoning that gas criterion would immediately distinguish between most nuisance sources and real fire sources. If this initial criteria set was realized, then the possibility of a real fire was imminent and the sample had to then pass the combined rate of rise criteria set for the remaining sensors.

After using the changes from ambient of all four sensors and the rate of rise levels of each sensor independently to formulate two different algorithms, a combination of the changes from ambient and rate of rise parameters was desired for possible optimization. Three new optimized algorithms consisting of specific combinations of the two previously mentioned algorithms were designed. The logical expression statement below was the first combination algorithm created:

$$\text{IF}\{ (d[CO]/dT > 1 \text{ OR } d[CO_2]/dT > 10)$$

$$\text{AND } (d[\%LT/ft]/dT > 0.1 \text{ OR } d[VOLTS]/dT > 0.1 \text{ OR } VOLTS < 4.7) \} \quad (3)$$

$$\text{THEN} \rightarrow \text{ALARM}$$

The only combination that was used here was the inclusion of the last AND logical expression that required the MIC voltage difference to be less than 4.7 volts. The next algorithm was a combination of sensors and only CO gas concentration levels. This was then followed by a similar algorithm using sensor combinations with CO_2, and not CO. This study was done hoping to determine whether or not one gas species would be more beneficial in the fire detection process over the other. The influence was measured with regards to detector response time, actual alarm versus no alarm comparison, and the effectiveness of the gas criteria along with the combination algorithm. Below is the actual CO combination algorithm:

IF {(CO ppm > 2 OR d[CO]/dT > 1) AND

(VOLTS < 4.7 OR °F > 3 OR %LT/ft < 94 OR d[%LT/ft]/dT > 0.15 OR (4)

d[VOLTS]/dT > 0.1) }

THEN → ALARM

The CO algorithm above combined all four sensors using both rate of rise and changes from ambient conditions data, with the exception of CO_2 gas concentration.

The performance of this algorithm was compared to that of the CO_2 based algorithm shown below:

IF { (CO_2 ppm > 7.5 OR d[CO_2]/dT > 5) AND (VOLTS < 4.7 OR °F > 3 OR

%LT/ft < 94 OR d[%LT/ft]/dT > 0.15 OR d[VOLTS]/dT > 0.1) } (5)

THEN → ALARM

The CO_2 algorithm above combined all four sensors using both rate of rise and changes from ambient conditions data, with the exception of CO gas concentration. The following section compares the performances of all five algorithms along with those of the conventional photoelectric and ionization detectors.

5.7 DETECTOR PERFORMANCE.

Table 4 shows the alarm times for algorithms 1 through 5, along with the alarm times of the conventional photoelectric and ionization detectors for the resin block fire source and the nuisance sources. Table 5 shows the same information for the remaining five fire sources. Results highlighted in red correspond to a failure for that particular detector or algorithm to detect the fire within 60 seconds or failure from alarming to a nuisance source, whereas an X meant there was no detection at all. For analysis and comparison, the photoelectric alarm threshold point was taken to be 96%LT/ft. Any fire or nuisance source revealing a percent light transmission below 96% returned an alarm mode condition. The ionization detector threshold voltage, discussed in the experimental setup in section 3.2, was found to be 4.1 volts, and all data produced from fire or nuisance sources below this voltage returned an alarm mode condition.

Table 4. Alarm Times for the Resin Block and Nuisance Sources (Seconds)

Reference Source	Algorithm 1	2	3	4	5	Photoelectric	Ionization
Resin block (X location)	20	18	18	24	14	20	20
PERIMETER TESTING							
Resin block (Fwd)	70	48	48	50	48	54	84
Resin block (Aft)	50	50	50	54	50	50	42
Resin block (Sidewall)	38	26	26	38	26	36	42
NUISANCE SOURCE X LOCATION							
Arizona test duct (Container)	X	X	X	X	X	6	8
Vaporizer (Fog formation)	X	X	X	X	X	8	X
Exhaust fumes (Forklift loading)	X	X	X	X	X	70	X
Heat gun (Heated container)	X	X	X	X	X	30	18
Occupied compartment (Human)	X	X	X	X	X	X	X
PERIMETER TESTING							
Arizona test dust (Under pan)	X	X	X	X	X	6	8
Arizona test dust (2 feet)	X	X	X	X	X	6	8
Arizona test dust (4 feet)	X	X	X	X	X	X	X

Table 5. Alarm Times for All Fire Sources (Seconds)

Fires Sources	Algorithm					Photoelectric	Ionization
	1	2	3	4	5		
(X location)							
FLAMING SOURCES							
Denatured alcohol (40 mL)	114	20	80	X	14	118	X
Alcohol-soaked rags	22	14	14	18	14	32	14
Polyurethane foam	12	12	12	14	10	38	10
SMOLDERING SOURCES							
Shredded newspaper	20	16	16	18	16	20	18
Suitcase	60	44	44	46	44	62	126
PERIMETER TESTING							
Alcohol-soaked rags (Average)	28	32	32	36	30	214	34
Polyurethane foam (Average)	34	24	24	28	18	38	22
Shredded newspaper (Average)	32	28	28	32	28	34	22
Alcohol-soaked rags (Fwd)	202	30	30	34	30	X	34
Polyurethane foam (Fwd)	24	24	24	28	22	22	20
Shredded newspaper (Fwd)	38	38	38	40	38	34	36
Alcohol-soaked rags (Aft)	48	36	34	36	32	50	46
Polyurethane foam (Aft)	46	40	40	46	34	52	36
Shredded newspaper (Aft)	46	28	28	30	28	48	22

Both tables provided a definitive comparison between algorithms 1 through 5, which represented the multisensor detector, and those of current aircraft smoke detectors. The two main factors that were discussed for performance analysis of the three detectors were the detectors alarm times and the nuisance immunity of each detector. Improving these two factors for fire detection in aircraft cargo compartments through a multisensor detector algorithm was essentially the main objective of this report.

5.7.1 Detector Alarm Time Comparison.

Algorithms 1, 3, and 4 all produced failure scenarios. Algorithm 1, logically based on changes from ambient conditions, failed to detect (within the 60-second regulation) the resin block and alcohol-soaked rag test at the forward starboard corner, along with the denatured alcohol at the x location. Algorithm 3, the first combination algorithm developed, failed to detect (within 60 seconds) the denatured alcohol alone. This algorithm proved to be successful in detection of all other fire sources within the required time. Algorithm 4, logically based on CO and a combination of all other sensors except CO_2, failed to detect the denatured alcohol test at the x location. Algorithms 2 and 5 were successful in the detection of all fire sources within the required time. They had the fastest alarm times due to increased sensitivity from all sensors and were also successful in the detection of all perimeter fires.

Conventional photoelectric and ionization detectors failed to detect several fires within the 60-second regulation, and some were not detected at all. The photoelectric detector, in the same way as algorithm 1, failed to detect the denatured alcohol fire within 60 seconds. The ionization detector, in the same way as algorithm 4, failed to detect even the presence of the denatured alcohol fire. The photoelectric detector also failed to detect the suitcase fire at the x location and the alcohol-soaked rags at the forward starboard corner location within 60 seconds. The ionization detector again failed to detect the suitcase fire at the x location within 60 seconds, along with the resin block fire at the forward starboard corner location.

5.7.2 Detector Nuisance Immunity Comparison.

The ability to distinguish between real fires and nuisance sources was the next topic to be analyzed to measure the performance of a detector. It was rewarding to note the complete nuisance immunity that was obtained by the multisensor detectors for all five algorithms. The many inconveniences and risks attributed to in-flight false alarm conditions would become obsolete with the capabilities of a multisensor detector. False alarms were only detected by the conventional photoelectric and ionization detectors. Table 4 shows that the primary cargo compartment smoke detection system today, the photoelectric detector, alarmed for four of the five nuisance sources. The secondary type of cargo compartment smoke detection system today, the ionization detector, alarmed for two of the five nuisance sources. The photoelectric and ionization detectors both failed the perimeter test with the Arizona test dust situated on the floor, 2 feet away from being directly beneath the recessed pan.

Table 6 summarizes the performance of each detector in terms of success and failure percentages for all 30 tests. Table 6 shows a 100% success rate for algorithms 2 and 5 in alarming to all fire sources within 60 seconds and not alarming to any nuisance sources. The conventional photoelectric and ionization detectors revealed poor success ratings, at 66.67% and 73.33%,

respectively, compared to the multisensor detector. The results clearly show that the multisensor detector responds faster than both the photoelectric and ionization detectors to all fires, while providing 100% nuisance immunity.

Table 6. Algorithm Results

	Algorithm					Photoelectric	Ionization
	1	2	3	4	5		
Total Tests	30	30	30	30	30	30	30
Failure	4	0	1	1	0	10	8
Successful	26	30	29	29	30	20	22
Failure %	13.33	0.00	3.33	3.33	0.00	33.33	26.67
Successful %	86.67	100	96.67	96.67	100	66.67	73.33

5.8 COMPUTATIONAL ANALYSIS.

A CFD model was used to create a virtual detector to aid in determining the range of the multisensor detector by eliminating the need to conduct numerous experimental fire tests. The range of a detector was valuable information that was pertinent in assessing the overall performance of the multisensor detector within a particular volume. To create this virtual detector, there had to be strong agreement between computational and experimental results. The figures discussed in the following sections show the results comparing computational simulation results to those of actual experimental resin block fire tests at identical locations and conditions.

5.8.1 X Location.

Figure 64 shows the comparison between computational and experimental percent light transmission data. The data shows excellent agreement from 0 to 75 seconds, and again after about 210 seconds. Since the time frame of interest was from 0 to 60 seconds, the model appeared to be a useful tool.

Figure 65 is the comparison of the experimental MIC voltage values to those of the computational MIC voltage values obtained from the x location polynomial correlation equation. The MIC correlation and experimental results were in good agreement from 0 to approximately 50 seconds. The agreement after 50 seconds was poor due to the curve-fitting method of correlation and because the MIC voltage is not indicative of the particle density present after the MIC has gone into alarm.

Figure 66 shows CO and CO_2 gas concentration rise levels for computational and experimental results. It was evident that, although the trends between computational and experimental for CO_2 gas concentrations were relatively the same, the magnitudes of their CO_2 concentrations were completely different. There was poor agreement between computational and experimental CO_2

gas concentration values. For CO, both the trends and the magnitudes were relatively close and therefore, it was safe to say that there exists strong agreement between experimental CO and computational CO gas concentration rise data.

The temperature rise data displayed in figure 67 showed similar trends between computational and experimental values; however, the magnitudes were in poor agreement.

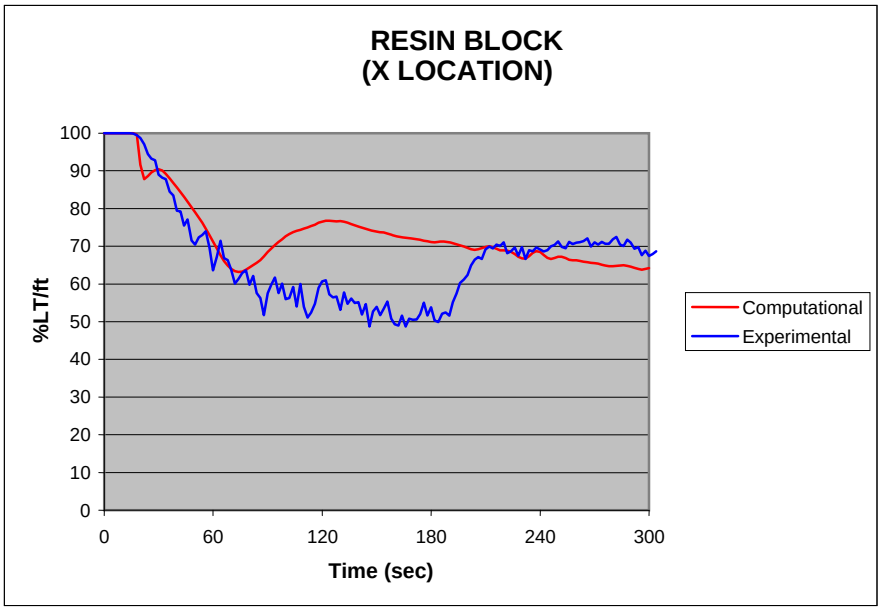

Figure 64. Comparison of Computational and Experimental Resin Block Percent Light Transmission per Foot at X Location

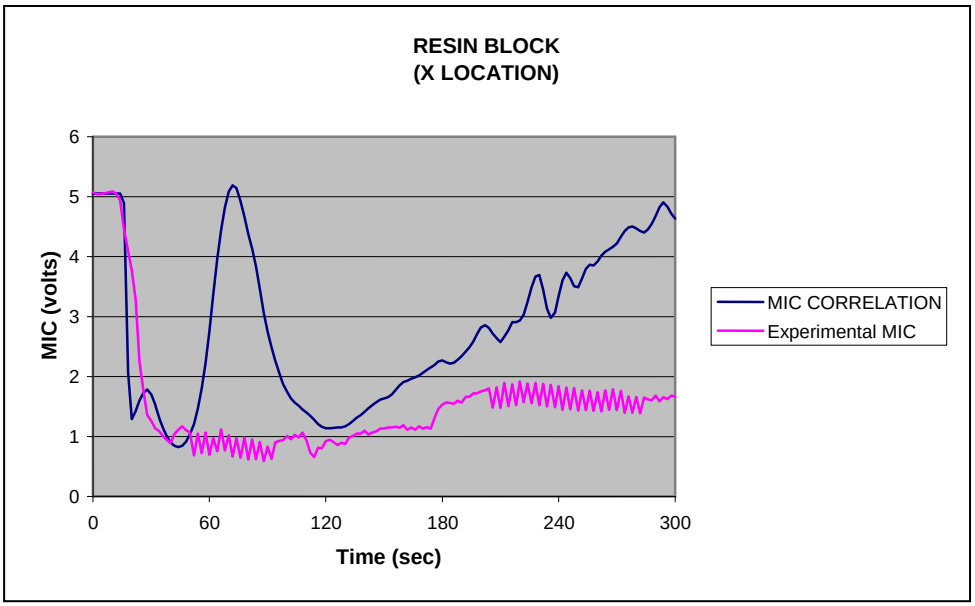

Figure 65. Comparison of Computational and Experimental Resin Block MIC Voltages at X Location

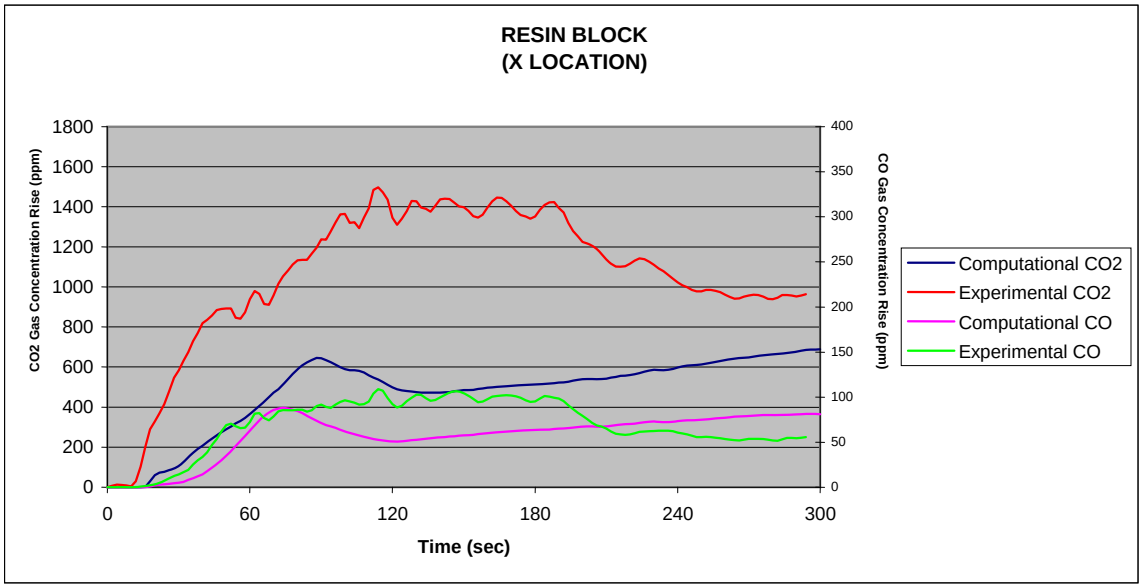

Figure 66. Comparison of Computational and Experimental Resin Block CO and CO_2 Gas Concentrations at X Location

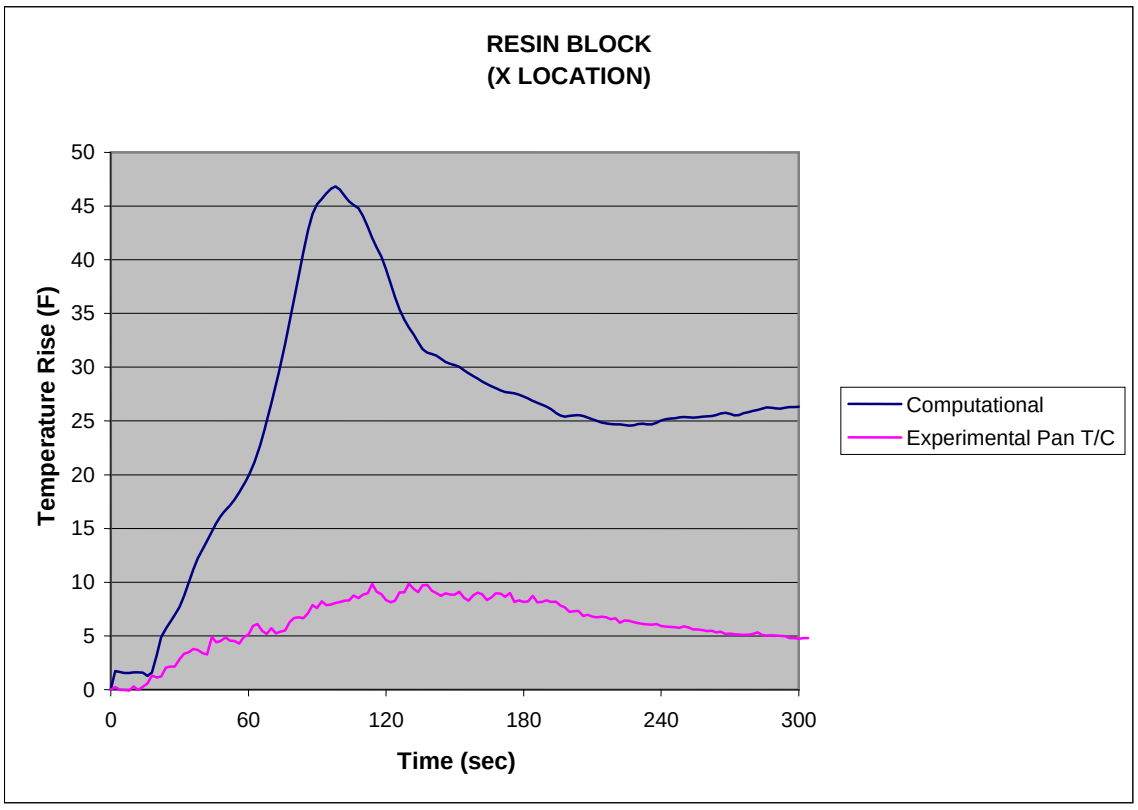

Figure 67. Comparison of Computational and Experimental Resin Block Temperature Rise at X Location

5.8.2 Perimeter Locations.

Figures 68, 69, 72, 73, 76, and 77 compare smokemeter data and MIC voltage data between computational and experimental tests for the forward starboard, aft port, and sidewall starboard locations, respectively. Analysis of each location's respective MIC and smokemeter data revealed that there was strong agreement for both the smokemeter and the MIC, until after about 75 seconds. At this point, both increased and followed the same trends. The obvious reasoning for the similar trends between the MIC correlation and the computational smokemeter data was because the MIC correlation was dependent on the computational smokemeter data through the second-order polynomial. It was important that trends and magnitudes between computational and experimental data for the time period up until 60 seconds for the smokemeter and the MIC were in strong agreement.

Figures 70, 74, and 78 compare gas concentration data between computational and experimental tests for the forward starboard, aft port, and sidewall starboard locations, respectively. There was poor agreement that existed between computational and experimental results for the CO_2 gas concentration data. The computational CO_2 data was significantly lower than those of actual experimental data for all locations. The experimental and computational CO data showed generally good agreement.

Figures 71, 75, and 79 compare temperature rise data between computational and experimental tests for the forward starboard, aft port, and sidewall starboard locations, respectively. These figures showed that computational temperatures were always several degrees higher than experimental temperature data. The aft port location provided the best agreement between computational and experimental temperature data of the three locations. Although magnitudes were relatively accurate for this perimeter location, analysis of the time response and trends between computational and experimental tests revealed discrepancies. For two of the three cases, it appeared that the computational temperature seemed to have a significant time delay, before increasing. The time delay was as much as 25-35 seconds for the aft port location, as shown in figure 75. The largest magnitude difference seen in figure 71 for the forward starboard location was approximately 10 degrees.

Temperature and CO_2 gas concentration comparisons, in general, did not show as strong an agreement as the smokemeter, MIC, and CO gas data. A simple detector alarm time analysis discussed in section 5.8 revealed how significantly close computational and experimental data really were with respect to the relevant parameters of this study.

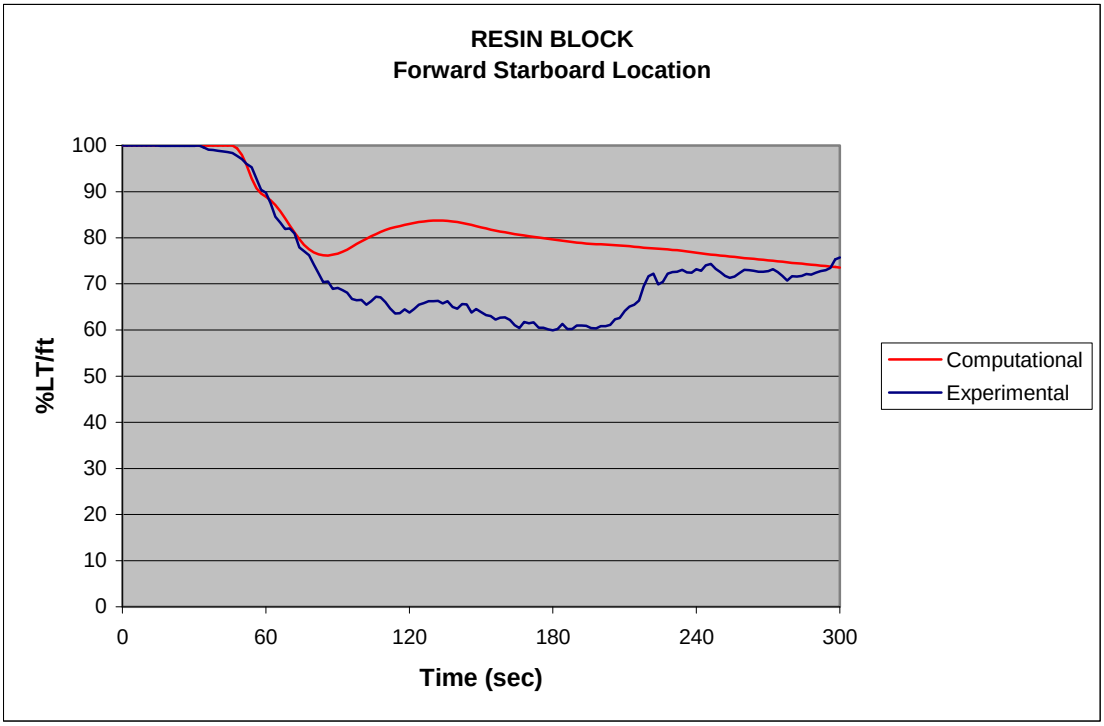

Figure 68. Comparison of Computational and Experimental Resin Block Percent Light Transmission per Foot at Forward Starboard Location

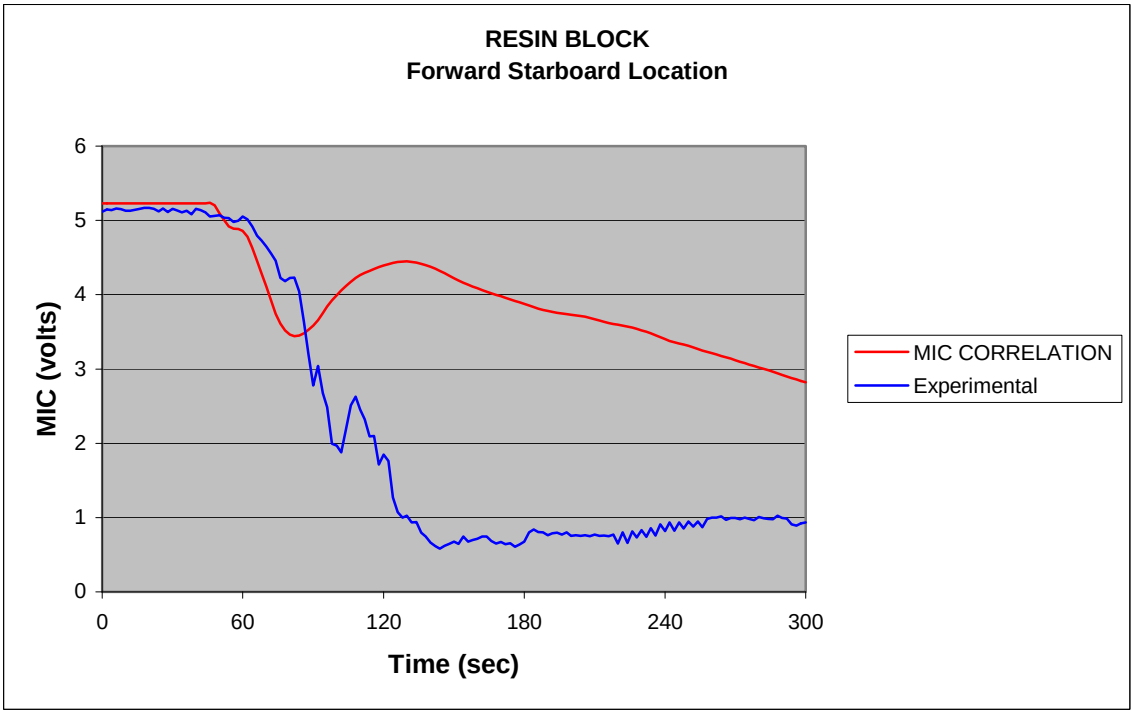

Figure 69. Comparison of Computational and Experimental Resin Block MIC Voltages at Forward Starboard Location

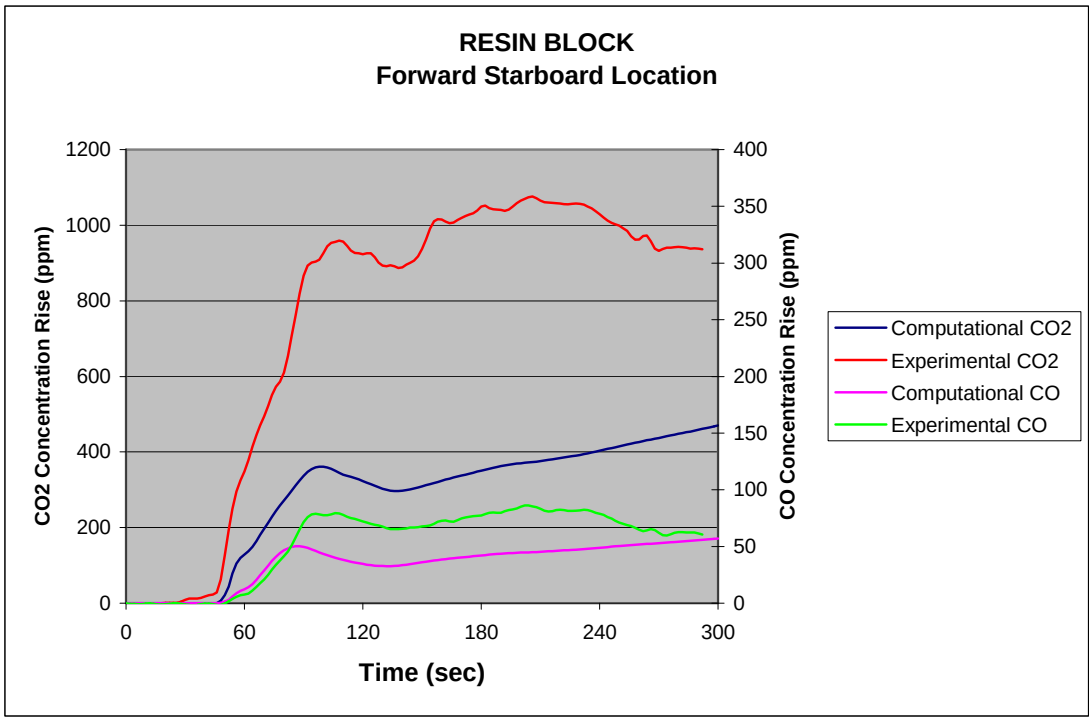

Figure 70. Comparison of Computational and Experimental Resin Block CO and CO_2 Gas Concentrations at Forward Starboard Location

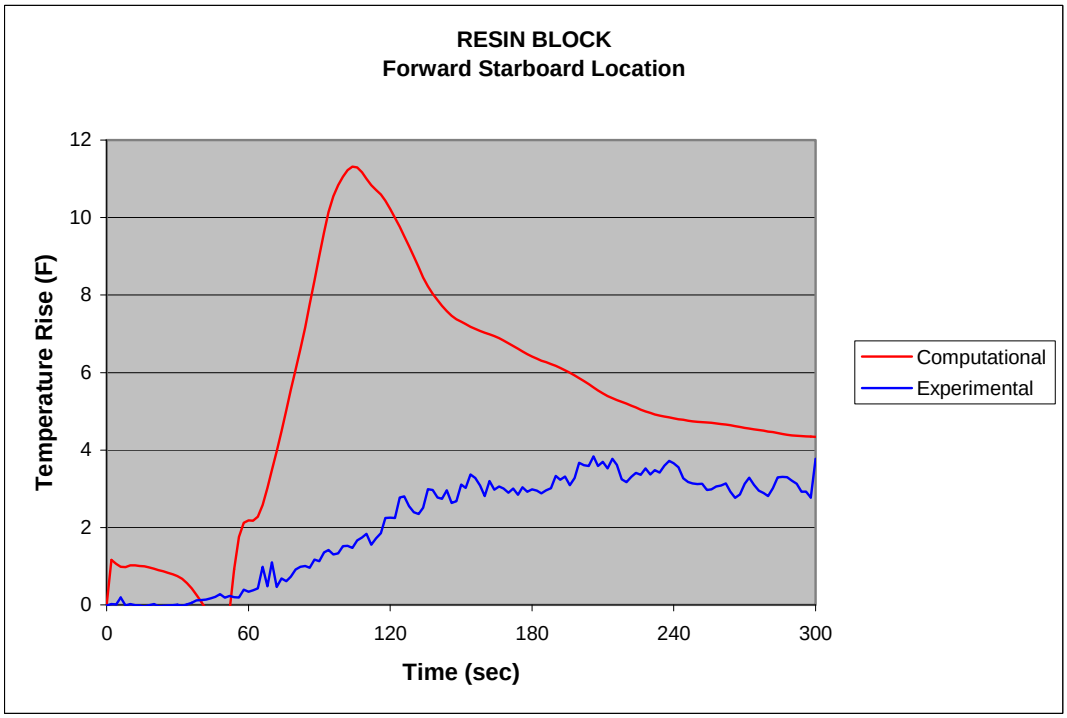

Figure 71. Comparison of Computational and Experimental Resin Block Temperature Rise at Forward Starboard Location

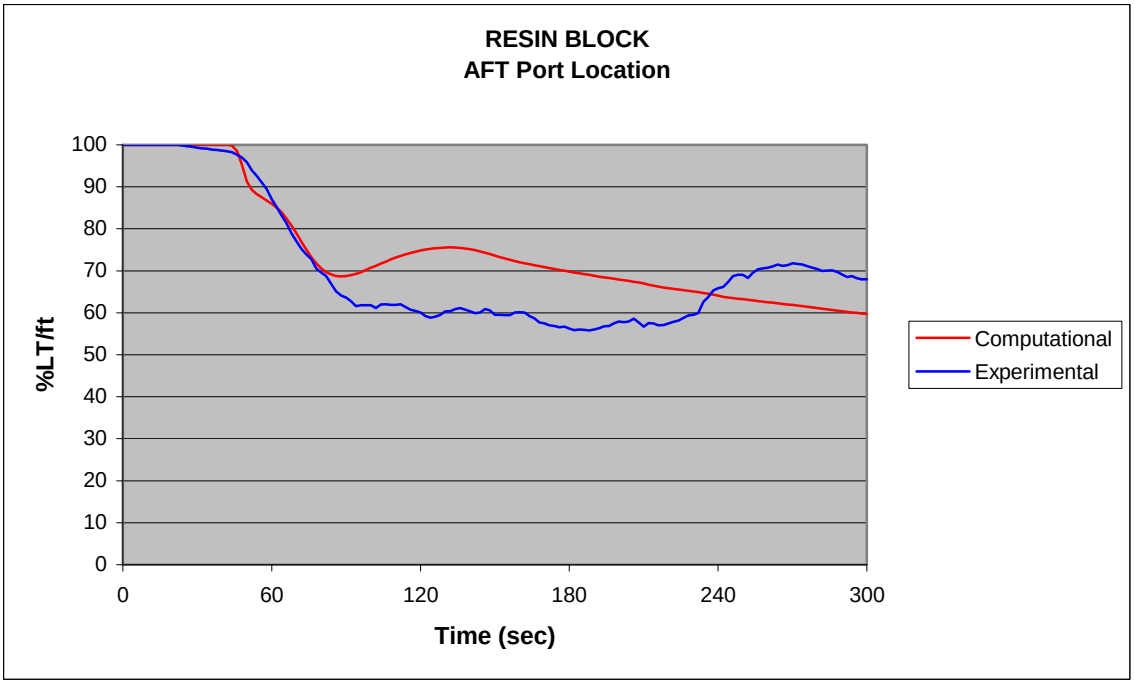

Figure 72. Comparison of Computational and Experimental Resin Block Percent Light Transmission per Foot at Aft Port Location

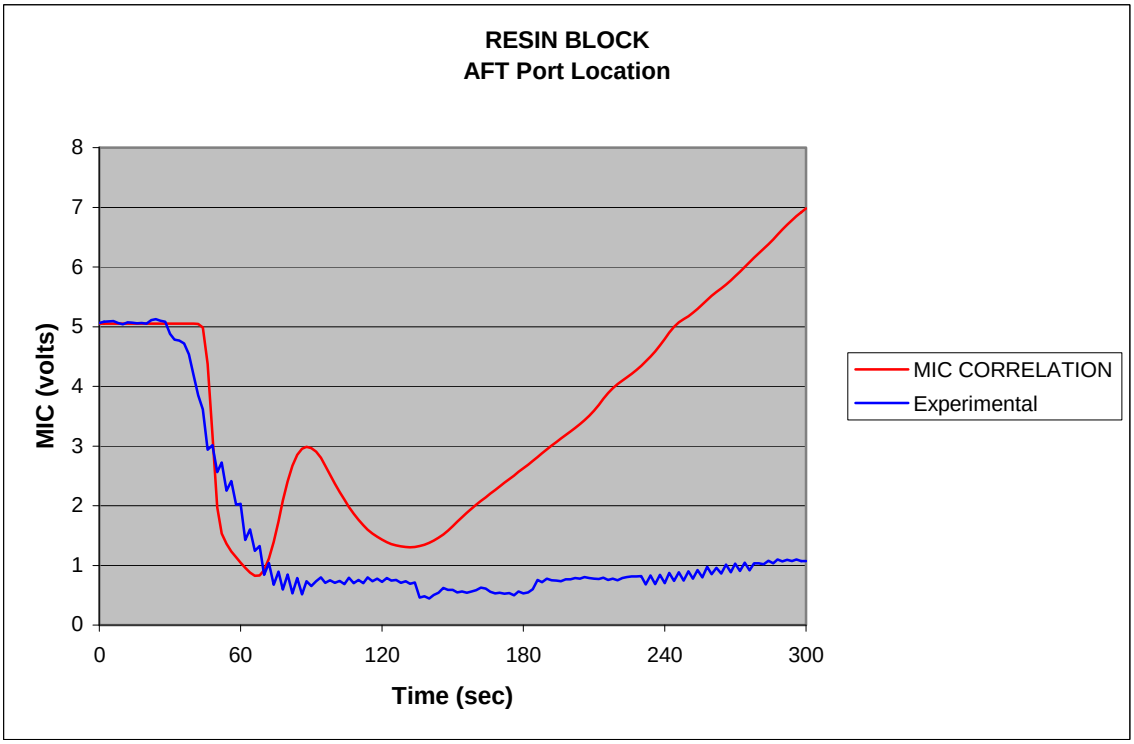

Figure 73. Comparison of Computational and Experimental Resin Block MIC Voltages at the Aft Port Location

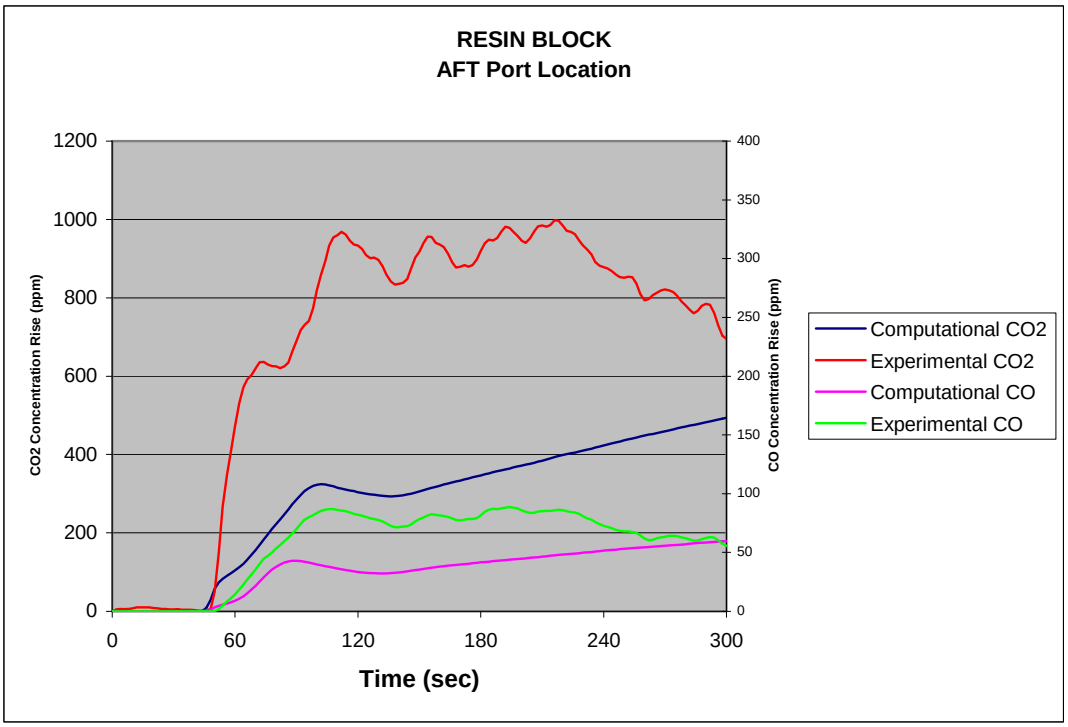

Figure 74. Comparison of Computational and Experimental Resin Block CO and CO_2 Gas Concentrations at Aft Port Location

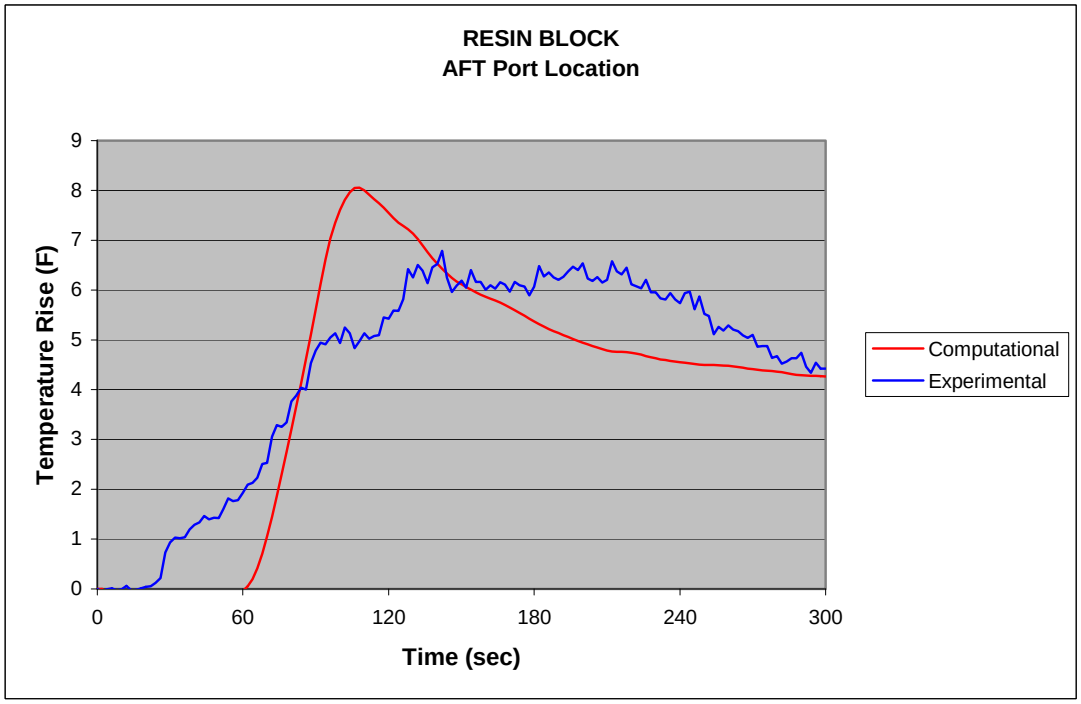

Figure 75. Comparison of Computational and Experimental Resin Block Temperature Rise at the Aft Port Location

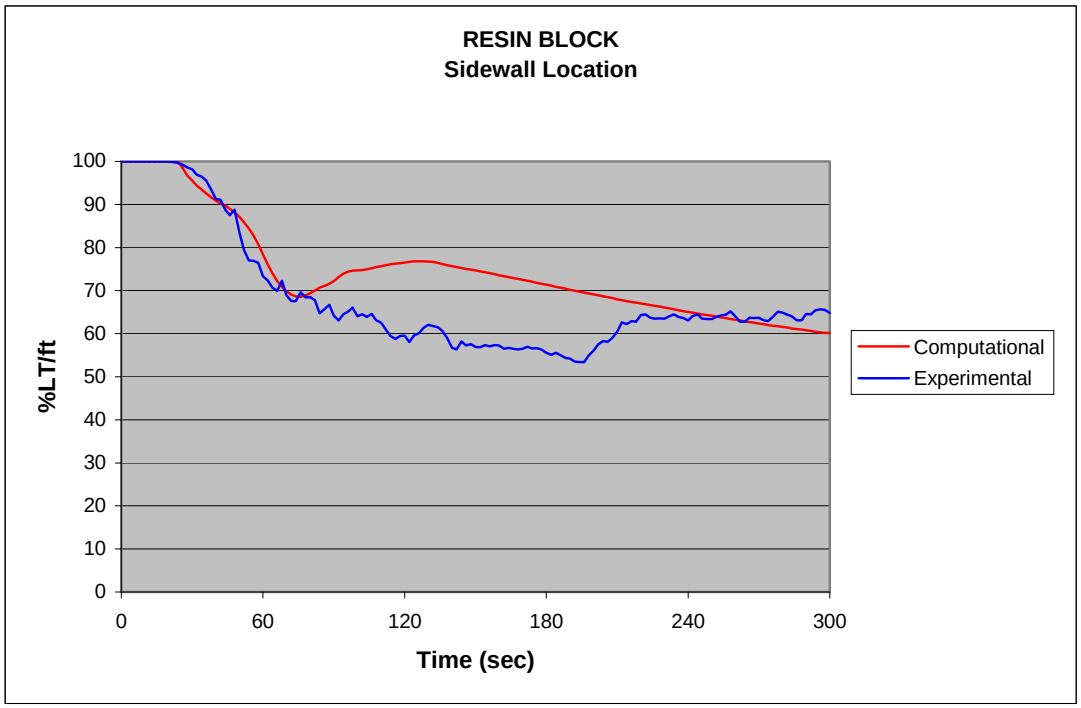

Figure 76. Comparison of Computational and Experimental Resin Block Percent Light Transmission per Foot at the Sidewall Starboard Location

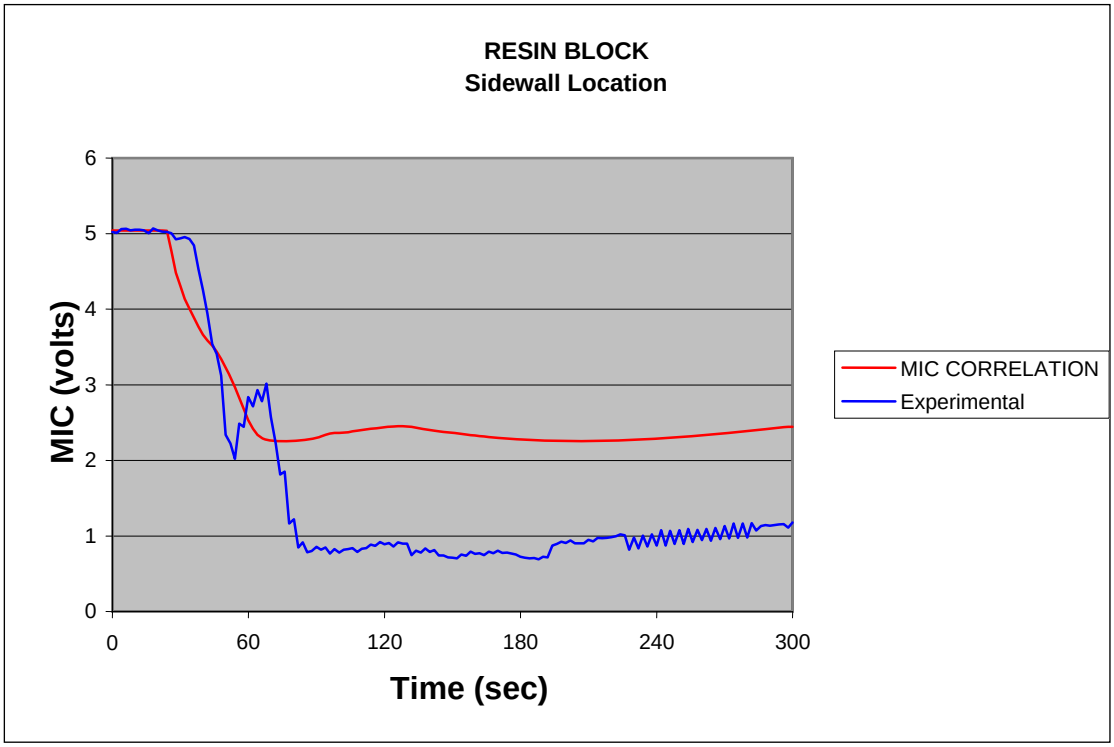

Figure 77. Comparison of Computational and Experimental Resin Block MIC Voltages at the Sidewall Starboard Location

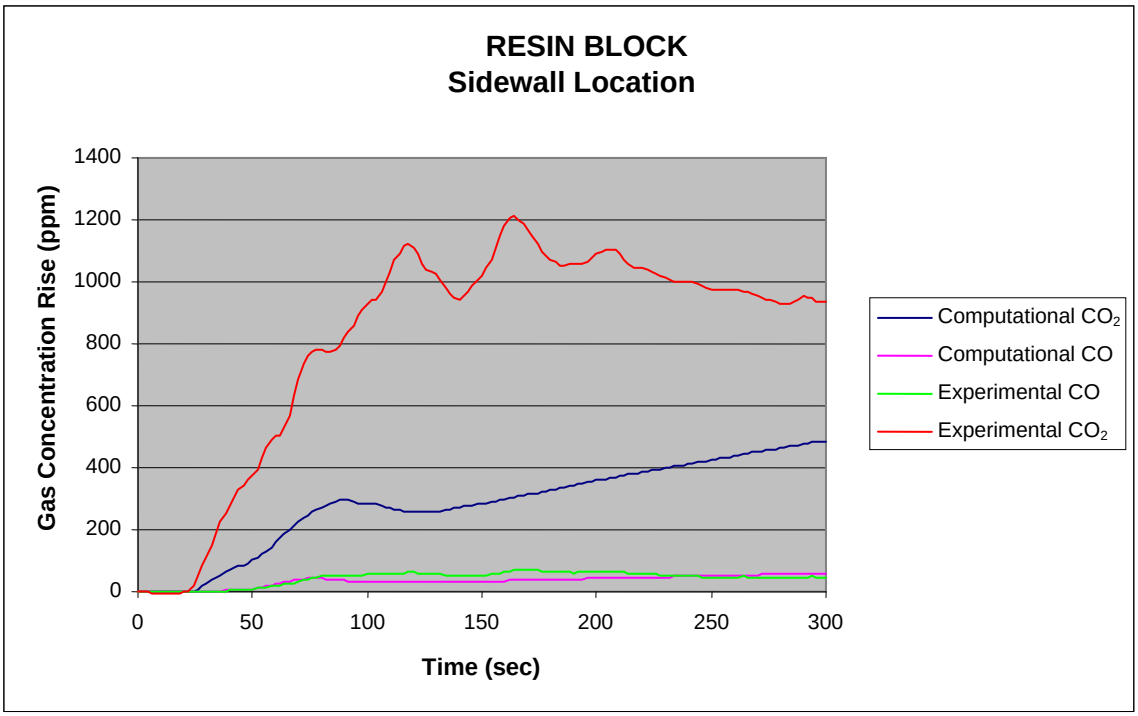

Figure 78. Comparison of Computational and Experimental Resin Block CO and CO_2 Gas Concentrations at Sidewall Starboard Location

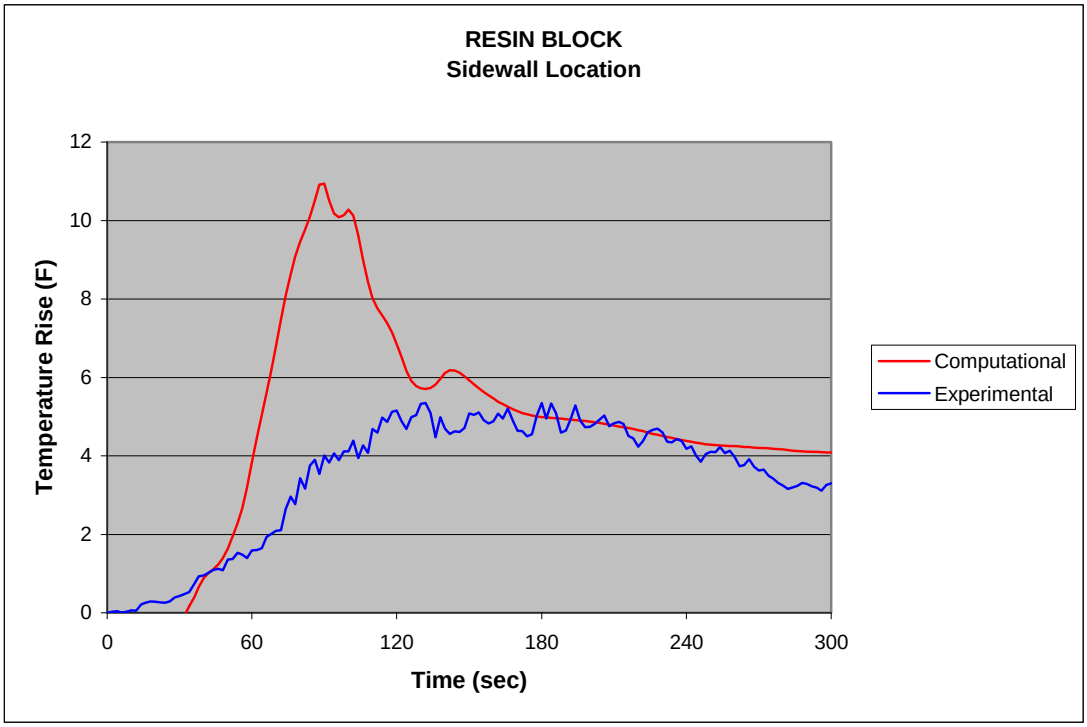

Figure 79. Comparison of Computational and Experimental Resin Block Temperature Rise at Sidewall Starboard Location

5.9 COMPUTATIONAL AND EXPERIMENTAL TIME COMPARISON.

To conduct an alarm time comparison between computational and experimental data for all detectors, it was necessary to import the computational data into the pre-existing threshold matrix. Table 7 shows the extreme detector levels for both new computational modeling data and the already existing experimental resin block data.

Alarm time results from the application of all five multisensor detector algorithms, the photoelectric detector, and the ionization detector for the resin block at different locations are displayed in table 8. Alarm time comparison between computational and experimental data is shown at the bottom of table 8. Analysis of this table showed that the maximum difference in alarm times between computational and experimental was 10 seconds and occurred for only the sidewall location, for algorithms 1 and 4. The majority of the alarm time comparison results revealed a difference of either 2 or 4 seconds. The average alarm time difference between computational and experimental was calculated to be approximately 2.57 seconds. Although temperatures and CO_2 gas concentrations between computational and experimental results were not in agreement, alarm times between the two were not significantly affected. One reason was because CO_2 gas concentrations exceeding 7.5 ppm, the algorithm threshold value, were obtained at about the same time for both computational and experimental results. Results from the alarm time comparison, coupled with the strong agreement obtained from previous smokemeter and MIC data analysis at all locations, showed that the CFD model may be used to accurately predict the alarm time of the multisensor detector using all five alarm algorithms.

Table 7. Extreme Detector Levels

	MIC (Volts)	Rate of Rise (Volts/sec)	Smokemeter (%LT/ft)	Rate of Rise (%LT/ft)	CO (ppm)	Rate of Rise CO	CO_2 (ppm)	Rate of Rise CO_2	Temperature Change (°F)	Temperature Rate of Rise
EXPERIMENTAL										
Resin block (X location)	0.589	-0.522	48.743	-3.036	108.889	4.580	1497.116	49.026	9.831	0.815
PERIMETER TESTING										
Resin block (Fwd)	0.583	-0.246	59.959	-1.522	86.243	3.571	1076.050	34.180	3.831	0.312
Resin block (Aft)	0.447	-0.340	55.755	-0.010	88.763	2.369	997.473	58.431	6.782	0.302
Resin block (Sidewall)	0.691	-0.391	53.372	-2.722	94.696	2.777	1245.117	24.185	5.352	0.332
COMPUTATIONAL										
Resin block (X)	0.820	-1.414	63.207	-4.003	88.042	2.990	688.218	15.176	46.829	1.081
PERIMETER TESTING										
Resin block (Fwd)	0.820	-0.465	73.544	-1.458	56.842	2.126	469.947	17.167	11.319	0.582
Resin block (Aft)	0.827	-0.613	59.726	-2.079	59.663	1.809	493.587	14.408	8.053	0.282
Resin block (Sidewall)	2.254	-0.144	60.187	-1.171	58.794	2.006	485.523	7.847	10.940	0.338

Table 8. Alarm Time Comparison—Computation vs Experimental

Fires Sources	Algorithm					Photoelectric	Ionization
	1	2	3	4	5		
EXPERIMENTAL							
Resin block (X location)	20	18	18	24	14	20	20
PERIMETER TESTING							
Resin block (Fwd)	70	48	48	50	48	54	84
Resin block (Aft)	50	50	50	54	50	50	42
Resin block (Sidewall)	38	26	26	38	26	36	42
COMPUTATIONAL							
Resin block (X location)	20	18	18	20	18	18	18
PERIMETER TESTING							
Resin block (Fwd)	70	52	52	52	50	52	82
Resin block (Aft)	50	50	50	50	46	48	48
Resin block (Sidewall)	28	26	26	28	26	30	34
ALARM TIME COMPARISON (Computational vs Experimental)							
Resin block (X location)	0	0	0	4	4	2	2
Resin block (Fwd)	0	4	4	2	2	2	2
Resin block (Aft)	0	0	0	4	4	2	6
Resin block (Sidewall)	10	0	0	10	0	6	8

5.10 SPATIAL DISTRIBUTION RESULTS.

As a result of the strong agreement between computational and experimental data, the CFD model was used to conduct fire simulations at various distances away from the recessed pan. The best way to determine the physical radius of successful operation for the multisensor detector was to run simulations in the furthest possible locations within the B-707 cargo compartment and check alarm times for all five algorithms. Table 8 shows alarm times for the furthest locations; the forward bulkhead wall and the aft wall. Analysis of table 8 showed that only algorithm 1 was unable to detect the resin block fire source at the furthest location in less than 60 seconds. All other algorithms alarmed in less than 60 seconds. Therefore, it was safe to designate the physical range of this multisensor detector subjected to algorithms 2 through 5 as at least 910 cubic feet, the volume of the B-707 forward cargo compartment.

5.11 ERROR ANALYSIS.

5.11.1 Repeatability.

Repeatability was one of the most important factors that had to be considered when fire testing. There was the need to reproduce similar results for each time a test of the exact same nature was performed. Without repeatability, it was difficult to determine whether or not the data acquired was accurate. All real fire sources were tested at least four times and analyzed for repeatability to within 5% variation from the average when comparing data from each of the four sensors. Comparison of trends between similar tests was also performed to eliminate the erroneous or failed experiments from the successful experimental tests. There were some special cases, such as the suitcase fire test, where repeatability was an issue. Since suitcases consist of various types of fabrics, which all combust and smolder differently, it was difficult to attain repeatability between tests. Results from the suitcase tests were presented with reasonable accuracy. All possibilities of both human and instrumental errors associated with each sensor used in the experiments for this project are outlined in the sections below.

5.11.2 Thermocouple.

Soot accumulation on the thermocouple beads could impact the temperature measurements. Although the pan thermocouple was calibrated prior to installation, soot on the bead itself after numerous fire tests could skew temperature measurements. For the Omega Type-K Thermocouple used in the experiments, the manufacturer error range was approximately ±4 degrees Fahrenheit or an uncertainty as high as 0.75% of the output temperature. However, by using changes from ambient temperature data, it reduced the error associated with thermocouple to thermocouple temperature variability.

Computational and experimental temperatures were significantly different and can be explained because of the following reasons. The computational temperatures were gas temperatures, not thermocouple temperatures [25]. The correction of the gas temperatures to thermocouple temperatures required knowledge of the gas velocities and significant densities. Another potential reason for the difference in temperature was the omission of radiation from the fire source in the calculations. Literature reveals that radiation from fires can approach 30% of the heat release [25]. Also another plausible reason for the discrepancy was the manner in which

temperatures were determined in the model; through the user-entered constant species heat capacities [25].

5.11.3 Smokemeter.

The extensive smokemeter setup gave rise to errors from either the photodetector, the fixed laser, or soot accumulation on the mirrors. Soot accumulation on the mirrors inside the recessed pan, and on the slide glasses used to enclose the recessed pan from the holes where the laser and photodetector operate, led to random fluctuations in percent light transmission data. To compensate for such an occurrence, prior to every test, all mirrors and slide glasses inside the recessed pan were cleaned. Also, smokemeter voltage output from the data acquisition system was measured to produce stability within ±1% about the mean voltage. This would ensure that the smokemeter was not fluctuating randomly from soot accumulation on mirrors or background particles from previous testing. Along with this procedure, optical density filter tests were conducted occasionally to analyze the power output of the fixed laser source. The photodetector output fluctuates randomly ±0.1% about the mean intensity, which was within the accuracy range of the voltage output stability.

5.11.4 Gas Probe.

The accuracy of the Rosemount analytical CO and CO_2 analyzers were obtained from the manufacturer as ±1% of the range. Therefore, for the CO with a range of 500 ppm, there was a maximum variation of ±5 ppm. For the CO_2, with a range of 2500 ppm, there was a maximum variation of ±25 ppm. Apart from the instrumental error, the lag in the gas analyzer readings due to transport times through the line and instrument response could result in skewed data. Although the 8 seconds were subtracted from the experimental data to adjust for the lag in response due to line transport, instrument response was not accounted for.

Another potential source of error between computational and experimental data was differences in the burning behavior of the flaming resin block in the cargo compartment, as compared to cone calorimeter testing done to produce heat release rate terms [25]. Any difference in the local ventilation or the thermal environment between the cone calorimeter and the cargo compartment could introduce error into the calculation boundary conditions and results. The ratio of CO to CO_2 for the burning resin block in the cone calorimeter and cargo compartment were compared to determine if over ventilation was occurring in the cone calorimeter. Although there was some variability in the ratios over the course of the respective tests, the ratios were not consistently higher or lower in either test location, leading to the assumption that the burning behavior in both locations was similar.

5.11.5 Measuring Ionization Chamber.

The measuring ionization chamber could easily be affected by residual dust or particles from previous tests. Therefore, prior to each test, the data acquisition system was checked to output a continuous reference voltage of 5.1 volts with a maximum uncertainty fluctuation of ±1% of reference voltage. The Arizona test dust nuisance source test oversaturated the ionization chamber and altered the reference voltage to about 4.8 volts. Compressed air was used to clean

out the inside of the chamber before commencing with more experiments. These reasons explain why the reference voltage had to be attained prior to commencing tests.

5.11.6 Ground and In-Flight Comparison.

All experimental data generated during this project were ground tests conducted in ambient conditions. In-flight environmental conditions, such as varying pressure and temperature effects, were considered to completely evaluate the performance and functionality of the multisensor detector. Of the four sensors used in the multisensor detector, literature revealed that the ionization detector exhibited the greatest tendency for variability in environments of varying temperature and pressure. Almost all cargo compartments are located within the pressurized region of the aircraft where the pressure varies from levels between 10.92 psi to ambient ground pressure of 14.7 psi. This small pressure variation during in-flight conditions is insignificant and will not result in malfunction of the ionization detector as long as the change is not abrupt.

The effect of temperature variations at different altitudes on all four sensors was also considered. Since cargo compartments are used for transporting various types of cargo ranging from livestock to vegetation, these types of cargo require compartment temperatures to remain significantly above the critical operational temperatures of all four sensors. The range of the Kidde ionization smoke detector used in this report is between 40 and 100 degrees Fahrenheit. This discussion shows that for normal in-flight scenarios with gradual variations in pressure and temperature, the multisensor detector should exhibit similar performance criteria to that achieved during the ground testing.

6. CONCLUSIONS.

The following summarizes the results of this project.

- Multisensor Detector versus Current Aircraft Smoke Detectors.
  - The multisensor detector complied with Title 14 Code of Federal Regulations Part 25.858, which requires that the detection system alarms within 1 minute of the start of a fire.
  - The multisensor detector demonstrated faster response times compared to the photoelectric detector, which is the primary aircraft fire detection method.
  - The multisensor detector demonstrated faster response times compared to the ionization detector, which is the secondary aircraft fire detection method.
  - The multisensor detector provided 100% nuisance immunity to those signatures tested.
  - The multisensor detector demonstrated a 100% success rate, when subjected to 30 different experimental tests, with five fire sources and five nuisance sources.
  - The photoelectric detector yielded a 66.67% success rate.

- The ionization detector yielded a 73.33% success rate.
- The photoelectric detector failed four of the five nuisance sources tested.
- The ionization detector failed two of the five nuisance sources tested.

- Algorithm Development and Performance.
  - Inclusion of the rate of rise parameter provided the first 100% successful multisensor detector algorithm, with no response to nuisance sources, and detection within the 1-minute federal regulation.
  - Algorithm 5, consisting of the carbon dioxide (CO_2) gas probe in combination with temperature rise, measuring ionization chamber (MIC), and smokemeter output, demonstrated a 100% success rate with the fastest alarm times, while distinguishing between real fire and nuisance sources.
  - Inclusion of the rate of rise parameter in algorithm criteria for all sensors in the multisensor detector produced faster response times for all algorithms.
  - Comparison between carbon monoxide (CO) and CO_2 gas species for algorithm performance criteria revealed CO_2 as being more effective.

- Computational Fluid Dynamic (CFD) Model
  - Comparison of computational data to experimental data revealed a strong agreement with regards to percent light transmission per foot.
  - A polynomial correlation based on computational light transmission per foot can be used to provide accurate computational MIC voltage.
  - Comparison of computational and experimental alarm time, smokemeter, and MIC results demonstrated the effectiveness of the CFD and provided strong evidence that the CFD can be used as a virtual detector to simulate fires in a Boeing 707 forward cargo compartment or compartments of similar or lesser volume with an average alarm time uncertainty of 2.57 seconds.

7. REFERENCES.

1. Freiling, A., “New Approaches to Aircraft Fire Protection,” European Aeronautic Space and Defense Company, Germany, *AUBE 2001 Conference*, pp. 641-652.

2. Schmoetzer, K., “Aircraft Fire Detection: Requirements, Qualification and Certification Aspects,” European Aeronautic Space and Defense Company, Germany, *AUBE 2001 Conference*, pp. 630-640.

3. Qualey III, J.R., Desmarais, L, and Pratt, J., “Response Time Comparisons of Ionization and Photoelectric/Heat Detectors,” Simplex Time Recorder Co., *AUBE 2001 Conference*, pp. 283-299.

4. Blake, D., “Aircraft Cargo Compartment Smoke Detector Alarm Incidents on U.S.-Registered Aircraft, 1974-1999,” FAA report DOT/FAA/AR-TN00/29, June 2000.

5. Zakrzewski, R., Sadok, M., and Zeliff, B., “Video-Based Cargo Fire Verification System for Commercial Aircraft,” Goodrich Corporation, USA, *AUBE 2004 Conference*, pp. 291-300.

6. Hedrick, R.L. and Billick, I., “Chamber Tests of Residential CO Alarms,” Gas Research Institute, 1997.

7. Mangon, P., “Fire Detection for Aircraft Cargo Compartments, Reduction of False Alarms,” *AUBE 2001 Conference*, pp. 653-664.

8. Blake, D. and Suo-Anttila, J., “Aircraft Cargo Compartment Fire Detection and Smoke Transport Model,” FAA William J. Hughes Technical Center, USA, Sandia National Laboratories, USA, *AUBE 2004 Conference*, pp. 376-385.

9. Code of Federal Regulations 14 CFR Part 25.858, “Cargo or Baggage Compartment Smoke or Fire Detection Systems,” 2006.

10. Society of Automotive Engineers, “Cargo Compartment Fire Detection Instrument,” Aerospace Standard 8036, Inc., 1985.

11. Cleary, T. and Grosshandler, W., “Survey of Fire Detection Technologies and System Evaluation/Certification Methodologies and Their Suitability for Aircraft Cargo Compartments,” National Institute of Standards and Technology, NISTIR 6356, USA, 1999.

12. Code of Federal Regulations 14 CFR Part 25.857, “Cargo Compartment Classification,” 2006.

13. Cleary, T. and Donnelly, M., “Aircraft Cargo Compartment Fire and Nuisance Source Tests in the FE/DE,” National Institute of Standards and Technology, USA, *AUBE 2001 Conference*, pp. 689-700.

14. Boucourt, G., “Two Dimensional Multi Detection Fire Sensor, System Architecture and Performances,” *AUBE 2001 Conference*, pp. 677-688.

15. Hunter, G., “Where There’s Smoke, There’s Not Always Fire. A New Approach to Fire Detection,” National Aeronautics and Space Administration, John H. Glenn Research Center.

16. Gottuk, D., Peatross, M., Roby, R., and Beyler, C., "Advanced Fire Detection Using Multi-Signature Alarm Algorithms," Hughes Associates, Inc., USA, *AUBE 1999 Conference*, pp. 237-246.

17. Cestari, L., Worrell, C., and Milke, J., "Advanced Fire Detection Algorithms Using Data from the Home Smoke Detector Project," *Department of Fire Protection Engineering, Fire Safety Journal*, 40, 2005, pp. 1-28.

18. Krull, W., Willms, I., and Shirer, J., "Test Methods for a Video-Based Cargo Fire Verification System," Goodrich Corporation, USA, *AUBE 2004 Conference*, pp. 301-313.

19. Storm, U., Bartels, O., and Binder, J., "A Resistive Gas Sensor With Elimination and Utilization of Parasitic Electric Fields," Sensors and Actuators B77, 2001, pp. 529-533.

20. Storm, U., Freiling, A., Schmoetzer, K., and Kohl, D., "Fire Gas Detectors for Aircraft Application," AIRBUS, Germany, *AUBE 2004 Conference*, pp. 324-334.

21. Goldmeer, J., "A Rugged LED-Based Sensor for Fire Detection," Southwest Sciences, Inc., USA, *AUBE 2001 Conference*, pp. 378-389.

22. *Proceedings Fire Suppression and Detection Research Applications*, "Using Multiple Sensors for Discriminating Fire Detection," 1999, pp. 150-164.

23. Environmental Protection Agency, "Ionization Technology," Smoke Detectors and Radiation, URL: http://www.epa.gov/radiation/sources/smoke_ion.htm

24. Environmental Protection Agency, "Photoelectric Technology," Smoke Detectors and Radiation, URL: http://www.epa.gov/radiation/sources/smoke_photo.htm.

25. Suo-Anttila, J., Gill, W., Gallegos, C., and Nelsen, J., "Computational Fluid Dynamics Code for Smoke Transport During an Aircraft Cargo Compartment Fire. Baseline Validation," Sandia National Laboratories, USA, October 2003.

26. Blake, D., Suo-Anttila, J., Domino, S., Gill, W., and Gritzo, L., "Initial Development of Improved Aircraft Cargo Compartment Fire Detection Certification Criteria," FAA William J. Hughes Technical Center and Sandia National Laboratories, USA, *AUBE 2004 Conference*, pp. 615-629.

27. *The FAA Smoke Transport Code Users Manual*, FAA William J. Hughes Technical Center, USA, 2004. URL: http://www.esc.sandia.gov/faa-stc/index.html